Master thesis : Multi-band IR sensor for Earth Observation

Auteur : Vilaboa Perez, Jesus
Promoteur(s) : Habraken, Serge
Faculté : Faculté des Sciences appliquées
Diplôme : Master en ingénieur civil en aérospatiale, à finalité spécialisée en "aerospace engineering"
Année académique : 2018-2019
URI/URL : http://hdl.handle.net/2268.2/6781

University of Liège - Faculty of Applied Sciences

Multi-band Infrared Sensor For Earth Observation

Author:

Jesús Vilaboa Pérez

Academic advisor:

Prof. Serge Habraken

Assistant:

Victor Laborde

Graduation Studies conducted for obtaining the Master's degree in Aerospace Engineering

Academic year 2018-2019

Abstract

A new CubeSat is in development by students and professors of the University of Liège and the Centre Spatial de Liège. The CubeSat OUFTI-NEXT will measure the hydric stress in crop fields in order to enhance the management efficiency of the water resources for agriculture. This CubeSat incorporates a thermal imager to capture the electromagnetic radiation of the infrared band. In this project, it is analysed the performance of the different infrared detectors that can be used within the CubeSat optical instrument.

There are a few examples of CubeSat missions observing in the Mid-Wave Infrared Band or in the Long-Wave Infrared band. However, any of these missions can observe in both bands at the same time. This Master Thesis describes the feasibility of an optical instrument for a CubeSat observing in both bands with the use of a single detector. With this aim, the performance of the two main groups of infrared detectors, photodetectors and thermal detectors, is measured in terms of temperature resolution and signal-to-noise ratio in the space environment. These computations are carried on with the model of equations developed in this Master Thesis.

Keywords: CubeSat, Dual-band, Microbolometer, Photodetector, NETD, SNR.

Jesús Vilaboa Pérez

June 2019

Acknowledgements

I would like to express my gratitude to Prof. Serge Habraken for the astounding opportunity to possibly realise my Master Thesis in the Centre Spatial de Liége. I really appreciate all the help and advice received from him during the whole project. I can state that I have found a field in space engineering that extremely enthusiasm me and in which I would like to continue in the near future. I am also very grateful for all the advice received from Victor Laborde that always helped me to continue when the complexity of the project was very high.

My special thanks to Prof. Jerôme Loicq for its support and help to coordinate the work of Antonio and mine to advance further in this project. Thanks also to Prof. Gaëtan Kerschen since he presented my the OUFTI project and the opportunity to do a Master Thesis in the topic.

Thanks to the other students involved in the project, Antonio, Arnau, Alex and Ysaline. And finally, I am very grateful to my family and friends who always support me.

Contents

List of Figures

List of Tables

Acronyms

AFPA Adaptative Focal Plane Array.

BLIP Background Limited Infrared Photodetector.

CCD Charge-Coupled Device.

CFA Colour Filter Array.

CIRAS CubeSat Infrared Atmospheric Sounder.

CMOS Complementary Oxide-Semiconductor.

CUMULOS CubeSat Multispectral Observation System.

DISR Descent Imager Spectral Radiometer.

FOV Field Of View.

FPA Focal Plane Array.

FPF Fabry Perot Filter.

GSD Ground Sampling Distance.

HTSC High Temperature Superconducting Bolometers.

IDCA Integrated Dewar Cooled Assembly.

IMS Image Mapping Spectrometer.

ITR Integrate Then Reading.

IWR Integrate While Reading.

JWST James Web Space Telescope.

LWIR Long-Wave Infrared Range.

MEMS Microelectromechanical System.

MGS MWIR Grating Spectrometer.

MISTIGRI Micro Satellite for Thermal Infrared Ground Surface Imaging.

MMO Mars Micro Orbiter.

MPT Micro Pulse Tube.

MRTD Minimum Resolvable Temperature Difference.

MSFA Multispectral Filter Array.

MTF Modulation Transfer Function.

MTGI Meteosat Third Generation Imaging Satelite.

MWIR Mid-Wave Infrared Range.

NEP Noise Equivalent Power.

NETD Noise Equivalent Temperature Difference.

OUFTI Orbital Utility For Thermal Imaging.

QDIP Quantum Dot Infrared Photodetector.

QWIP Quantum Well Infrared Photodetector.

ROIC Read-Out Integrated Circuits.

SLS Strained Layer Superlattice.

SNR Signal-To-Noise Ratio.

SWIR Short-Wave Infrared Range.

T2SL Type II Superlattice.

TDI Time Delay Integration.

TEC Thermoelectrical Cooler.

THEMIS Thermal Emission Imaging System.

TLHJ Triple Layer Heterojunction.

VNIR Very-Near Infrared Range.

Chapter 1

Introduction to the project

1.1 The OUFTI CubeSat mission

In April 2016 there was successfully launched the CubeSat OUFTI (Orbital Utility For Telecommunication Innovations). It was destined to test an innovative telecommunication protocol, known as D-STAR. This CubeSat was developed with the work of students and professors of the University of Liège and the Centre Spatial de Liège.

The OUFTI CubeSat was an excellent tool to learn about satellite technologies and space missions. As a result, a new OUFTI CubeSat is now in development.

The CubeSat OUFTI-NEXT (Orbital Utility For Thermal Imaging NEXT), will measure the hydric stress in crop fields in order to enhance the management efficiency of the water resources for agriculture. It will incorporate a thermal imaging instrument to capture the infrared electromagnetic radiation emitted by the plants. Inside of the thermal instrument, it is located the detector. The study of this device is covered in this Master Thesis document.

At the beginning, this CubeSat mission was oriented to capture the electromagnetic radiation in the Mid-Wave Infrared Range (MWIR). However, as it will be now presented, it is also very interesting to look at the Long-wave Infrared Range (LWIR). Nowadays, it is possible to find a few examples of CubeSat operating in one of the two bands of the infrared range. Nevertheless, it has not been developed any CubeSat with an optical instrument sensitive to both bands.

One of the main objectives of this project will be to study the feasibility of a CubeSat mission capturing light from two bands of the infrared electromagnetic spectrum, using only one thermal imager instrument.

Next, there are included the difference between the MWIR and the LWIR bands, and why it is interesting to observe in both bands.

1.2 Differences between the Mid-Wave Infrared and the Long-Wave Infrared bands

In general, the MWIR defines the band from 3 μm to 5 μm, while the term LWIR is used for the 8 μm to 14 μm band. The wavelength at which the Earth surface emits a maximum of radiation is around 10 m. Therefore, the LWIR band is commonly used for temperature remote sensing. In the LWIR band, the sensitivity is higher observing at ambient temperature objects [40].

A very important parameter of an infrared imaging instrument is the contrast. A thermal image is formed by capturing the different emissivities of a target due to the differences in the temperature. The contrast defines the variation of the power received from the target in function of the changes in temperature. In the MWIR band, the contrast is higher comparing with the LWIR band [41]. Therefore, the MWIR band is useful to observe very hot targets, as it could be a fire, or when the sensitivity is not as important as the contrast.

The efficiency of the observations in the MWIR band and the LWIR band is also very dependent on the weather and atmospheric conditions. For example, the LWIR band has a better transmission in fog, mist and dust conditions or winter haze. On the other hand, when the humidity of the scene is high, the transmission of the MWIR band is better [40].

Another fundamental distinction between the MWIR and the LWIR band is that the emissions of the constituents of the atmosphere and the ground is different for both bands.

As a result, the selection of the bands depends on the scene characteristics, the atmospheric transmission, the weather, and the requisites in term of temperature sensitivity and temperature contrast.

Therefore, it is clear that the possibility of capturing light from the two both bands with the same optical instrument will be an enormous advantage.

1.3 Objectives of the project

The main goal of this project is to study in detail the different infrared detectors that can be implemented in the optical instrument of the OUFTI-CubeSat. This research will be divided into the following sections:

- **Single-band infrared detectors:** the purpose is to make a full review of all the single-band, MWIR and LWIR, infrared detectors. The study has to be oriented into detectors that can be used in the space environment. Once studied the different sensors, the objective will be to analyse and select the best single-band detectors, available at the moment in the market, for a near CubeSat mission.

- **Multi-band infrared detectors:** this is the point of higher interest in this project. As discussed before, there are no previous examples of CubeSat missions capturing light from two bands in the infrared. The goal is to analyse if it will be possible to carry on a mission with these characteristics with the technology available at the moment in the market. This technology has to be designed, in terms of size and wavelength operation range, to be used in a space CubeSat mission.

- **How to split the light into its different wavelengths:** there is also the possibility of using a single-band detector together with band-pass filters and other optical devices for multispectral operation. The term multispectral refers to multiple bands, more than two, in the MWIR band or in the LWIR regions. Another objective is to analyse if it is possible to do multispectral imaging in the dual-band detectors technology.

- **Performance of the detectors in the space environment:** another fundamental goal of this project is to create a model that can be used to test the performance, in terms of temperature resolution and signal-to-noise ratio of the detectors operating in the space environment. This model has to be useful to determine the feasibility of the mission.

For this project, there will be used several different research tools besides the software MATLAB to develop the model to test the performance of the optical detectors in space.

Chapter 2

Infrared optical instruments

2.1 Introduction

The starting point of the project will be a review of all the infrared detectors developed for single-band operation. That is detectors for the Short-Wave Infrared range, SWIR, Mid-Wave Infrared Range, MWIR, and Long-Wave infrared range. In the next chapter, there will be presented the detectors operating in dual-band, for example, the MWIR-LWIR infrared detectors.

All the infrared technology covered in this chapter will be oriented to space applications. It will be seen how not all the available technologies can withstand the space environment. In addition to this, there will be presented several examples of small infrared detectors, very suitable for a CubeSat mission, available at the market. The final objective will is to select a detector that accomplishes the requisites of the OUFTI mission

2.2 Infrared optics

A thermal imager is made of a set of lenses or mirrors that project the incoming thermal radiation from a target into a heat sensitive sensor. The material used for these optical surfaces depends on the wavelength range of the infrared spectrum that is observed. For example, it is commonly used for the Mid Wave Infrared Range, MWIR, Si or Ge materials. The Ge can be also used for optical instrument operating in the Long-Wave Infrared Range, LWIR. Other examples of materials for the MWIR-LWIR full range, are ZnS, ZnSe and CdTe or the Chalcogenide IRG22, [42].

Two of the main parameters used to describe an optical instrument are the focal length, f, and the diameter of the entrance pupil, D_p. The focal length is the distance

from the lens to the point in which the incoming rays of light are focused. The ratio of these two quantities is known as the F-number, F/#, defined in Equation 2.1.

$$F/\# = \frac{f}{D_p} \tag{2.1}$$

The importance of the F-number is that it characterizes the resolution limit of an optical system. Infinite resolution is not possible because of the wave properties of light. This property is defined by the diffraction limit, D_l, of the optical system. The D_l parameter is proportional to the F-number and the wavelength of the electromagnetic spectrum observed, according to Equation 2.2. It defines the minimum size of the pixel that can be used in the detector array [43].

$$D_l = 2.44 \cdot \frac{f \cdot \lambda}{D_p} = 2.44 \cdot F/\# \cdot \lambda \tag{2.2}$$

The size of the pixel is defined with the pixel pitch. In general, pixels for infrared detectors are squared with dimensions in the order of micrometres. However, not all the pixel area is sensitive to infrared radiation. This is defined by the fill factor, which is the percentage of the pixel area that actively participates in the conversion of the incoming flux of photons into electrons to be later measured. Moreover, the number of pixels in the array will define the resolution of the final image. But not always a higher number of pixels is better, since, in general, a higher number of pixels is achieved by reducing their size in the array. This reduction will cause a decrease in the signal-to-noise ratio, SNR, of the optical sensor which depends directly on the size of the pixel. This statement will be covered in detail along with the project.

In addition to this, the pixel size is also used in the definition of the angular resolution of the optical system. This parameter is presented in Equation 2.3, depending on the focal length, the altitude of the satellite, h, and the ground sampling distance, GSD. The GSD defines the spatial resolution of the optical system. It is the area in the ground corresponding to each individual pixel of the detector array. Therefore, it is the minimum detail for the final thermal image [1]. The angular resolution is illustrated in Figure 2.1.

$$\frac{GSD}{h} = \frac{ps}{f} = \tan(\alpha) \tag{2.3}$$

For example, if the altitude of the satellite increases, for the same spatial resolution, GSD, it will be necessary to reduce the pixel size or to increase the focal length. After

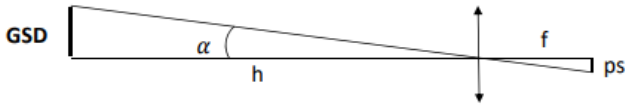

Figure 2.1: Definition of angular resolution. [1]

this introduction to the optical subsystem, it will be started the detail presentation of detectors for the infrared.

2.3 Infrared detectors

A detector or sensor is a device that responds to some type of input coming from an event or change in the physical environment. These specific inputs could be light, speed, temperature, pressure, humidity, besides another large number of possible phenomena that can be found in nature. Therefore, a sensor will detect these electrical or optical signals and convert them in another type of signal that can be read and quantified.

The kind of sensor used within the optical subsystem of satellites is a sensor for imaging. These modules capture the radiation from a specific range of the electromagnetic spectrum that a target emits. The purpose is to have a representation of the scene that the optical subsystem is observing.

In the case of the infrared optics, a thermal image will be formed with the thermal heat radiation from the infrared spectrum that reaches the detector array. The thermal image obtained with these heat-sensitive detectors will be a pictorial representation of temperature differences observed in the target.

Since the sensor is located in the focal plane of the optical system, we can refer to the detector array as the Focal Plane Array (FPA). Additionally, is possible to talk about a second component of the detector. It is the circuit module, which is in charge of the conversion of the signal detected by the FPA into a signal that can be electrically measured and read. Therefore is possible to differentiate two concepts, detection and readout. The first infrared detectors used a different chip for each action, while the most modern devices implement both technologies in the same chip. These are the read-out integrated circuits (ROIC) characteristic of the CCD and CMOS technology that will be explained along the following chapters [6].

According to the previous background, is possible to classify infrared detectors in function of the way in which the thermal image is formed, the material of the sensitive element, the circuit used for the processing of the signal, among other parameters as the infrared operating wavelength for the detector.

2.3.1 Two main types of detectors

As an introduction to the historical background, infrared detectors can be split into two broad categories. These are the photodetectors and thermal detectors. The photodetectors are also known as photon detectors or quantum detectors [44].

The main difference in the operational principle of photodetectors and thermal detectors is located in the FPA sensitive part. The differences in the electronic module are lower as it will be seen later in this project. In the case of photodetectors, the sensitive part converts an incoming signal of photons into a current of electrons, to be later processed in the electronic module. On the other hand, the FPA of thermal detectors reacts changing its temperature when it enters in contact with a flux of infrared radiation. Then, these changes in temperature will be measured in a different way depending on the type of thermal detector. For example, in bolometer detectors, a type of thermal detectors, what it is measured is the change in the electrical resistance of the FPA after the detection of the photon signal. [44] [41]

Another big difference, not entering into the figures of merit that will be explained in the next section, is the operating temperature of both types of detectors. In general, the performance of a photodetector for the same range of infrared wavelengths, is larger than a thermal detector. Nevertheless, photodetectors have the big constraint that they need to operate at very low temperatures. For reaching these temperatures, 77 K as a standard, they need to be cooled what make them heavier and therefore more expensive than thermal detectors. In contrast, thermal detectors operate usually at room temperatures, around 300 K [41].

One of the main objectives of this project will be to understand in deeply detail both types of detectors with the aim of establishing their implementation in a CubeSat working in the infrared.

2.3.2 Historical background of infrared detectors

Looking back to the last centuries is possible to find several examples of optical systems that made use of photographic plates or films in order to create an image. These optical

systems are telescopes, microscopes, cameras, or even corrective lenses for the human eye which forms an image in the retina.

The first type of detector conceived was the photodetector when at the end of the XIX century Smith discovered the photoconductivity property in Selenium. Following this event, at the beginning of the next century, Einstein illustrated the photoelectric effect on metals. Also, new advances in the Einstein's topic where presented by Planck complementing his model of the radiation emitted by a black body. It was in 1917 when the first infrared photoconductor, a type of photodetector, was presented by T. W. Case. New advances appeared later with detectors for observing further in the infrared. Highlighting in 1933 when the University of Berlin found that lead sulphide had a response to about 3 μm in the electromagnetic spectrum. From this moment, many materials for the IR FPAs started to gradually appear as a result of the advances in new fabrication processes for material purification and uniformity control [44] [2] [41].

During the 1950s, the first extrinsic photoconductive detectors were reported. They had the capability to operate in the long-wave infrared starting in 8 μm until 30 μm wavelengths. These detectors were based on Ge:Hg. By this time, a big effort was also put into the development of Silicon detectors, but it was not until the 1970s, with the invention of the CCD read-out integration circuits, when they gained a real importance [2].

At the same time, great advances were done in the so-called narrow bandgap semiconductors. A semiconductor is a compound that can conduct electricity under some specific conditions. The bandgap is an energy range in a solid, where no electrons states can occur. It is between the valence band and the conduction band. Electrons that goes from the valence band to the conduction band carrying the electric current are known as charge carriers, a definition that will be later used in this project. The properties of these narrow bandgap semiconductors, like a high optical absorbance of the infrared radiation, were very adequate for the IR radiation. The first material with these characteristics was InSb, operating in the mid-wave infrared (MWIR) [41] [2].

It was in the 1960s when the most famous material for infrared FPAs appear. The ternary alloy HgCdTe (MCT). Figure 2.2 shows a timeline of the major advances in techniques and materials in infrared detectors. It shows how the HgCdTe material has

had major importance since the so-called first generation of infrared imagers. HgCdTe can detect in the MWIR and LWIR range.

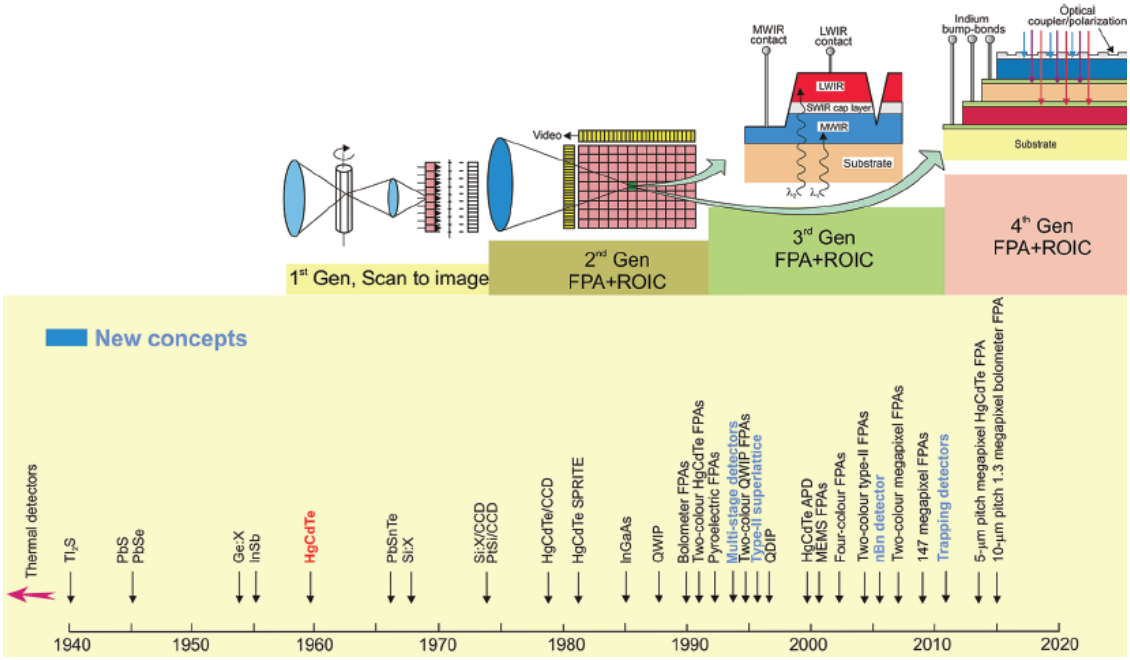

Figure 2.2: Roadmap of the major milestones in development of detectors for the infrared. [2]

Between 1960 and 1975, large advances were achieved in HgCdTe linear photoconductors. That is considered as the first generation of scanning-to-image detectors where the linear detector scans the complete horizontal field of view (FOV).

The second generation of detectors appears in 1975 with the first HgCdTe photodiodes besides the development of CCD chips as cited before. A photodiode, which is another type of photodetector as the photoconductor, presents several advantages over the photoconductor. These differences will be later presented. For the moment, introduce that photodiodes have lower noise, faster response times, lower size besides lower power consumption in comparison with photoconductors. To not get into confusion, the photodiode detectors are inside of a group label as photovoltaic detectors [44].

The first commercial thermal bolometer detectors were presented at the end of the 1990s, point of start of the third generation of infrared detectors. Developments with bolometers started much before, but they were kept in secret due to their use for military applications. In this third generation of detectors is possible to find new enhanced HgCdTe detectors with a greater number of pixels and higher capabilities; the

development of the so-called type-II superlattice detectors which turned nowadays into a real competitor for the HgCdTe; and the appearance of the MEMS microbolometers [44] [2].

The last advances in infrared technology are found in the development of multi-colour sensors sensitive to multiple bands of the electromagnetic spectrum. Also, there has been developed new architectures for detectors as the barrier structure nBn detectors or the multi-stage/cascade infrared detectors. These new architectures are implemented in the traditional materials in order to improve its performance, as is the case of the state-of-the-art T2SL nBn barrier detectors [45].

At the moment, the research in infrared detectors is directed towards photodetectors operating at high temperature (larger than 130 K). On the other hand, thermal detectors have reached also a very important relevance due to its low cost and small size. Their performance still lower than photodetectors, but there are projected to be in the near future real competitors of the photodetectors.

2.4 Figures of merit of infrared detectors

Before entering into detail with the classification of infrared detectors, the main parameters that characterize them will be introduced. These main parameters are known as the detector figures of merit due to its relevance. Nevertheless, there are several other parameters of huge importance and they will be defined in Chapter 5. As will be seen, this large number of different parameters is one of the reasons for the complexity of characterization of infrared detectors.

2.4.1 Responsivity

It is defined as the detector electrical output signal per unit of incident radiation power (input signal photon power). The ideal case is a maximum value of responsivity [24]. Within this definition, is possible to find two concepts:

- **Voltage responsivity, R_V:** is the detector output voltage per incident radiation power. The units are [V/W].
- **Current responsivity, R_I:** is the detector output current per incident radiation power. The units are [A/W].

These two parameters can be expressed according to Equations 2.4 and 2.5 [46].

$$R_V = \frac{V}{P \cdot A} \tag{2.4}$$

$$R_I = \frac{I}{P \cdot A} \tag{2.5}$$

Where P is the incident energy from the source per area [W/m^2], A is the pixel active area [m^2], calculated as the pixel pitch horizontal dimension times the pixel pitch vertical dimension times the fill factor. The fill factor is the percentage of the pixel sensitive to the light (usually in the order of 0.8). The signals V and I are expressed in [V] and [A], respectively.

The responsivity is also known as spectral response or spectral responsivity when it is defined in function of the wavelength of the incident radiation beam [46] [24]. Therefore, the best is to have a maximum value in the desired wavelength range and zero outside of it. In photodetectors, ideally, the spectral response varies linearly proportional to the wavelength, as illustrated in Figure 2.3. For photodetectors, the spectral response can be expressed with Equation 2.6 [24].

$$\mathrm{R}_\lambda = \frac{\eta \mathrm{q} \lambda}{\mathrm{hc}} = \frac{\eta \lambda}{1.24} \tag{2.6}$$

Where h is the Planck's constant [J $\cdot$ s], c is the speed of light in vacuum [cm/s], q is the electron elementary charge [C, coulombs], η is the quantum efficiency [%], and λ is the wavelength [m]. The spectral response is in [A/W].

On the other hand, the spectral responsivity of thermal detectors is independent of the wavelength, as represented also in Figure 2.3. The limit of the spectral response will be given by the spectral response of the material of the window in front of the detector.

A very important aspect is that the responsivity measured in the ground, will not change with the altitude. The same occurs with the specific detectivity D^*, that will be later presented. These two parameters change with the wavelength but are not dependent on the radiation received. Therefore, once computed with specific values in the ground, it will be possible to use the same responsivity in space to compute any of the other parameters that are unknown. This was one of the conclusions reached in this project after several experiments and analysis of different detectors.

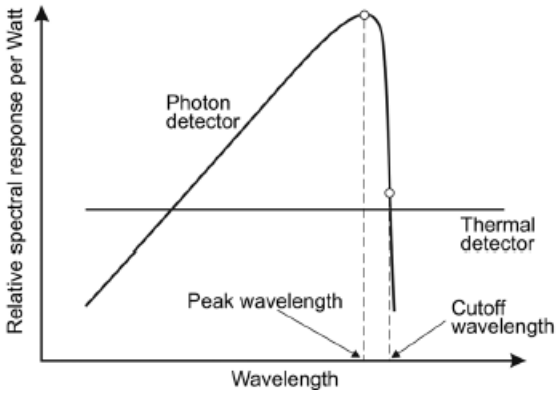

Figure 2.3: Responsivity vs. wavelength for photodetectors and thermal detectors in the infrared. [2]

2.4.2 Spectral range. Cut-off wavelength

The previously discussed spectral response, increases linearly with the wavelength, as indicated, until a limit wavelength. The so-called cut-off wavelength. It can be seen that photons with $\lambda > \lambda$ cut-off are not absorbed by the detector's material and therefore, these photons are not detected. A value for the cut-off wavelength is obtained with the definition of the detector's material energy gap, ϵ_{gap}, Equation 2.7 [24].

$$\lambda_{\text{cutoff}} = \frac{h \cdot c}{\mathcal{E}_{\text{gap}}} \tag{2.7}$$

Where h is the Planck's constant [J· s], c is the speed of light in vacuum [m/s] and ϵ_{gap} the energy gap in [eV] defined in Equation 2.8.

$$\epsilon_{gap} = \frac{h \cdot c}{\lambda_{cutoff}} \cdot \frac{1\text{eV}}{1.6 \cdot 10^{-19}\text{J}} = \frac{1.24}{\lambda_{cutoff}} \tag{2.8}$$

Additionally, it is observed that photons arriving in the cut-off wavelength range, have an energy equal to the material energy gap [46]. It is a value of great importance since the best performance of the detector is located in this range. As a remark, in order to avoid confusion, when the manufactures indicate in their datasheets the spectral range of the photodetector, the highest value of this range is mostly all the times the cut-off wavelength.

2.4.3 Quantum efficiency

This parameter defines the number of incident photons converted to electrons (photocarriers) in a photodetector, i.e. the capability of a detector to convert light energy to electrical energy, expressed as a percentage. Larger values of quantum efficiency η are desirable, taking into account that this figure is very dependent in the wavelength range [47]. The quantum efficiency can be expressed as in Equation 2.9 [46] [6].

$$\eta = \frac{h \cdot c}{q} \cdot \frac{R_I}{\lambda} = 1.24 \cdot \frac{R_I}{\lambda} \tag{2.9}$$

Where R_I is the current responsivity of the photodetector [A/W], h is the Planck's constant [J·s], c is the speed of light in vacuum [m/s], q is the electron elementary charge [C, coulombs], and λ the wavelength [m].

In order to maximize the quantum efficiency in a detector, is necessary to increase the absorption coefficient of it and reduce the reflection in the detector's front area or increase it on the back side [46]. Figure 2.4 includes a comparison of the quantum efficiency's for the different photodetectors that will be discussed in this chapter.

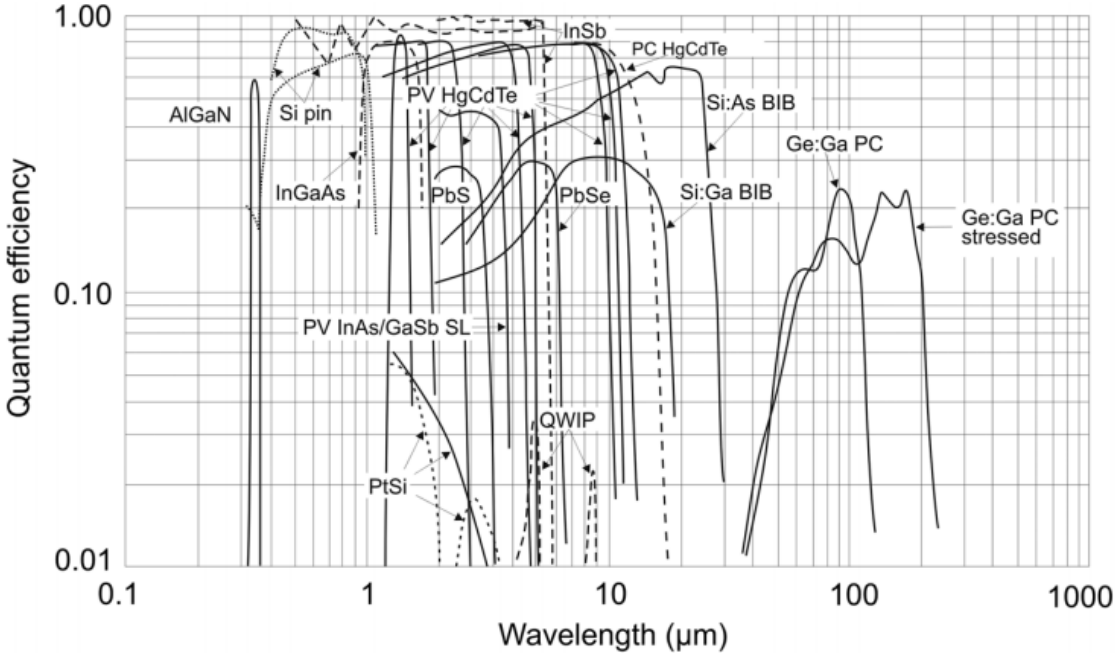

Figure 2.4: Quantum efficiency vs. wavelength for the main categories of photodetectors. [3]

This concept is not applicable for thermal detectors since the photons that reach the thermal detector are not converted to electrons like in photodetectors. Thermal

detectors, for instance, measure the change of a physical property due to the heat of the incoming radiation.

2.4.4 Detectivities

2.4.4.1 Detectivity, D

It is the inverse of the Noise Equivalent Power, NEP, which is defined as the amount of absorbed power in the detector that generates on it an output signal equal to the detector noise [46]. D can be described according to Equation 2.10. It is expressed in [$Hz^{1/2}$/W]

$$D = \frac{1}{NEP} \tag{2.10}$$

2.4.4.2 Specific Detectivity, D^*

In general, the specific detectivity, D^*, is defined as the photosensitivity per unit of active area and unit of bandwidth of a detector. It also can be understood, as the signal SNR (Signal-to-Noise-Ratio) for an incident radiation power of 1 W on a 1 cm^2 area of the detector and 1 Hz bandwidth. These two definitions are illustrated into Equation 2.11, [46] [24].

$$D^* = \frac{\sqrt{A\Delta f}}{NEP} = \frac{\sqrt{A\Delta f}}{P} \cdot SNR \tag{2.11}$$

Where P is the incident energy from the source [W], A is the active area of the pixel in [cm^2] and Δf is the frequency bandwidth, in [Hz], at which the circuits of the detector operates. The unit of D^*, [cm$\cdot$ Hz $^{1/2}$/W], is also called Jones.

It represents one of the main figures of merit of infrared detectors to describe its performance, most commonly used than the NEP. In addition to this, it is a very useful parameter in the comparison of different detectors, because it is defined per unit of area and unit of frequency bandwidth [24] [46].

As it was explained in the responsivity parameter, one of the conclusions reached is that the responsivity and specific detectivity do not change with the altitude. The specific detectivity and responsivity for a detector with the same conditions of temperature (of the detector) and wavelength range are equal into their respective values in space. Therefore, when the SNR is increased, D^* will not increase, not only because an increase in SNR is due to a higher incident energy, P (dividing in Equation 2.11);

but also because the SNR increase suppose the variation of other parameters of the optical design, like the diameter of the pupil. At the end, the D^* will remain constant. This assumption is covered at Section 5.6 about the noise description.

Largest values of D^* are desired. In addition to this, in general, the value of D^* increases with the wavelength until the same limit that was constraining the responsivity. This limit is the cut-off wavelength of the infrared detector material. Which was described as the optimum wavelength for the detector operation, and correspond to the largest value of the SNR [46]. The manufacturers usually provide with this D^* peak at the cut-off wavelength, and in order to calculate the value of D^* at any wavelength, the Equation 2.12, [24].

$$D^*(\lambda) = D^*_{\text{peak}} \cdot \frac{\lambda}{\lambda_{\text{cutoff}}} \tag{2.12}$$

Moreover, it is also possible to increase the specific detectivity by maximizing the detector photon absorption and by optimizing the detector carrier time and transit time [46]. The different values for the specific detectivity, depending on the type of material of the infrared detector and the wavelength of operation will be illustrated in Figure 2.17.

2.4.4.3 D double Star. D^{**}

It is defined as the specific detectivity, D^* per an angle . Its value is independent of the field of view, FOV, of the infrared imager system. It can be expresed according to Equation 2.13, [46]. The units are [cm$\cdot$ Hz $^{1/2}$ $\cdot$ sr$^{1/2}$ /W]

$$D^{**} = D^* \sin\theta \tag{2.13}$$

2.4.5 Response time

It is defined as the interval of time that the detector response (detector output signal) needs to reach 63 % of its maximum value, after an input of infrared radiation. Moreover, it is also defined as the time for the signal output to decrease to 37 % of its maximum value after the input signal is switched off [46].

Small values of the response time are better, and zero is the ideal figure. The concept of response time is equal for thermal detectors and photodetectors, nevertheless, it is calculated differently for each one. In the case of photodetectors, the following expression of Equation 2.14,[24], is used.

$$|R| = \frac{v_0 \tau}{\sqrt{1 + (2\pi f \tau)^2}} \tag{2.14}$$

Where $|R|$ is the modulus of the responsivity [V/W], v_o is the initial value in [V] of the output voltage signal of the detector (since it varies with time once illuminated by an incident radiation pulse), and f is the frequency at which the electronics of the detector operate [Hz]. The unit of the response time τ is [s].

In the case of thermal detectors, the response time, time to reach 63 % of the final signal, is also known as thermal time constant τ_{th}. It is written according to Equation 2.15, [48].

$$\tau_{th} = \frac{C_{th}}{g} \tag{2.15}$$

Where C_{th} is the thermal capacity of the material of the detector in [J/K], and g is the thermal conductivity of the cited material in [W/K].

The importance of the thermal time constant (response time) of thermal detectors, is that it is approximately 1/3 of the total time needed to reach 95 % value of the total maximum output signal. The time to reach 99 % of the output signal is approximately 5 times the thermal constant, [49] and Xenics old website. As a remark, this definition is not used in the case of photodetectors, since the time constants are very short. The interval of time for reaching 99 % of the steady-state for photodetectors can be approximated as a step function. In the case of thermal detectors, it is approximated as an exponential function, illustrated in Figure 2.5. The response time (time for the 63 %) of photodetectors is in the order of microseconds while for thermal detectors is between 5 ms to 15 ms, from the detectors offered by the main manufacturers of infrared detectors.

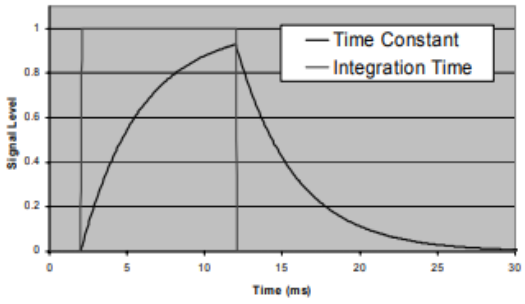

Figure 2.5: Differences bettween the exponential response time function of thermal detectors and the step response time function of photodetector.

The thermal time constant is a fixed value and cannot be reduced even cooling down the detector. It is dependent on the size of the pins of the bolometer (a type of thermal detector) surface, and therefore it can be reduced only by micromachining techniques in the production process.

In addition to this, it is important not to confuse the response time with the saturation time of pixels of the detector. The saturation time is the time for the pixel to reach an overexposure state where it has no more storage for integrating more arriving photons.

2.5 State of the art of photodetectors and thermal detectors. Space applications.

Once the infrared detectors and their figures of merit have been presented, is possible to enter in detail in the different types of materials and architectures that characterize the photodetectors and thermal detectors. This section will be oriented into the main advantages and disadvantages of the different types of infrared detectors, comparing them with the most used detector in their category, and presenting its degree of developing.

2.5.1 Photodetectors

The photodetectors were presented as devices that convert an incident flux of infrared radiation into a current to be later read-out in the circuit module. A read-out that differs between the main architectures of photodetectors, which are photoconductors and photodiodes (inside of the group of photovoltaic sensors). The read-out procedure is very important for the determination of the noise and therefore will be treated in detail Chapter 5 about the signal-to-noise ratio.

It was discussed how the responsivity of photodetectors increase with the wavelength until the cut-off frequency. Photons with a higher wavelength will not be detected. Therefore, it is very important to select the material for the FPA that present the best performance in the desired band of observation.

Another main advantage of a photodetector is their great values of response time and their high sensitivity [2]. The response time of modern photodetectors is in the order of a few milliseconds, or even in the range of microseconds. That is why the response time of photodetectors is usually represented as a step and not as an

exponential function. This will be a very important aspect to take into account in the most demanding applications.

Moreover, photodetectors are characterized by low noise, and therefore high-signal-to-noise ratio, but as mentioned before, the noise is very dependent on the circuit module.

On the other hand, the price to have these good characteristics is that photodetectors need to be cooled, operating at very low temperatures. Therefore, they occupy more space in the optical system since a cooler need to be attached to them. Nevertheless, they are becoming smaller with time. Some of the latest photodetectors modules are around 70 mm large, like the new 'Neutrino Swap-C' from FLIR operating in the mid-wave infrared [38], which made them very suitable to be used in a CubeSat.

As a remark, it is very common to find the term BLIP associated with photodetectors. Ideally, the operation of photodetectors is limited by the fluctuation in the number of photons of the signal emitted by the specific observed target. However, the target is within a background with specific temperature and, therefore, the discernible signal by the detector will be limited by the fluctuations of this background radiation. In these conditions, the photodetector is said to be BLIP, which means Background Limited Infrared Photodetector, [24]. In reality, BLIP conditions are also very difficult to achieve due to the internal processes of the detector that are also limiting the sensitivity of it.

The following subsection will cover the different types of materials and architectures for the infrared optical photodetectors.

2.5.1.1 Intrinsic detectors

It represents the group of higher importance in the infrared detection field. Within this category is the ternary alloy HgCdTe. They offer a high performance of detection due to their strong absorption of the infrared radiation. This strong absorption is due to the narrow bandgap between the valence band and the conduction band of the semiconductor. They are comparable less noisy than extrinsic detectors, and therefore they are lower constrained by the cooling [6]. It is possible to find intrinsic detectors in the range between 1 μm and 20 μm.

2.5.1.1.1 InGaAs photodiodes. III-V material.

Within the group of photovoltaic detectors, is possible to find the p-n junction photodiodes. A p-n semiconductor allows the electric current to go only in one direction, from the valence band to the conduction band as it can be seen in Figure 2.6, [4].

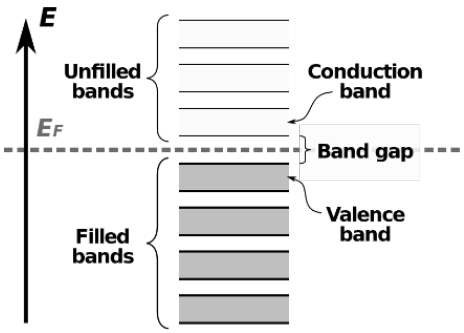

Figure 2.6: Representation of the valence band and the conduction band of a p-n semiconductor. [4]

InGaAs is a very suitable detector material for the near-infrared, from 1.0 μm to 1.7 μm [2]. It can be matched with InAs to be sensitive until 3.7 μm wavelength [44]. Over the range from 1.0 μm to 1.7 μm, the quantum efficiency reaches a very high value close to 80 %, [7]. The cooling requisites are low due to the short wavelength of operation. The FPA temperatures will be no lower than 100 K. Standard InGaAs detectors with a 1.6 μm cut-off wavelength have also high values of specific detectivity, D^*, of around 10^{13} cmHz$^{1/2}$W^{-1}. Moreover, the current responsivity is close to 1 A/W for the standard model, [6].

These properties make InGaAs the detector of reference for the short wave infrared SWIR, overpassing the performance of the HgCdTe detectors, in terms of sensitivity and quantum efficiency for the similar range, beside have a lower cost [6]. Recently, in April 2019, an InGaAs detector has been used in the 'Hello World Nano satellite' developed by Finland. The detector is the 'Cardinal 640 Loon' offered by the Israeli manufacturer SCD, offering a pixel pitch of 15 μm and FPA size of 640x512 pixels.

Other examples of space missions in which InGaAs detectors have been used are the Descent Imager/Spectral Radiometer (DISR) instrument aboard the CassiniHuygens mission to Titan and in the multispectral instrument of the ProbaV satellite, which implemented a combination of three InGaAs 1024 pixels linear arrays. These detectors experienced a noticeable pixel degradation in space what conduced to an increase of the dark current and therefore a loss in the detection capabilities, [33]. The dark current is the flux of charge circulating in the detector even when it is switched off.

2.5.1.1.2 InSb detectors, III-V material

2.5.1.1.2.1 InSb Photoconductor detectors

A photoconductor is a radiation sensitive resistor, in general, a semiconductor, which operates measuring the increase in the electrical conductivity due to an incident flux of photons. This change is sampled due to a number of electrodes attached to the FPA. As explained in Section 2.3.2, photoconductors offer a lower performance compared with photodiodes and therefore their importance has plunged over the last two decades.

The operational wavelength range of InSb photoconductors is from the SWIR to the MWIR. The FPA need to be cooled to around the reference temperature of 77 K. At this temperature and with a cut-off wavelength of 5.3 μm, the specific detectivity has a value between $5{\cdot}10^{10}$ cmHz$^{1/2}$W^{-1} and 10^{11} cmHz$^{1/2}$W^{-1}, [6].

Additionally, these detectors were also used at room temperatures, suffering from a decrease in the detectivity until a value close to $2.5{\cdot}10^{8}$ cmHz$^{1/2}$W^{-1}, [6].

2.5.1.1.2.2 InSb Photoelectromagnetic detectors (PEM)

PEM InSb detectors appeared as a result of the research into sensors operating with a good performance at room temperature. The problem with these detectors is that they have their peak of responsivity between 5.5 μm and 6.5 μm,[6], which is outside of the atmospheric window of interest for the OUFTI CubeSat mission.

As a remark, the response time of these detectors is very small, around 0.2 μs, but it has not been possible yet to extend its range of detection further than 8 μm without cooling, [6].

2.5.1.1.2.3 InSb Photodiode detectors

During the last two decades, InSb photodiode detectors have been a reference for the ultraviolet UV to about 5.5 μm range of the electromagnetic spectrum. Nevertheless, in the short wavelength infrared (SWIR) range they need to be cooled to about 80 K to operate. As a result, InGaAs is usually the detector of choice for this range, since InGaAs can operate at temperature larger than 100 K [2].

A key factor in InSb photodiodes is that they offer an extraordinary quantum efficiency above 90 % for its whole range of detection. The operation temperature is, as mentioned before, between 60 K and 80 K. At this temperature, the values of dark current are very low, around 0.004 electrons per second in the modern InSb detectors offered by manufacturers as the Israeli SCD or the Americans Raytheon and Santa Barbara Focalplane [7]. These detectors present specific detectivity values around 10^{11} $cmHz^{1/2}W^{-1}$ for the MWIR range between 3 μm and 5 μm [6].

Additionally, is possible to find very large InSb arrays in the market, as the 'Blackbird 1920' from SCD with an FPA of 1920x1536 pixels and 10 μm pixel pitch [5]. Nevertheless, it has a big size, what could make it not compatible with a small CubeSat. Other InSb detectors will be compared in Chapter 7 as the small size SCD 'Pelican D 640' illustrated in Figure 2.7.

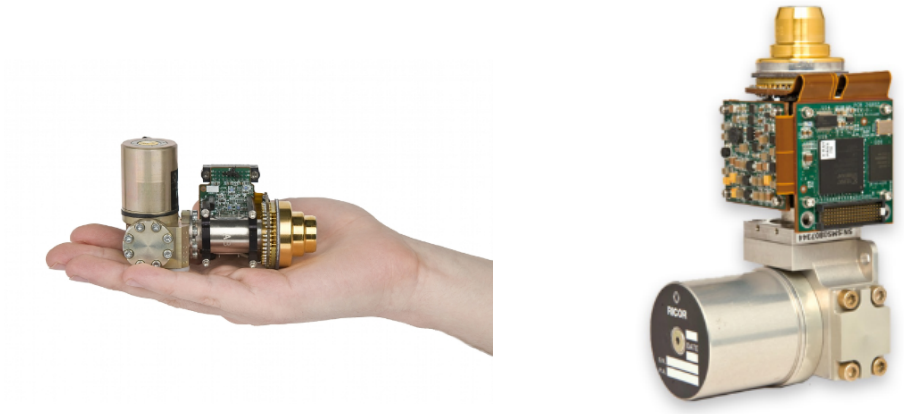

Figure 2.7: InSb 'Pelican D 640' photodetector from SCD. 640x512 pixels, 15μm pixel pitch for the 3.6 μm to 4.9 μm infrared range. [5]

Comparing InSb with HgCdTe detectors, both of them offer excellent characteristics in the MWIR range. Nevertheless, InSb could be limited by its fixed cut-off wavelength of 5.5 μm, in contrast with the tunable capability of HgCdTe detectors for the wavelength of interest [44]. Another disadvantage is that in InSb detectors the performance quickly drops at temperatures higher than 80 K as a difference of HgCdTe detectors which can operate at higher temperatures [6]. In addition to this, the dark current for the same temperature and wavelength is higher than in HgCdTe detectors due to the fabrication process [44].

The cooling characteristics and dark current in comparison with HgCdTe detectors, where the reason why they were discarded for the James Web Space Telescope. In

order to not risk the thermal design, the HgCdTe detector was selected for the JWST [33].

On the other hand, InSb offers a higher uniformity over the range of operation besides a significantly lower cost per pixel in comparison with HgCdTe detectors. Therefore they are a good choice for large FPA applications or for example when the budget of the mission is a constraint and detection capabilities does not need to be the highest [33].

2.5.1.1.3 HgCdTe detectors. II-VI material

2.5.1.1.3.1 HgCdTe photoconductor detectors

As mentioned in the historical background, HgCdTe detectors have been the detector of reference for the infrared region in the last four generations of detectors. The photoconductor HgCdTe detectors highlighted in the first generation, operating at temperatures from 77 K until 200 K with respective specific detectivities of 10^{12} cmHz$^{1/2}$W^{-1} and 10^{10} cmHz$^{1/2}$W^{-1}. These values are higher than the ones offered by InSb photoconductors for the same conditions. But due to the advances in photodiode detectors, photoconductor HgCdTe detectors were relegated to a second place, [6].

2.5.1.1.3.2 HgCdTe photodiode Detectors

One of the main reasons for the success of HgCdTe detectors is that they can operate in a wavelength range that starts in 1 μm and extends further than 20 μm, [7] [44]. Moreover, within this range, HgCdTe infrared detectors offer extreme flexibility to select the wavelength of interest and set-up the desired cut-off wavelength. The values of the quantum efficiency are higher than 70 % and remain uniform over the whole infrared range. Additionally, its quantum efficiency can be increased by 90 % by the use of an antireflection coating [12].

HgCdTe photodiode detectors are mainly used for high-performance applications. In the SWIR range, their performance in comparison with InGaAs detectors is slightly lower as presented before. They have high specific detectivities, close to 10^{13}cmHz$^{1/2}$W^{-1}, but not higher as in the case of InGaAs detectors [6]. Nevertheless, since InGaAs photodiodes do not work in higher wavelengths than 1.7 μm, in some missions as ESA's

Euclid satellite the detector of choice was HgCdTe to have a wider range in the infrared [33]. But is important to take into account that HgCdTe detectors have always the highest cost. Additionally, in comparison with InSb photodiodes for the SWIR, HgCdTe detectors were also better because of the temperature constraints of InSb detectors.

For the case of the MWIR region, HgCdTe photodiodes operate at temperatures around 77 K, but their drop in performance at higher temperatures is not as pronounced as it was in InSb detectors [7]. The values of specific detectivity, D^*, in the infrared are illustrated at Figure 2.17, where it will be possible to see how HgCdTe figures of sensitivity are slightly higher than the $10^{11}\text{cmHz}^{1/2}\text{W}^{-1}$ values of InSb detectors.

HgCdTe MWIR FPAs are used in the cutting-edge MIRI instrument for the James Web Space Telescope. The detector is the Teledyne's HgCdTe 'HAWAI-2RG'. A detector selected due to the low dark current values, which make it very suitable for the observation of faint astronomical bodies [33].

Finally, LWIR HgCdTe detectors are commonly used in Earth observation and meteorological payloads. This is for example the case of the ESA's Meteosat Third Generation Imaging Satellite (MTGI), which implemented an LWIR HgCdTe detector from the French manufacturer Sofradir into its Flexible Combined Imager (FCI) instrument [33].

Nowadays, SWIR, MWIR and LWIR HgCdTe arrays, implemented into CMOS ROICS, are commercially available from several manufacturers. They offer big FPAs sizes into smaller detector cores including the cooling systems. This is, for example, the case of the 3.7 μm to 4.8 μm detector 'Daphnis-XGA MW RM2/K563', 1024x768 pixels and 82 mm long (cooler included) from SCD detectors [5]. Furthermore, HgCdTe detectors have response times in the order of μs what make them very suitable for demanding space mission [33].

2.5.1.1.4 InAsSb detectors. III-V material

2.5.1.1.4.1 InAsSb photoconductor detectors

InAsSb detectors with the photoconductor architecture show larger performances than HgCdTe photoconductors. Used for the MWIR, specific detectivities of $3 \cdot 10^{10}$

$cmHz^{1/2}W^{-1}$ could be obtained at a wavelength at 5.4 μm, which are slightly lower than InSb photoconductors, but can be obtained at higher temperatures [6].

The quantum efficiency of InAsSb photoconductors is close to 50 %. The response times are very low, in the order of ns, additionally, they can also operate in the LWIR, 8 μm to 14 μm range [6].

2.5.1.1.4.2 InAsSb photodiode detectors

They are very high-quality photodiode detectors in terms of the stability of the chemical bonds of the ternary alloy. HgCdTe is weaker in this aspect what could eventually derive into non-uniformities in its operation [45].

The quantum efficiency values are between 40 % and 60 % and the operating temperatures around 77K. In comparison with the HgCdTe detectors, they present the disadvantage of higher values of dark current and therefore lower signal-to-noise ratio [6]. InAsSb detectors are developed and manufactured mostly with the barrier structure that will be discussed in Section 2.5.1.7.

2.5.1.2 Extrinsic detectors. Si:As, Si:Ga photoconductors and Si:As blocked impurity band detectors (BIB)

The second group of infrared detectors, extrinsic detectors, is split into two categories. The first category is the Si:As and Si:Ga photoconductors, also known as photoresistors. The second category, the blocked impurity band detectors (BIB). The BIB architecture present similitudes to the photodiodes but the internal photoexcitation of the electrons is carried on in a different way between the semiconductor bands. Due to the difference in performance between both types of structures, [7], only the BIB structure will be presented.

Extrinsic BIB detectors are highly constrained by the cooling requisites, as mentioned in the description of intrinsic infrared detectors. They operate at temperatures between 8 K and 10 K in order to reduce the internal circuit noise [7].

Si:As BIB detectors operate in a wavelength range that starts in 2 μm and continues until 30 μm. Modern Si:As detectors, can reach wavelengths of more than 100 μm. Its quantum efficiency is about 60 % for the wavelengths higher than 10 μm, but it drops in the shorter wavelengths [2] [33]. Therefore is an adequate detector for LWIR imaging, offering better detectivity figures in comparison with LWIR HgCdTe photodiode detectors but with the limitation of the temperature [7].

An important aspect is that they are very useful for space applications. That is because they are very sensitive to low-background fluxes. Furthermore, their internal structure gives them hardness under cosmic rays and other radiation effects of the space environment [2] [45]. Due to these properties, they were also selected to be implemented in the MIRI instrument of the JWST for the 5 μm to 30 μm wavelength range [33]. In the case of terrestrial operations, they do not offer and advantage over HgCdTe and InSb detectors.

At the moment, the temperature of operation of Si:As extrinsic BIB detectors is not compatible with the CMOS read-out circuits [33].

2.5.1.3 Photoemissive metal silicide Schottky-barrier detectors, PtSi.

The third group of infrared detectors is formed by the photodiode Schottky-barrier detectors. Until now, the photodiodes were of the type p-n junction. Scottky-barrier is a new architecture characterized by its major simplicity besides better response times and the possibility to be used in larger bandwidths.

The most common type of Scottky-barrier photodiodes is the PtSi detector. Sensitive in the wavelength range between 3 μm to 5 μm. They are characterized by a very good uniformity along with the detection range besides large pixel fill factors of 71 %. The fill factor of an image sensor array is the ratio of the pixel light-sensitive area to its total area [6].

Nevertheless, they present a major drawback that makes them totally not useful for the space mission of this project. They present a quantum efficiency of the order of 1 %, which is not compatible with the low number of photons in the infrared that the CubeSat will be receiving. That is why PtSi detectors are relegated to only some specific ground missions [6] [12].

2.5.1.4 Quantum Well Infrared Photodetectors (QWIP). Type I GaAs/AlGaAs, InGaAs/ AlGaAs photoconductors.

The quantum well structure is formed in semiconductors when a material, for example, the alloy GaAs, is introduced between two layers of a material with a wider bandgap, as is it could be the case of aluminium or indium. As a result, AlGaAs and InGaAs QWIP detectors are obtained [12].

QWIP detectors commonly appear as photoconductor detectors. Even in this type of internal architecture, they have advantageous characteristics as low power

consumption, the possibility of large FPAs fabrication, or their use in applications where it is requested a long integration time [6].

QWIP photoconductors cover the infrared MWIR and LWIR regions, with an easy wavelength control, operating at temperatures in the range of 40 K to 100 K. The values of the specific detectivity are between 10^{10} $cmHz^{1/2}W^{-1}$ and 10^{11} $cmHz^{1/2}W^{-1}$, lower than in the case of HgCdTe detectors in its photodiode mode. Their performance in the LWIR range is also lower in comparison with LWIR HgCdTe detectors for the same temperature and detection bandwidth. The dark current of LWIR QWIPs is approximately two orders higher than in LWIR HgCdTe sensors [7] [45].

But the most important drawback is the quantum efficiency. With a value of 10 % at around 77 K. The response time in in the order of milliseconds what makes them considerably slower in comparison with the other MWIR detectors that have been discussed before [45]. For a space mission, the shorter the response times the better in order to match which the integration time of the satellite.

Nevertheless, they offer an interesting property which is the possibility of multi-colour imaging. To capture two bands at the same time. NASA/JPL, has recently implemented a QWIP multicolour detector in one of its upcoming satellite missions. The Hyperspectral Infrared Imager (HyspIRI) mission. The instrument utilized is the Hyperspectral Thermal Emission Spectrometer (HyTES) detecting in the range of 7.5 μm to 12 μm, [33].

The most common FPA size is 640x512 pixels and 640x480 pixels, and it is offered by the Americans FLIR and Raytheon or the Belgian Xenics, among others like the German AIM, [37] [50] [38].

Moreover, photodiode QWIPs are currently in development oriented to operate in the LWIR region.

2.5.1.5 Quantum-dot infrared photodetectors (QDIP) and DWELL detectors. InAs/GaAs, InGaAs/InGaP, Ge/Si photoconductors.

QDIP detectors represent one of the most promising technologies for overpassing the performance of HgCdTe detectors in the near future. Their capability of detection goes from the MWIR to the LWIR at temperatures between 77 K and 200 K or higher [51]. They are developed as photoconductors, surpassing the behaviour of InSb and HgCdTe photoconductors for the same range of operation [6].

In addition to this, QDIP photoconductors operating at high temperatures, large than 200 K, show sensitivity values bigguer than HgCdTe with the photodiodes architecture at the same temperature; as it is illustrated in Figure 2.8a). On the other hand, at lower temperatures the experimental detectivity figures of QDIPs photoconductors do not present an advantage over HgCdTe photodiodes 2.8b).

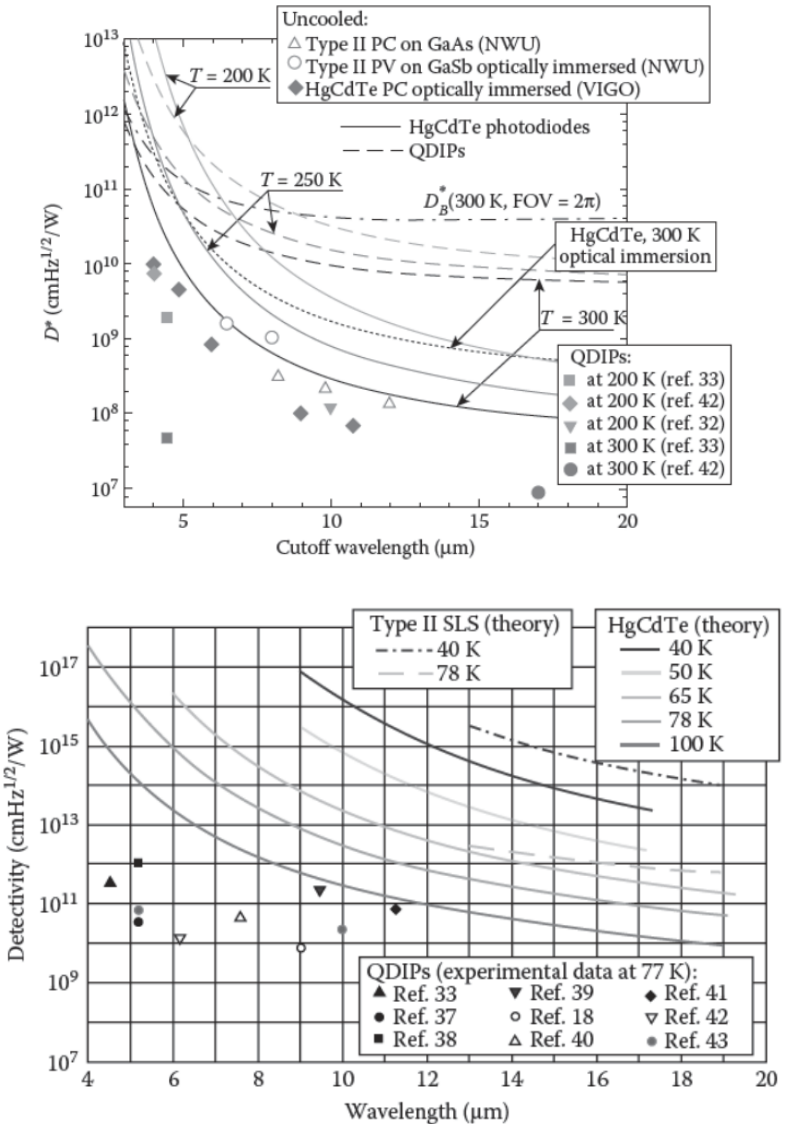

Figure 2.8: Comparison of the specific detectivity in function of the wavelength for QDIP, HgCdTe and T2SL photodetectors at a)high temperatures and b)low temperatures.[6]

In comparison with QWIP photodetectors, QDIP photoconductors have large values of quantum efficiency around 35 % at 4.1 μm, besides lower values of dark current and higher signal-to-noise ratios SNR. Nevertheless, the noise figures are bigger than

HgCdTe detectors at low temperatures [12].

It is, therefore, a very promising detector to closely follow in its development for the possibility of use at very high temperatures or even uncooled, what may be interesting in future CubeSat missions at CSL.

As a remark, and with the purpose of covering the whole range of infrared detectors, the DWELL detectors are also presented. They are a combination of QDIPs and QWIPs detectors, in which an InAs QDIP is embedded into InGaAs QWIP. This architecture is also known as dot-in-a-wall heterostructure. They provide with higher values of sensitivity, responsivity and dark current than the individual QDIPs and QWIPs [6] [12].

2.5.1.6 Strained layer superlattice (SLS) Detectors.

The concept of superlattice refers to a structure made of layers of different materials one over the other. Strained refers to the procedure of fabrication. These definitions form the so-called strained layer superlattice detectors.

Is possible to find three types of SLS detectors depending on the materials used. The first group is formed by the Type I InAsSb/InSb SLS detectors, characterized by rather low detectivities in comparison with usual InAsSb photodiodes. The third group, are the Type III HgTe/HgCdTe SLS, which development was stopped since they never reached the performance of HgCdTe photodiodes as it happens in Type I SLS. Nevertheless, the second category, Type II InAsSb/InSb SLS are very promising and huge results have been obtained, with a performance close to the HgCdTe detectors [6].

2.5.1.6.1 Type II InAs/GaInSb SLS photoconductors and photodiodes. III-V materials.

As an introduction, is important not to confuse the T2SL detectors with the nBn barrier T2SL detectors, that will be presented in Section 2.5.1.7, built with a different internal architecture.

T2SL detectors appear with the structure of photoconductors and photovoltaic diodes. The following description is for T2SL photodiodes. These detectors cover a wide range of the infrared radiation, from MWIR to wavelengths around 25 μm. Their cut-off wavelength can be easily tuned in this range, as it was possible with HgCdTe

photodiodes. Besides this, T2SL present an advantage over HgCdTe detectors, for T2SL photodiodes is not necessary to change the material composition in the tuning of the cut-off wavelength what reduces the costs of production. Their stability in terms of uniformity of operation is also higher than HgCdTe photodiodes [7] [52].

The quantum efficiency of T2SL is around 40 % to 60 % in the MWIR at 77K, and about 20 % to 50 % in the LWIR also at 77K [53]. Which are lower quantum efficiency than InSb photodiodes (90 % QE) for the MWIR and lower than HgCdTe photodiodes for both regions (70 % QE).

At Figure 2.8, it was possible to see how T2SL detectors had theoretical greater detectivity figures in the LWIR region, in wavelength larger than 14 μm, in comparison with HgCdTe photodiodes. It was the case also for extrinsic detectors, Si:As and Si:Ga which higher detectivities than HgCdTe detectors in the LWIR.

T2SL have reached an impressive development in the last years, but at the moment, their performance still slightly worse than HgCdTe detectors, not reaching yet the theoretical performance [52]. Despite this, several manufacturers already offer TSL2 detectors, as the 'IRNova 640-MW' detector for the range 3.5 μm to 5 μm, with an FPA size of 640x512 pixels and excellent value of NEDT below 20 mK (Section 5.5.2), offered by the manufacturer IRNova in Sweden [54].

In addition to this JPL/NASA has reached great advances into the development of an LWIR (11.5 μm cut-off wavelength) 1024x1024 pixels FPA [55]. The T2SL detectors are clearly an option to take into account for future CubeSat missions due to its high operating temperatures, low power consumption, and cost in comparison with HgCdTe detectors.

2.5.1.7 Barrier nBn and pBn detectors

Barrier detectors with nBn and pBn designs are a hybrid between photoconductor and photodiode. It provides superior performance in comparison with traditional p-n junction photodiodes. The term 'barrier' refers to its property to reduce the surface unwanted leakage current. That allows to also reduce the dark noise, in way that the input signal is not affected. The barrier is made by the use of three layers. For the nBn structure, a wide-gap barrier layer (B) is introduced between two narrow-gap n-type (n) layers, one receives the infrared radiation and the other acts as an absorber. Analogous design for the pBp structure [56].

The nBn and pBp barrier structures have been implemented over the last years in many of the materials alloys discussed in previous sections. Therefore, is possible to find InAsSb, T2SL or HgCdTe nBn/pBp barrier detectors. The main advantage of barrier detectors is that they have a great signal-to-noise ratio at lower temperatures, in comparison with a photodiode at the same temperature, and therefore they can operate also at higher temperatures with lower dark currents [56] [57]. Other advantages are next presented.

As a remark, is important to not confuse the concept of barrier detectors, with the concept of unipolar barrier photodiode, which is a technology in research to reduce the dark current in traditional photodiodes.

2.5.1.7.1 Type II superlattice (T2SL) nBn/pBn barrier detectors

It was already discussed the importance of Type II superlattice detectors for the upcoming years as a substitute of HgCdTe detectors. This idea became even more solid after the implementation of the barrier structure on the type II InAs/GaInSb materials.

The wavelength range covered by T2SL nBn/pBn barrier detectors goes from the SWIR to the LWIR. The latest developments efforts are for the MWIR range since theoretical performances of T2SL in the LWIR were already better than HgCdTe photodiodes [56] [7].

At the moment, T2SL barrier detectors are already offered by some manufacturers. This is the case of the LWIR 'Pelican-D LW' T2SL pBn detector, developed by SCD. It operates at 77 K with a quantum efficiency higher than 50 %. The cut-off wavelength is 9.3 μm and the FPA size is 640x512 pixels [5].

In addition to this, the Jet Propulsion Laboratory, in California, has developed also an extraordinary T2SL barrier detector. The 'HOT-BIRD' detector. BIRD refers to barrier infrared detector. It is an MWIR detector, from 4.08 μm to 5.3 μm, operating at temperatures higher than 150 K. It has been designed for multispectral observation in 625 bands. But the most impressive aspect is that it has been developed to be used in the CubeSat 'CIRAS', to be launched in 2019 [30]. This CubeSat will be analysed in Section 6.2, but for the moment is possible to state that its detector is the best reference for the future OUFTI CubeSat mission.

Another example of T2SL barrier detectors is the 'Neutrino SWAP+C HOT FPA' from the American FLIR. At the moment, it is one of the most promising detectors for the OUFTI mission. It operates at 130 K in the range from 3.4 μm to 5 μm. Additionally, it has a compact size of 74 mm large and an FPA size of 640x512 pixels and 15 μm pixel pitch [38].

In spite of this, T2SL barrier detectors still on research. At 2017, their dark current and NETD values still higher than the cutting-edge HgCdTe photodiodes. In Figure 2.9 it is shown the Noise Equivalent Power Difference, NETD, of T2SL nBn/pBp detectors for the MWIR and LWIR cut-off wavelengths [7].

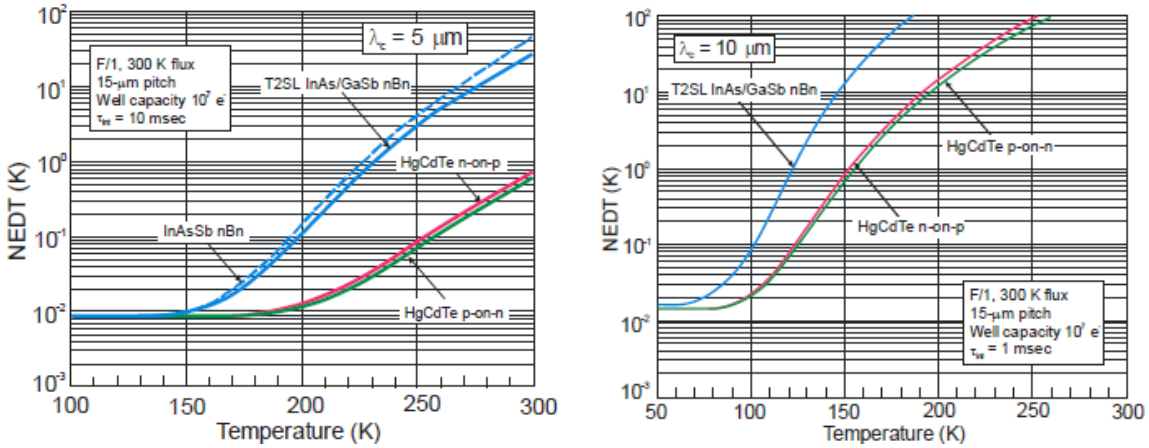

Figure 2.9: Noise Equivalent Temperature Difference (NETD) vs. temperature of the FPA for different barrier detectors with cut-off wavelength a)5 μm and b) 10 μm. It can be observed how T2SL barrier detector figures are worse comparing with HgCdTe barrier detectors. [7]

2.5.1.7.2 HgCdTe nBn barrier detectors

Even if HgCdTe photodiodes still the better in terms of low dark current, high sensitivity and high quantum efficiency, they continue in development with the aim of be further improved. As a result, the barrier technology has been also tested into HgCdTe detectors as it was done in T2SL detectors.

The main objective is to obtain HgCdTe nBn/pBp barrier detectors operating at temperatures much higher than 77 K, close to room temperatures. Nevertheless, the advances in HgCdTe are comparable behind T2SL barrier detectors. HgCdTe detectors present a valence band offset into its internal structure. That means that the valence

band and conduction band illustrated in Figure 2.6 are not perfectly aligned. This effect is limiting the performance of the nBn/pBp HgCdTe detectors. At 2017, new advances were achieved in the decrease of the valence band offset [56] [7].

Latest advances, show HgCdTe barrier detectors with figures of merit close to the HgCdTe photodiodes at lower temperatures [7]. It is, therefore, a technology to follow up but it will not be ready for a CubeSat mission in the near future since these detectors need to be first tested in the ground once developed.

2.5.1.7.3 InAsSb nBn/xBn barrier detectors

They are very promising detectors for the MWIR range. One of their main advantages is that they can be operated at higher temperatures, around 150 K or higher [7].

At the moment, InAsSb barrier detectors are manufactured by several companies. This is the case of the InAsSb xBn 'HOT Pelican-D' from SCD. It is a compact, 80 mm length and 300 g, detector for the 3.4 μm to 4.2 μm range. It is a low noise detector with a NEDT value in the order of 20 mK for a F number of 4 [5]. The variation of the NEDT with the temperature is illustrated in Figure 2.10.

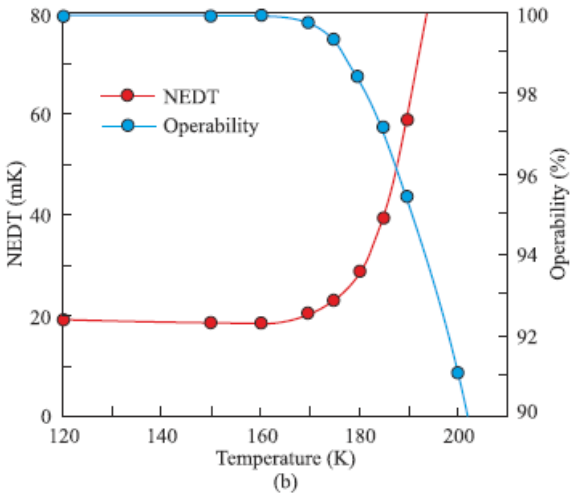

Figure 2.10: NETD vs. temperature of the detector for an InAsSb xBx 'Pelican D' photodetector from SCD. It has 640x512 pixels, 15μm pixel pitch and is sensitive for the 3.4 μm to 4.2 μm infrared range. Normal operation at 150 K. [5]

The 'Kinglet' detector, also an option for the OUFTI mission, from SCD, is within this group of InAsSb xBn barrier detectors. In addition to this, other InAsSb barriers

detectors can be found in manufacturers as IR Nova from Sweden, or the American Teledyne Nova Sensors [54] [50].

2.5.1.8 Photon trapping photodiodes

The next group of photodetectors is formed by the so-called photon trapping photodiodes. They are a new detection architecture to enhance the performance of the already developed infrared sensors. As it was the case of barrier detectors. The purpose is not only to reduce the noise but also to reduce the power consumption.

Photon trapping photodiodes appeared after 2010, as it was illustrated in Figure 2.2. At the moment, photon trapping detectors reduce the 1/f noise (Section 5.2.7) from the typical value of 1 kHz of HgCdTe detectors to a few hundred Hertz. In addition to this, it has been achieved a reduction in two orders of magnitude of the bias power needed to achieve the same value of responsivity in comparison with traditional HgCdTe photodiodes. The bias power is the power needed for the correct operation of the electronic components of the detector [6].

The photon trapping photodiodes still in development and they are not yet offered by manufacturers in contrast with the cutting-edge barrier detector largely produced.

2.5.1.9 New advances in nanomaterial detectors

Over the last few years, great advances in nanotechnology have been achieved. It is therefore clear that this technology will reach infrared detectors in the near future.

At the moment, is possible to find considerable advances in graphene-based photodetectors for the SWIR and MWIR. Also the so-called TMDC MoS_2 and WSe_2 photodetectors, which are highly sensitive detectors but with the disadvantage of slow response times, in the range of milliseconds to seconds. WSe_2 is used in the low-cost Colloidal quantum dot, QD photodetectors. The first QD detectors perform with very low dark currents, around 80 μA in the range from 3 μm to 5 μm. Nevertheless, the values of quantum efficiency still very low [45]. Additionally, as it was discussed also for HgCdTe barrier detectors, it is not a technology to be considered in the next CubeSat missions.

2.5.1.10 Infrared photodetector components

In general, the structure of photodetectors is similar for the different types of material. In Figure 2.7 it was illustrated a common photodetector. The main components are

the dewar, which contains the detector FPA, and the cooler engine connected to it. The size of these two elements joined is close to 100 mm or higher in traditional photodetectors. Nowadays, is possible to find photodetectors with the cooler included, no larger than 60 mm, as it could be the case of the 'Neutrino SWaP C Series' from the American FLIR [38]. This reduction in size is very advantageous for their use within the optical system of small size CubeSats. Inside the dewar, there are several different components as it is illustrated in Figure 2.11. These different components are going to be next described.

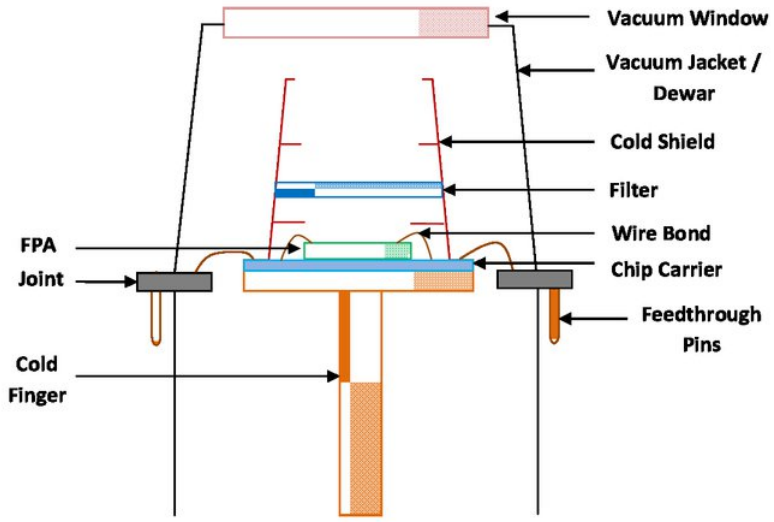

Figure 2.11: Scheme of the components that form a photodetector. [8]

- **Dewar:** it is a vacuum cover for all the detector components. Normally, it is made of Kovar, a nickel-cobalt ferrous alloy. This material is selected because of its good coefficient of thermal expansion. Within the dewar, it is also considered the housing and the base of the photodetector, made also of Kovar [9].

- **Vacuum window:** it is used to protect the FPA and to maintain the vacuum inside the dewar. It is fixed at the top of the dewar. This optical window has an excellent transmission in the wavelengths in which the detector operates, absorbing the undesired ones [58]. For infrared photodetectors, the material of the vacuum window is usually Ge, ZnSe, Si or Shaphire. The vacuum window is usually coated with an anti-reflection material [59].

- **Cold shield:** it is used to limit the field of view of the photodetector. This is done to isolate the FPA from unwanted out of field radiations reflected inside the dewar and is realised by a higher or lower aperture in the top of the cold shield. In addition to this, it is called cold shield since it is cooled down to the same temperature of the detector FPA in order to shield the detector. The cold shield is usually made of copper or silver [58] [9].

- **Optical filter:** the material of the FPA is sensitive for a range of wavelengths, nevertheless, it is possible to select a specific narrow wavelength by the use of a band-pass filter before the FPA. Filters are covered in detail in Chapter 3.

- **FPA:** the main detector component is located after the filter and in contact with the cold finger.

- **Cold finger:** it is directly connected to the cooler from one side and to the FPA of the detector and cold shield of the dewar from the other side. It is responsible for the temperature exchange between these three components [58] [8]. For its construction, it is commonly used the Inconel 625 material for the cylindrical part, and the alloy Al2O3 for the upper part in direct contact with the FPA [9].

- **Cooler:** it is usually a DC brushless motor, and is well known as Stirling micro cooler. It is important to highlight that is possible to find two types of coolers for infrared detectors. Integrated Dewar Cooled Assembly (IDCA) devices and Linear Engine devices. The first one, the IDCA setup, describes a system in which the cooler is directly in contact with the cold finger of the dewar. On the other hand, the linear engine is an external cooler connected to the dewar by a tube of small diameter. This allows to possibly locate the dewar and the cooler at different locations within the optical system. These devices have to be very stable, producing negligible vibrations and ideally with very low power consumption and higher durability. Nowadays, it is possible to find cryocoolers operating under very good performances, specially designed for space applications. This is the case of the cryogenic devices of the American manufacturer RICOR with his K series of coolers [60], and also of the micro coolers designed by the German AIM with a lifetime exceeding the 60000 hours [37].

A cutaway of a photodetector is represented in Figure 2.12, including some of the typical materials used for its construction.

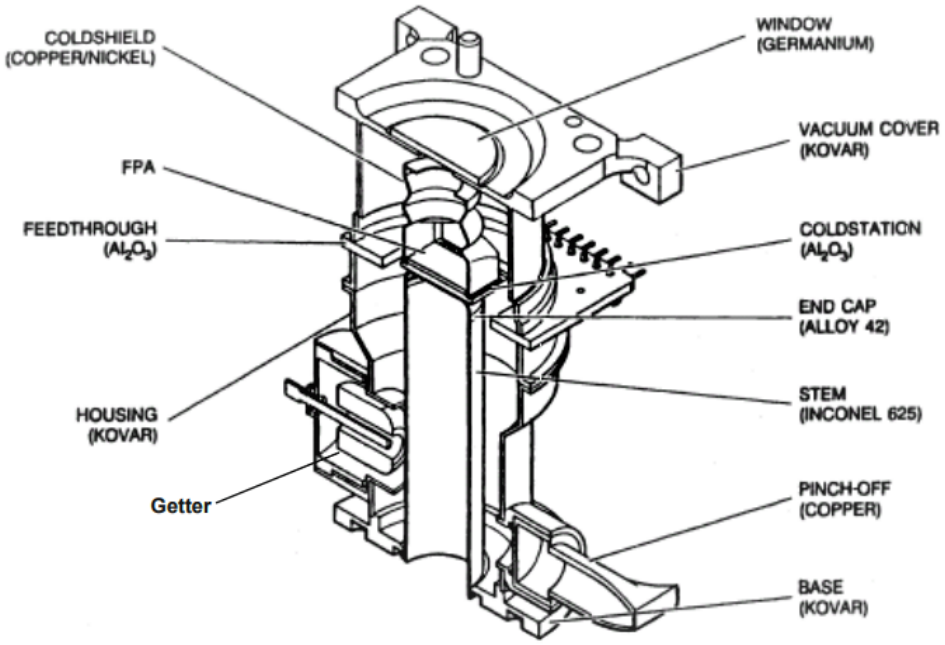

Figure 2.12: Cutway of a photodetector highlighting the main material used into its construction. [9]

2.5.2 Thermal detectors

The second large group of infrared detectors is composed by the thermal detectors. As discussed in the introduction of this chapter, the best property of thermal detectors is that, usually, they do not need to be cooled to operate. For instance, they are lighter and smaller than photodetectors. What makes them very suitable for a CubeSat. The lack of a mechanical cooler, as the IDCA rotary coolers of photodetectors, increases also the reliability of the detector.

Thermal detectors do not convert the incoming flux of photons into electrons, as in the case of photodetectors. In contrast, thermal detectors measure the variation in a specific physical property of the detector due to the heat of the incoming radiation [3]. The relation between the different types of thermal detectors and the physical variable that is measured appears in Table 2.5.2.

On the other hand, the biggest disadvantage of thermal detectors is their considerable big response time values (time to reach 63 % of the final output signal. Modern bolometers have response times in the order of 5 ms to 10 ms. This may suppose an important problem in space applications due to the requested short pixel exposure times coming from the satellite velocity. A solution could be to take the image before

Thermal detector	**Physical property**
Bolometer detector	Electrical resistance
Pyroelectric detectors	Electrical charge
Thermopile detectors	Tension
Dielectric detectors	Dielectric permittivity
Golay cell	Gas volume

Table 2.1: Physical property measured for each type of thermal detector.

reaching 99 % of the final output signal, approximately 3 times the response time, but the result will be a blurred frame. Nevertheless, within this project, there has been found one main solution, the time delay integration (TDI) that will be presented in Section 4.4.9.

In general, the performance and development of thermal detectors, in terms of sensitivity, signal-to-noise ratio and wavelength tunability, is considerably lower than photodetectors. It is important to considere that the first commercial bolometer detector appeared at the beginning of the 1990s, 40 years later than the first HgCdTe photodetectors, therefore there was a big gap in the technology [44]. In spite of this, nowadays the interest in thermal detectors has soared as it has been reported by the companies providing software for the development of infrared detectors.

One of the reasons for their recent success is due to the introduction of the new micromachined silicon bolometers (MEMS) which are compatible with the cutting edge CMOS read-out circuits. The CMOS technology allows to drastically reduce the response time. These MEMS detectors will be the best option for a space mission as it will be later presented.

Besides microbolometers, there are several other categories of thermal detectors. Nevertheless, there will be discussed only the groups with applicability in a space mission. Excluding for example well known thermal detectors as the Golay cell due to its internal structure not compatible with the harsh conditions of the space environment [6].

2.5.2.1 Bolometers

It was discussed how an incident flux of photons changes the temperature of the detector FPA, which causes a variation in the detector electrical resistance for the case of the bolometers according to Table 2.5.2. Therefore, this type of thermal detectors is constructed in a way in which the absorbed radiation (low in the infrared)

produces a large change in the electrical resistance with the purpose of increasing its sensitivity. To achieve this, the bolometer is constructed from a material with a very small thermal capacity and large temperature coefficient [6]. The thermal capacity is defined as the amount of energy that must be absorbed by an object in order to change its temperature. On the other hand, higher temperature coefficients produce larger changes in electrical resistance. A schematic representation of a bolometer pixel is included in Figure 2.13.

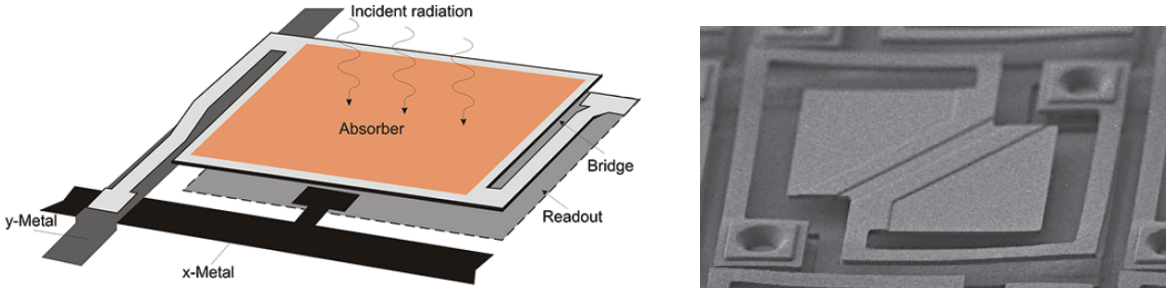

Figure 2.13: a)Representation of the pixel internal structure for a bolometer. [2] b) Photography of a bolometer pixel. [10]

At the moment, several types of bolometers have been developed. They will be discussed in the following section, excluding the detectors that are out of the wavelength range of the CubeSat mission (MWIR-LWIR). As it could be the case for example of the well-known hot electron bolometers (HEB) with high speed of response but operating close to terahertz wavelengths [6].

2.5.2.1.1 Metal bolometers

They are within the first generation of bolometers. Metals were later substituted by semiconductors and superconductors. At room temperatures they have a specific detectivity, D^*, of the order of $1 \cdot 10^8$ cmHz$^{1/2}$W^{-1}, as a reference, InSb photoconductors for the MWIR at room temperatures reached higher detectivity values than metal bolometers, of the order of $2.5 \cdot 10^8$ cmHz$^{1/2}$W^{-1}, [6].

The metals used for their fabrication are nickel, platinum, or antimony. But they are fragile and thus the size of the arrays is limited. Metal bolometers are used only in applications that require long-term and high stability [2].

2.5.2.1.2 Thermistor bolometers

Thermistor bolometers are well known for their use in several applications in the ground, like alarms or fire detection systems. But also, they have been implemented in several Earth satellite missions, for the satellite attitude control. Thermistor bolometers detect the sharp discontinuity of temperatures between the Earth limb and the space horizon, what is later used into the orientation of the spacecraft. Nevertheless, their noise levels, especially the 1/f noise, are very high to be used in imaging arrays [2].

2.5.2.1.3 Semiconductor bolometers

In comparison with other thermal detectors, semiconductor bolometers operate at low temperatures, less than 100 K, in order to reach the highest possible performances. Despite this, semiconductor bolometers offer and extraordinary detection capability of low fluxes. As a result, semiconductor bolometers have become a detector of reference for the LWIR and very long waveband infrared, VLIR, [2].

The most advanced semiconductor bolometers are based on gallium and germanium, for the wavelength range 5 μm to 100 μm. The performance can be comparable with the photodetectors operating at the same range, as extrinsic photodetectors, T2SL detectors and FLIR HgCdTe detectors, discussed in previous sections. Latest developments have substituted the germanium of the semiconductor bolometer for silicon in order to have a lower value of noise [6].

2.5.2.1.4 High-temperature superconducting bolometers (HTSC)

The response time is one of the main fundamental figures of thermal detectors. Superconductor detectors are faster than semiconductor detectors maintaining similar sensitive values. HTSC detectors are mainly fabricated in YBaCuO. As it was done in semiconductors, they are also cooled to cryogenic temperatures, around 77 K, reference [3].

Their high sensitive in the LWIR and its reduced response time in comparison with semiconductor bolometers, make them a real competitor to the best cooled detectors

for wavelengths higher than 10 μm. At Figure 2.14, it is plotted the value of specific detectivity, D^*, for different photodetectors and the superconducting bolometers, operating all of them at 77K. Is possible to observe similar values of sensitivities of semiconductors and HgCdTe cooled detectors at wavelengths around 10 μm, while for wavelengths higher than 20 μm the sensitivity is large for semiconductor bolometers [6].

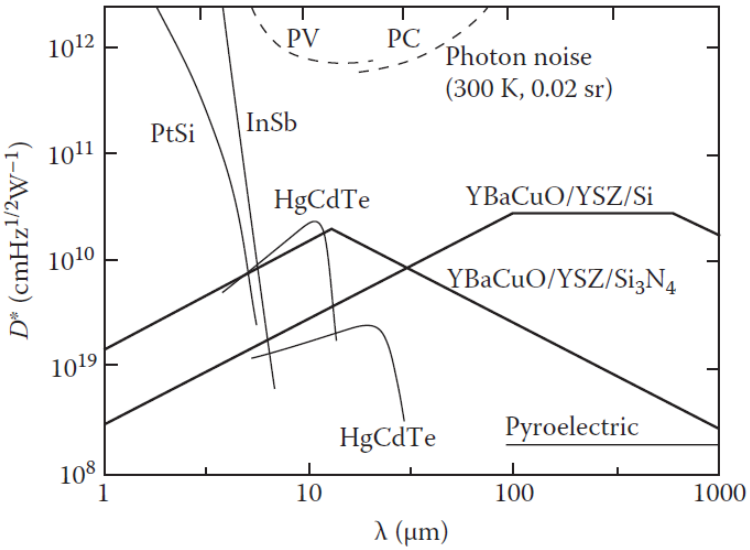

Figure 2.14: Specific detectivity vs. wavelength for different detectors, illustrating how at large wavelengths, cooled High Temperature Superconducting Bolometers have a bigger sensitivity values than HgCdTe photodetectors also at 77K. [6]

Recently, HTSC superconducting bolometers have reached great importance in the development of microbolometer detectors, presented in the next section.

2.5.2.1.5 Microbolometers. Micromachined room temperature bolometers (MEMS). Amorphous silicon (a-Si) and vanadium oxide (VO_x)

During the last decades, many efforts have been made into the miniaturization of components. Microbolometers arrays are formed of several tiny heat-sensitive sensors fabricated using microelectromechanical systems (MEMS) technology. The impact of the photon flux on these small sensors will heat them what will later produce a change into the electrical resistance, as explained in the bolometers introduction.

The most common type of commercial microbolometers are the thermistor bolometers. In addition to this, large advances have been achieved into the development of

semiconductor and superconductor bolometers [6], characterized by their great performance at long wavelengths as discussed before.

Mainly two materials are used in the production of microbolometers, vanadium oxide (VO_x) and amorphous silicon (a-Si). The former, VO_x, is the most common material offered by manufacturers. The a-Si microbolometers are less common but they are also available at the market. This is the case for example of the cutting-edge a-Si microbolometer 'Pico1024 Gen2' for the 8 μm to 14 μm range, and with a size of 1024x768 pixels, from the French manufacturer ULIS [11]. The main disadvantage of a-Si bolometers comparing with VO_x detectors is that a-Si bolometers have a higher Johnson noise. The Johnson noise depends on the temperature of the detector, the value of the bolometer resistor, and also is dependent on the circuit bandwidth. Therefore it will be necessary to cool-down the a-Si bolometers in order to reach the same value of Johnson noise present in VO_x detectors. The a-Si material has the advantage of be easily implemented with a CMOS read-out circuit in comparison with the VO_x material [61].

Although microbolometers are fundamentally for the LWIR range from 8 μm to 14 μm, new detectors have appeared extending its range to the MWIR, from 3 μm to 14 μm. These last microbolometers are known as wide band (WB) microbolometers. In general, microbolometers have a high pass filter to limit its range to the LWIR, if it is not, it will be not possible to observe in the LWIR high-intensity events on the ground because the detector will be 'blind' by a higher signal in the MWIR. Microbolometers without the high-pass filter (WB microbolometers), can be used for example to observe a fire. An example is the FUEGO mission, a constellation of small satellites including a microbolometer for the fire monitoring in the MWIR at an altitude of 700 Km, [35]. WB detector cannot distinguish between the signals coming from the MWIR or the LWIR. The concept of a dual-band MWIR-LWIR microbolometer is presented at Chapter 2 and 7.

As an example, SCD produces the 'BIRD 640' VO_x wide-band microbolometer. The main issue of this detector is the long time constants, the great disadvantage of thermal detectors. For this detector, the thermal time constant (also known as response time, time to reach 63 % of the final output signal) is in the order of 14 ms, [5]. One of the objectives will be to passively reduce the temperature of the detector to see the effect in the time constant and therefore increase their usability in space missions.

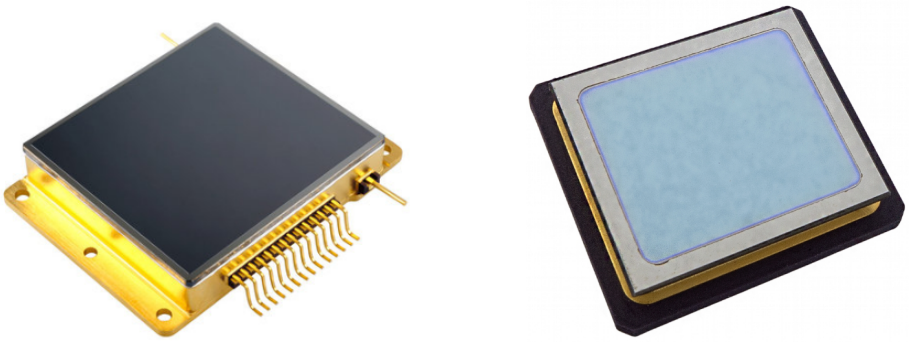

Figure 2.15: a) Microbolometer 'Pico 1024' from the French manufacturer ULIS. It has 1024x768 pixels, 17μm pixel pitch, operating in the 8 μm to 14 μm infrared range at room temperature with a NETD of 50mK in ground.[11] b) Microbolometer 'Bird 640 Ceramic Packaging' from the Israeli manufacturer SCD. It is a wide-band detector from 8 μm to 14 μm, with a FPA of 640x480 pixels and 17μm pixel pitch. The NETD is 22 mK with a response time of 18 ms. Both detectors do not requiere a termo electrical cooler (TEC) [5].

One of the first space missions that implemented microbolometers was the 2001 Mars Odyssey mission into its Thermal Emission Imaging System (THEMIS) instrument working in the LWIR range. A microbolometer for the LWIR was also used in the New Infrared Sensor Technology (NIRS) instrument of the Aquarius SAC-D Canadian mission for the monitoring of forest fires and water temperatures. These detectors were adapted to withstand the space environment [33].

Recently, in 2017, a microbolometer for the 7.5 μm to 15.5 μm region, has been used in the CubeSat ISARA developed by NASA/JPL for weather monitoring [62]. The camera used was the 'Tau 2' from the American manufacturer FLIR. The Tau 2 camera is going to be also used in the Phoenix CubeSat of the Arizona State University in the US.

2.5.2.2 Pyroelectric detectors

The pyroelectricity is the property of certain materials to generate a temporary current when they are heated. This effect is used in the design of pyroelectric detectors, where the current generated depends on the heat produced by the incident flux of photons. This current or electrical charge change allows to quantize the incoming infrared radiation and therefore form later image.

It is not a useful detector for space applications since it needs to be operated in stable environments. Besides this, it requires an optical chopper to defocus the

incoming light and operate correctly, which produces elongated images when used in moving cameras as it will be the case of a satellite [6].

2.5.2.3 Thermopiles

Thermopiles appeared looking for low cost and low power thermal detectors. These two properties characterize thermopiles, and because of that, in several application bolometers and pyroelectric detectors have been substituted by thermopiles even if they do not reach yet their sensitivity. For thermopiles, the physical property measured is the electromotive force or tension generated in the internal junctions of the detector by the heat produced by the incoming radiation.

In 2005, an array of linear thermopiles detectors was used in space in the Mars Climate Sounder (MCS) instrument of the Mars Reconnaissance Orbiter (MRO) for the observation of the Mars surface in the range from 12 μm to 50 μm, [33].

In 2017, great advances were done in their implementation with CMOS read-out circuits. Furthermore, another advantage is that they do not use the optical chopper characteristic of pyroelectric detectors [3]. It is, therefore, a technology to closely follow for future implementation in a CubeSat working in the LWIR.

2.5.2.4 Temperature control of thermal detectors

Thermal detectors, with the exception of thermopiles, are sensitive to ambient temperature variations. This may affect the precision in the measurements of the detector. In order to solve this problem, thermal detectors commonly include a thermoelectric cooler (TEC) to stabilize the detector temperature at a fixed level. Therefore, it will respond only to temperature changes in the target. The problem of these devices is that they increase the power consumption of the optical system besides the cost of the instrument [63]. State of the art-microbolometers, do not need for thermoelectric coolers due to the use of novelties read-out techniques for the microbolometer change in resistance. This is the case of the presented wide-band BIRD 640' microbolometer from SCD that does not make use of a TEC.

2.6 Second comparison of photodetectors and thermal detectors

The ideal infrared detector, would respond instantaneously when illuminated by an incoming flux of infrared radiation; would have an excellent responsivity in the wavelength range of operation and negligible out of it; would work at high performance even when the temperature of operation changes, with low cooling requisites; and finally, the power consumption and cost would be also low [46]. Nevertheless, it has been seen that the ideal detector does not exist yet. For example, thermal detectors have a low cost and power consumption and can also work at higher temperatures without using a cooler. Despite this, their sensitivity, responsivity and noise figures are in general lower than photodetectors for the same wavelength range of operation. Therefore, the final selection of the infrared detector will be based on the requisites of the mission.

The next paragraphs will summarize the best properties of the discussed photodetector and thermal detector for the infrared. Starting with the short wave infrared SWIR range, until 1.7 μm, where the best performances are offered by InGaAs photodiodes, with quantum efficiencies higher than 80 % and sensitivity values larger than HgCdTe photodiodes.

Operating in the MWIR, there are architectures and materials like InSb, HgCdTe, Type II superlattice, QWIP and QDIP detectors besides the wide-band microbolometers. In general, the best performances in terms of detectivity and noise generated is obtained with HgCdTe photodiodes. The availability of HgCdTe detectors in the market is very large and is possible to easily find a detector that adapts to the requirements of the mission. Nevertheless, their high cost in comparison with other MWIR detectors as InSb, and low operating temperatures (best performance at 77 K) can be a limitation for specific missions. InSb detectors are also a very good option to take into account due to its flight heritage, In contrast, the major drawback of InSb photodetectors is the cooling requisites, operating at a maximum of 80 K.

In the last decade, new technologies appeared with the aim of improving HgCdTe detectors. This is the case of the QWIP, QDIP and T2SL detectors. Among them, QDIP and T2SL are the most promising ones. New QDIP detectors have proven higher performances at large temperatures, in the order of 200 K, in comparison with HgCdTe photodiodes at the same temperature. The drawback of QDIP detectors is its lack of

availability in the market and therefore they are not an option for the near future. On the other hand, T2SL detectors are also projected to overpass HgCdTe photodiodes. New T2SL with barrier nBn/pBn architectures improve even more the capabilities of T2SL photodiodes, but at the moment, their dark current and sensitivity values still behind HgCdTe photodiodes. Nevertheless is possible to find excellent T2SL barrier detectors in the market. Highlighting the Neutrino SWaP+C from the American FLIR operating at 130 K, and the T2SL detectors offered by the German manufacturer AIM or the Israeli SCD.

In addition to this, there are also the wide band microbolometers, 3 μm to 14 μm, operating at room temperature but the disadvantage of the long-time constants. In the following chapters, it will be test their use in space missions.

Finally, for the LWIR range, there is a higher offer in infrared detectors. In this range, there are already infrared detectors overpassing HgCdTe photodiodes capabilities. For example, extrinsic photodetectors highlight due to their sensitivity to low-background fluxes, which is a very attractive feature for a space mission. Nevertheless, its operating temperature is extremely low in the order of 10 K. Type II superlattices were worst in the MWIR, but in the LWIR their specific detectivity values are greater than HgCdTe photodiodes. An example of an LWIR T2SL detector is the PELICAN D from SCD.

Thermal detectors have a great performance in the LWIR range. This is the case of the high-temperature superconducting bolometers (HTSC). At room temperature, their sensitivity is larger than HgCdTe detectors as it can be supposed. But if they are cooled to 77 K, at 10 μm wavelength the detectivity values are similar to the ones of HgCdTe photodiodes at 77K and larger after 20 μm. On the other hand, HTSC thermal detectors share the drawback of QDIP detectors which is their low availability at the moment.

Referring to the microbolometers, the greatest availability is for the LWIR. They have been already designed for space missions, highlighting the MISTIGRI satellite with a multispectral capability in the LWIR. This mission achieved the required NETD lower than 0.5 K for the monitoring of ground and agricultural areas [23]. As mentioned before, the microbolometers usability will be presented with large detail in the following section.

As a reference for the temperature of operation and specific detectivities for the different infrared detectors, Figures 2.16 and 2.17 are next included. The specific

detectivity, D*, allows to directly compare the performance of the sensors since it is defined per unit of detector area and unit of frequency in which the detector operates.

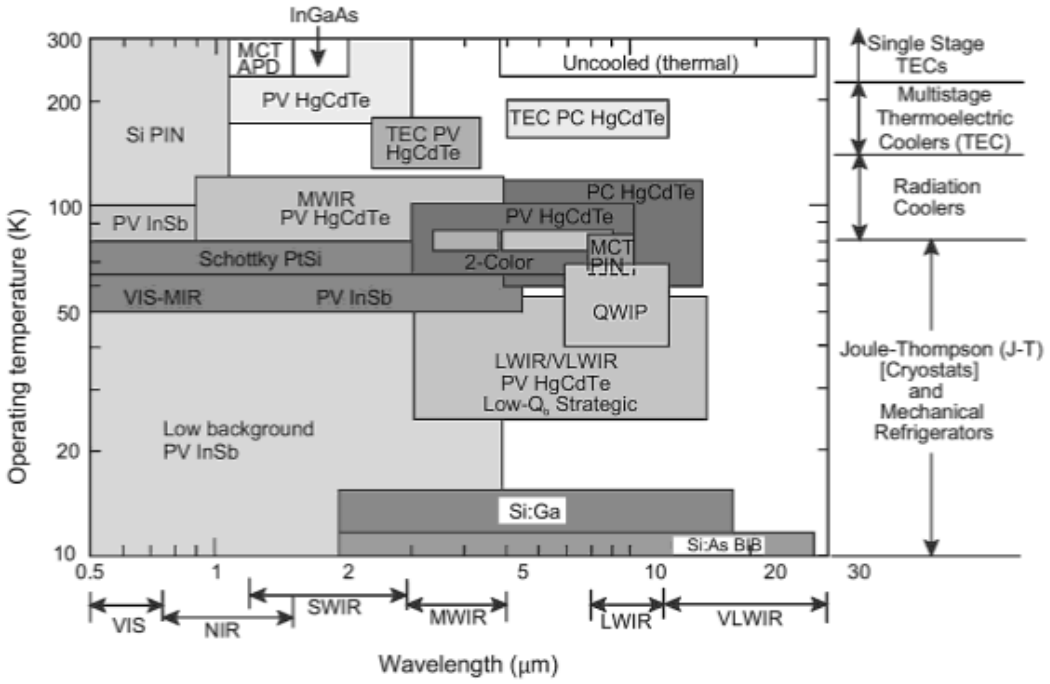

Figure 2.16: Operating temperatures for the main groups of photodetectors and thermal detectors. [3]

2.7 Conclusions

This chapter is a collection of all the infrared single band technologies. Once presented the figures of merit of infrared detectors, it was possible to compare the different sensors in the previous 'second comparison of photodetectors and thermal detectors'. On the MWIR range, it is clear that photodetectors are the main reference. Nevertheless, for the LWIR, thermal detectors play a very important role. The cost of thermal detectors and their size is comparatively smaller than photodetectors. In addition to this, these are two very attractive properties for CubeSat technologies.

A numerical comparison of the best single band photodetectors and thermal detectors at the market is presented in Chapter 6. On it, it is compared not only the performance of the detectors on the ground but also in the space environment.

On the other hand, there are also the very promising QDIP detectors, HgCdTe nBn/pBn barrier detectors and High-Temperature Superconducting Bolometers. However, they are not yet available to buy and therefore they can not be considered for

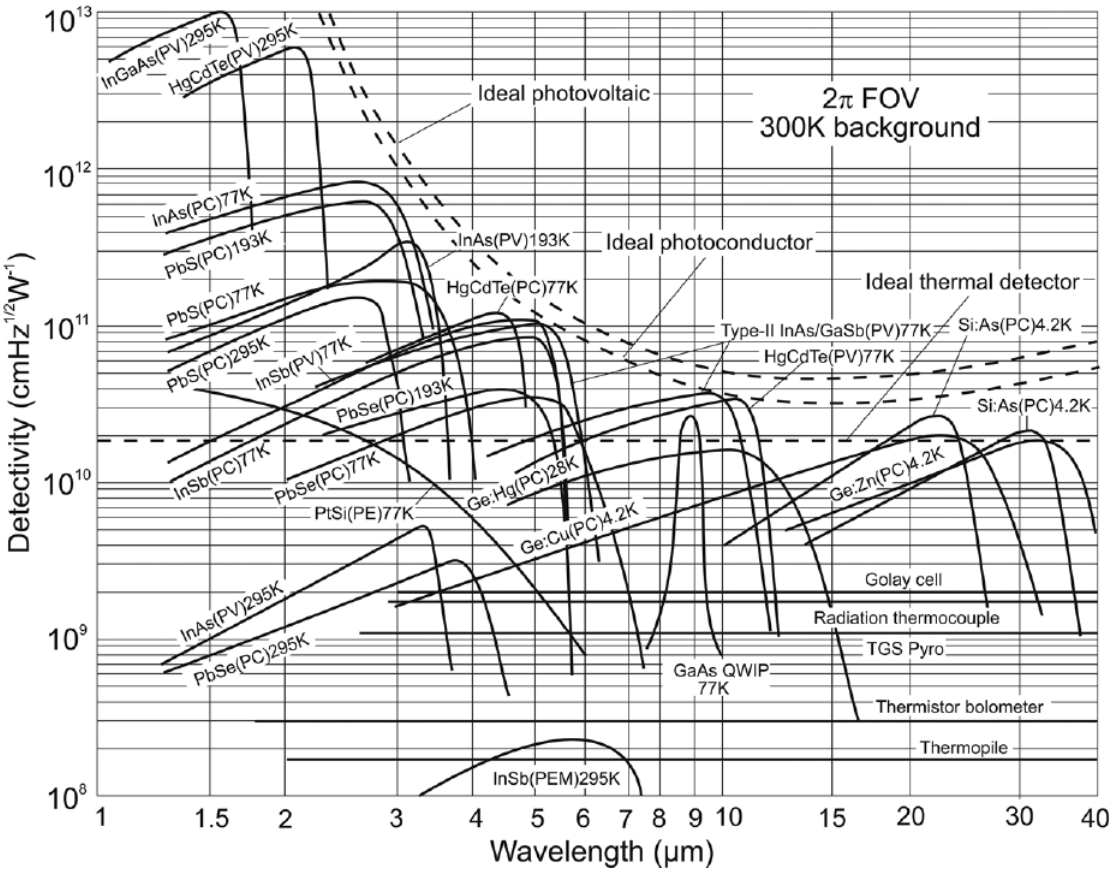

Figure 2.17: Specific detectivity vs. wavelength for the main groups of infrared photodetectors and thermal detectors. [6].

a near CubeSat mission. In the next chapter, there will be presented the dual-band infrared detectors.

Chapter 3

Multiband operation

3.1 Introduction to multiband detectors

In the previous chapter, there were presented several detectors sensitive to a wide range of wavelengths in the infrared electromagnetic spectrum. Nevertheless, these detectors were used only for a specific band inside this range. For example, there were MWIR HgCdTe photodiodes and LWIR HgCdTe photodiodes.

New emerging infrared detectors have multicolour capabilities. That is, a detector capturing light in a wide range of wavelengths and then be able to discriminate the radiation of a specific band in the interval captured. With a multicolour or multi-band detector, it will be possible to have considerable more information of the target observed.

Different multi-band infrared detectors are already offered by the manufacturers. These detectors will be analysed in this chapter, comparing the different dual-band materials.

3.1.1 Types of multiband detectors

3.1.1.1 Dual-band HgCdTe FPAs. HgCdTe triple layer heterojunction (TLHJ) design

The first infrared multiband detectors, presented at the beginning of the 1990s, were the dual-band HgCdTe detectors. They are made by a combination of two photodiodes p-n junctions, as the ones discussed for single band detection detectors. This structure is known as n-P-n HgCdTe triple layer heterojunction design (TLHJ). The term heterojunction refers to the interface between two layers of semiconductors with a different energy gap (space between the conduction band and balance band, Figure

2.6). Therefore, one of the photodiodes has a longer wavelength of operation than the other [12]. A descriptive drawing of one pixel is presented in Figure 3.1.

In addition to this, at Figure 3.2 is possible to see that the response of the longwave photodiode is maximum when the response of the shortwave photodiode is minimum. This effect is because the cut-off wavelength of the shorter photodiode acts as a band-pass filter for the long wavelength photodiode.

These detectors can be fabricated with two different architectures. Therefore, it is possible to find sequential-mode detectors and simultaneous-mode detectors. The former, the sequential-mode, is less efficient since it is not possible to independently control the voltage necessary for the operation of each photodiode. That gives rise to the crosstalk effects, which are undesired effects in one photodiode coming from the other photodiode. On the other hand, the simultaneous-mode dual-band detectors, Figure 3.1, incorporate an additional electrical contact what allows to independently control the two photodiodes. In addition to this, later, the two channels are also integrated in the read-out circuits simultaneously [12] [3].

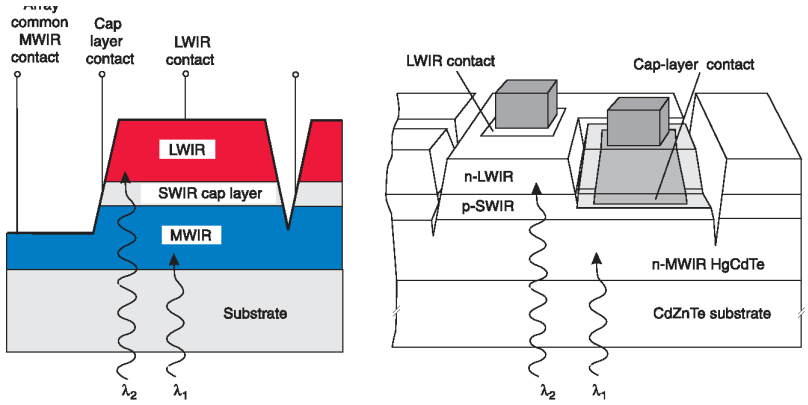

Figure 3.1: Pixel structure of a HgCdTe dual-band MWIR and LWIR focal plane array. [12]

The performance of the dual-band HgCdTe detectors is similar to the single HgCdTe photodiodes, in terms of sensitivity, quantum efficiency and low noise. Sharing also disadvantages like the high cost of production [64].

Several manufacturers like the American Raytheon, the French Sofradir or the UK/Italy Leonardo offer in their catalogues dual band HgCdTe detectors. But among them stands one detector offered by Leonardo. The 'Condor II Dual Waveband Infrared Detector' [32]. The main characteristics are described in Table 3.1. The Leonardo Condor II is an astounding detector for dual-band MWIR-LWIR infrared,

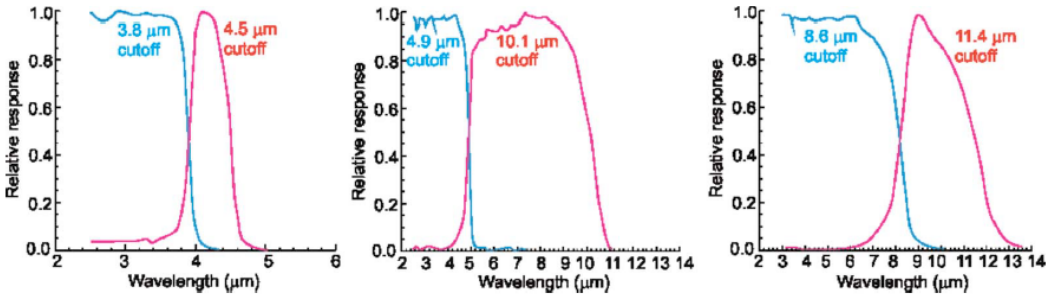

Figure 3.2: Differences in the response of the two photodiodes that form a HgCdTe dual-band detector. [12]

operating at high quantum efficiency and with the characteristic low values of noise in photodetectors. In addition to this, after recent communications between the Centre Spatial de Liège, CSL, and Leonardo, it has been possible to know that the 10 μm cut-off in the LWIR can be extended to 14 μm under request by growing additional wafers (semiconductor slices). One of the disadvantages could be the size, what could limit its use in very small CubeSats. Another issue could be the rotary Stirling cooler, which can be affected by vibrations in the harsh space environment.

Parameter	**Value**
Wavelength range	Dedicated 3 μm to 5 μm
	Dedicated 8 μm to 10 μm
	Dual band mode: 3 μm to 5 μm and 8 μm to 10 μm
FPA size	640x512 pixels
Pixel pitch	24 μm
Quantum efficiency	70 %
Operational temperature	80 K
NEDT	MWIR dedicated: 11 mK
	LWIR Dedicated: 22 mK
	Dual band mode: MWIR 28 mK, LWIR 28 mK
Dimensions	145x80x70 mm (Cooler included)
	750 g (Cooler included)
Cooler	IDCA, Rotary Stirling engine

Table 3.1: Fundamental parameters of the 'Condor II' dual-band infrared HgCdTe detector from the UK/Italy manufacturer Leonardo. [32]

Therefore, dual-band HgCdTe photodiode detectors are a very good option to take into account for the multiband OUFTI CubeSat. Other solutions will be presented in the multi-band filter section.

3.1.1.2 Dualband QWIP FPAs

Multiband detection is also a possibility for quantum well detectors. They are made following the same concept as HgCdTe dual-band detectors, by joining two different QWIP layers [44]. A QWIP was formed in semiconductors by introducing a narrow gap material between two layers of wide gap material. In addition to this, in order to have an independent bias control of the two QWIPs, as the simultaneous mode discussed before, a contact layer is introduced between the two QWIPs. An illustration of the internal architecture of an MWIR-LWIR QWIP is presented in Figure 3.3.

The operating temperature of these detectors is in the order to 40 K to 100 K. Multicolor QWIPs share the advantages but also the disadvantages of QWIP single unit detectors as for example the low quantum efficiencies or higher dark currents in comparison with HgCdTe [64] [12].

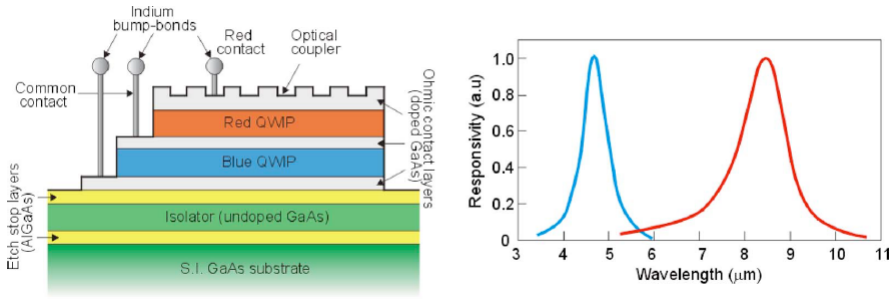

Figure 3.3: QWIP dual-band detector a) Pixel structure, b) wavelength responsivity. [12]

Advanced dual-band QWIPs detectors are developed by NASA/JPL and QimagiQ. It was already mentioned a NASA mission for 2023 in which a QWIP multicolour detector is going to be used. The Hyperspectral Infrared Imager (HyspIRI) mission, detecting in the range of 7.5 μm to 12 μm with a dual-band QWIP [33]. On the other hand, QimagiQ commercializes a multicolour QWIP detector formed by a GaAs/AlGaAs QWIP layer on top of an InGaAs/ GaAs/AlGaAs QWIP, with respectively cut-off wavelengths of 8.6 μm and 4.6 μmm [65]. The value of NETD (the parameter used to describe the temperature resolution, Chapter 5) is lower than 35 mK in accordance with typical photodetectors.

3.1.1.3 Multiband QDIPs and DWELL FPAs

Single band quantum dot-infrared photodetectors, QDIPs, were presented as a very promising technology. These conventional QDIP detectors overpassed the properties of the QWIP detectors as the quantum efficiency, in the order of 35%, besides lower values of dark current. Furthermore, they had better detectivity values at high temperatures, 200 K than HgCdTe photodiodes. On the other hand, the concept of DWELL detectors was associated with a combination of QDIP and QWIP detectors [12].

The first advances in this dual-band technology were presented as a voltage-tunable dual-colour DWELL detector. A 320x256 MWIR/LWIR FPA that modifies its response to a different wavelength range depending on the voltage applied with values of NETD from 55mK in the MWIR to 70mK in the LWIR [12]. Nevertheless, this technology still in development and has not yet tested in space as it was the case of dual-band QWIPs, therefore it is also not considered for a near future CubeSat mission.

3.1.1.4 Superlattice type-II Dual-band FPAs

Type II superlattice detectors highlighted due to their great performance in the LWIR range in comparison with HgCdTe detectors. Several manufacturers produced these detectors mainly for the LWIR, but also for the MWIR 3.5 μm to 5.0 μm range, like IRNova in Swedenm [54].

Nowadays, T2SL dual-band detectors have reached a great level of development. One of their advantages is that the thickness of the pixel structure in multiband is in the order of 5 μm in comparison with the 15 μm of HgCdTe multiband detector (two photodiodes joined). Therefore their transit time, time that the photons need to cross the pixel active area thickness, is lower what is better for high operating temperatures [7] [64].

One of the manufacturers that offer a dual-band detector, is AIM from Germany. It is a T2SL tunable dual-band detector in the MWIR, 3.4 μm - x - y - 5 μm wavelength of operation. The size is 384x288 pixels and 40 μm pixel pitch operating at 80 K, [37]. The performance in terms of detectivity and noise levels of the AIM detector is lower than the dual band 'Condor II' HgCdTe detector from Leonardo, but the AIM detector is dual-band in the MWIR while the detector from Leonardo was dual-band MWIR/LWIR. Moreover, AIM works into space applications and has already developed two low vibration and high duration coolers to be used in infrared detectors

for space missions. Therefore T2SL dual-band detectors are also considered for a future multiband CubeSat mission.

3.1.1.5 Microelectromechanical systems (MEMS). Four generation FPAs

The future of infrared sensors will be oriented into adaptive FPAs for multispectral imaging. The so-called Adaptive FPA (AFPA). The purpose is to achieve a voltage tunable detector in which the sensitivity of each pixel can be independently modified for a specific wavelength, eliminating the necessity of using additional optical elements as filters or dispersive lenses [12]. A description of this technology is included in Figure 3.4. As a remark, this sensor can be referred also as Transverse Field Detector (TFD).

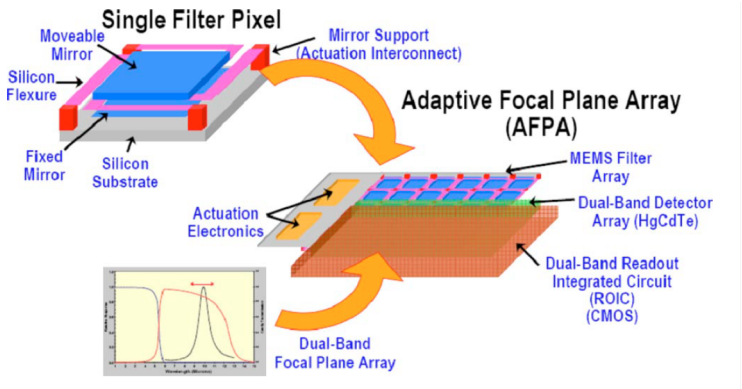

Figure 3.4: Dual-band adaptative FPA. Four generation of infrared detectors. [12]

3.1.2 Dual-band microbolometers

The manufacturer SCD from Israel is producing the Bird 640 Ceramic Packing BB wide band detector. This detector operates in the range from 3 μm to 14 μm, [5]. Thermal detectors microbolometers can not discriminate between the radiation coming from the different wavelengths. The responsivity is constant for all the band in contrast with photodetectors where there was the concept of cut-off wavelength. However, the detector produced by SCD has a very big potential, for applications in which the ground temperature is very high. For example a fire. The use of this detector in the MWIR range will be detailed analysed in Chapter 7 with the temperature resolution model developed in this project.

3.2 Devices to split the light into its wavelengths

3.2.1 Introduction

Multiband infrared detectors are a very promising technology. However, they still in development and therefore there is not a large variety of multicolour detectors at the moment. As a result, their use can be limited to some applications.

In this section, there will be presented the different methods that can be used to split the light into its different wavelengths. On one hand, there are the traditional prism and grating devices, while on the other hand there are the new multispectral arrays of band-pass filters. These devices can be used not only for multiband operation but also for multispectral and eventually hyperspectral operation. Multispectral refers to the capability of splitting the light into several channels (wavelengths) inside each of the wide bands. The difference between multispectral and hyperspectral is the number of channels in which the light is divided. In addition to this, several examples of space missions are also introduced for the different methods to split the light.

3.2.2 Optical filters and multispectral imaging systems

A filter is a passive optical device used to control the flux of photons that is reaching the detector. In general, two types of optical filters can be distinguished. These are the band-pass filters, also known as absorptive filters, and the dichroic filters.

A band-pass filter (BFP) or absorptive filter, is a device that isolates certain wavelengths of the incoming radiation and rejects the others. This is dependent on the absorption properties of the glass substrate used for the filter. Moreover, usually, these filters maintain its properties of transmission and absorption for a wide range of angles of the incoming radiation. Depending on the band of the electromagnetic radiation that they allow to pass, the concepts of wide band-pass filters and narrow band-pass filters are used [66].

On the other hand, dichroic band-pass filters use the principle of thin-film interference to transmit the light of a specific wavelength of interest and block the others. The filter can be considered as a film between two mediums were the film and the medium index of refraction are different. The light waves reflecting from the upper surface of the film will interfere with the waves reflecting from the bottom surface. Depending on the type of interference (from the different dichroic filters), the light

reflection will be higher or lower, an effect that is used to select the specific desired wavelengths [67] [16].

In order to achieve multispectral and hyperspectral capabilities, it is needed a combination of different filters.

In general, the optical instrument of a satellite can capture the incoming light through two different methods. Scanning and snapshot. The scanning technology use movable devices. In addition to this, to reach the multispectral capability with a scanning device is necessary to expose the pixels of the detector multiple times. In contrast, the snapshot technique allows capturing a multispectral image with only one exposure of the pixels. Moreover, for the snapshot technique, is not necessary to use movable parts. Other difference is that a scanning device starts capturing the objective scene from the border of it, while for the snapshot technique you need to be at the centre of the scene you want to capture. On the other hand, the complexity of designing a snapshot device is higher than for a scanning system, they need for bigger FPAs, advanced manufacturing methods and highly precise optics [16].

In Figure 3.5 there are illustrated different multispectral imaging systems, MSI, depending on the combination of band-pass filters for multispectral imaging and the technique for capturing the scene. They are going to be next explained.

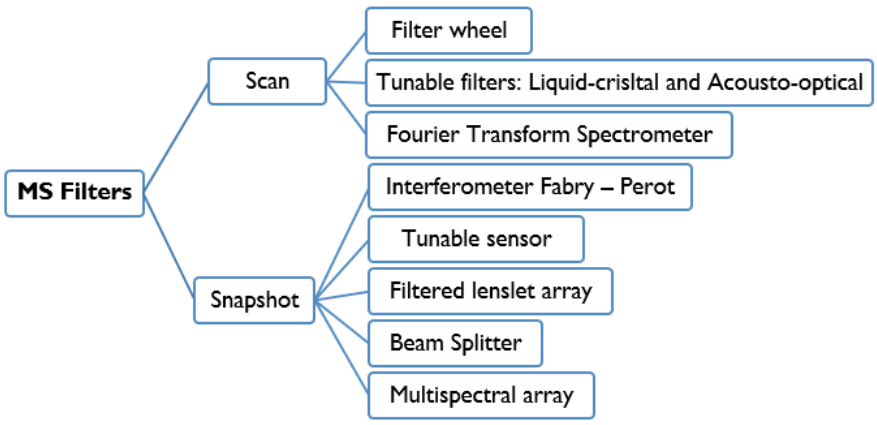

Figure 3.5: Different multispectral techniques for scanning and snapshot devices.

3.2.2.1 Scanning imaging techniques

3.2.2.1.1 Filter wheel

It is a device made of different band-pass filters not superimposed. Each of the filters

insolates a specific wavelength and reflect or attenuate the others. A filter wheel usually rotates capturing an image of one spectral band per exposure time. Therefore, after several exposures is possible to do a reconstruction of a multispectral image.

A very good example is the filter wheel used by the NASA CubeSat Mars Micro Orbiter, MMO. This 12U CubeSat contains three cameras, one camera for the visible wavelengths and other two cameras for the observation in the longwave infrared. Each of the LWIR cameras used an uncooled microbolometer of 17 μm pixel pitch and 640x480 pixels FPA. These two LWIR cameras shared an eight-position filter wheel, and each camera uses three of these filters, and the other two filters were used for calibration of the instrument. One of the cameras operates in the range 7.5 μm to 13 μm with a subdivision of 3 bands and the other camera in the 14 μm to 16.5 μm range also subdivided into 3 bands [68] [13]. A picture of the CubeSat and instrument is included in Figure 3.6 [13].

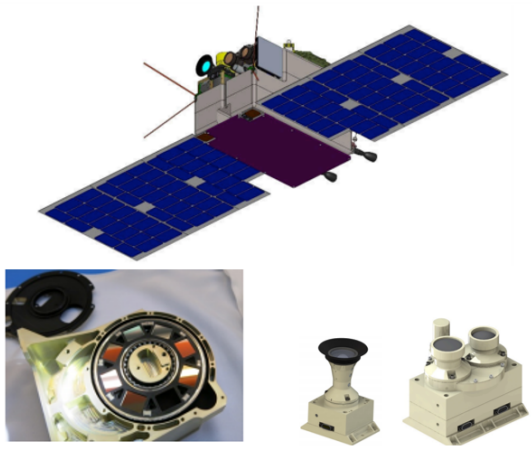

Figure 3.6: Filter wheel included in the Mars Micro Orbiter (MMO) CubeSat for multiband operation in the LWIR range. [13]

3.2.2.1.2 Tunable filters

It is a band-pass filter that changes its properties depending on the applied voltage. The most used tunable filters are:

- Liquid crystal tunable filters: these devices use a liquid crystal to select and specific wavelength in function of the electrical current flowing through it. A liquid crystal is a substance that can flow like a liquid while its molecules can be structured as a crystal [14].

- Acousto-optical tunable filters: they are birefringent crystals that vary in their response in function of an applied acoustic field. Therefore, with different sound waves is possible to split the light in its different wavelengths [16].

3.2.2.1.3 Interferometer-based techniques

- Imaging Fourier Transform Spectrometer: An imaging Fourier transform spectrometer is a device that does not make use of band-pass filters, but in contrast, it utilizes a Michelson interferometer. The Fourier transform spectrometer scans one mirror of a Michelson interferometer to obtain measurements at multiple optical path differences. Therefore, after an interval of time, a set of successive frames of the scene is captured and combined to have a full 2D image [14].

- Fabry-Perot Filter: It is a device made of two highly reflective mirrors separated a distance that is equal to an odd multiple of $\lambda/2$. Where λ is the desired wavelength to reach the detector surface. The space between the two mirrors is known as a resonant cavity. Therefore, when the light enters into the cavity it will be reflected between the mirrors, and only the beams with the selected wavelength will interfere constructively and therefore transmitted to the detector. The other beams of light with different wavelengths will interfere destructively and its transmission will plunge toward zero [67]. In addition to this, the transmission of the Fabry-Perot filter is not always perfect and therefore sometimes is necessary to use a combination of multiple cavity filters and mirrors [16].

3.2.2.2 Snapshot imaging techniques

3.2.2.2.1 Multispectral beam splitting

With this technique, it is possible to eliminate the use of additional dispersive lenses in the optical instrument and thus to reduce its size. Nevertheless, due to cumulative transmission losses, there is a maximum number of beam splitting filters that can be used. In addition to this, there are different layouts for a multispectral beamsplitter, at Figure 3.7 a) it is illustrated the sequence spectral filter. Other layouts are for example the well-known setup of beam splitters projecting each beam of light in a different detector, Figure 3.7 b). The main problem of these devices is the limit number of bands besides a high cost of production.

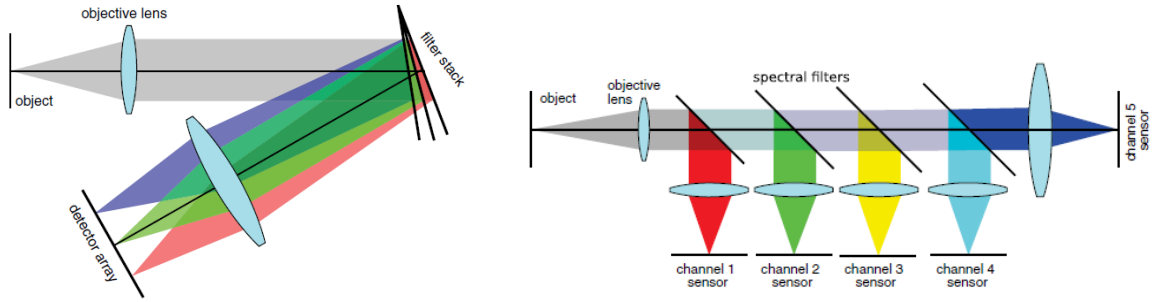

Figure 3.7: Multispectral beam splitting devices, a) sequence spectral filter, b) sequence of beem splitters. Both from [14]

3.2.2.2.2 Filtered Lenslet Array

The principle of this technique of multispectral imaging is to locate an array of lenses at the objective lens image plane, where commonly is located the detector. Moreover, in front of this array of lenses is located a multispectral filter array and behind of the lenses is the detector. Therefore, the array of lenses will form an image of the multispectral filter array into the detector. Then the projection into the pixels is rearranged in order to have a multispectral image [16]. This imaging technique is presented a Figure 3.8.

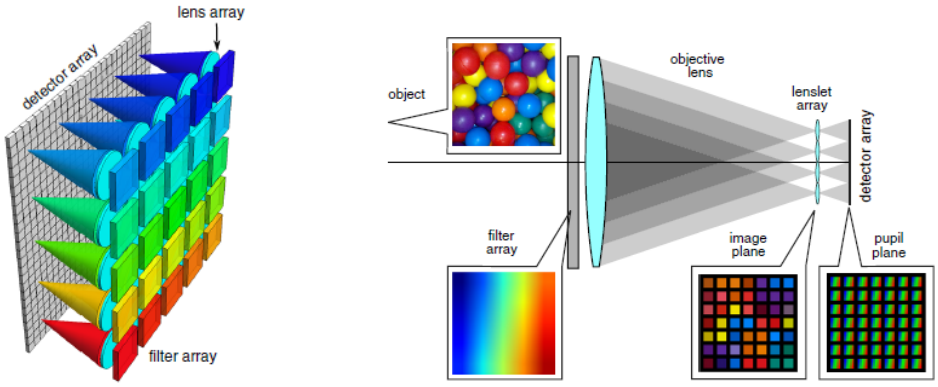

Figure 3.8: Filtered lenset array for multispectral imaging. [14]

Conceptually, this is a simpler method to have a multispectral image in comparison with the use of only the multispectral filter. Nevertheless, the filtered lenslet array technique needs from a uniform irradiance to capture a similar power of light in each lens. The maximum resolution is also lower than the multispectral filter array that will be next presented.

3.2.2.2.3 Multispectral Filter Array Approach (MSFA)

In general, depending on the use or not of a filter array over the detector FPA, it is possible to distinguish three different devices, monochrome sensors, colour sensors, and multispectral sensors. The monochrome detector captures all the wavelengths and cannot discriminate between them, therefore, a black and white image is obtained. On the other hand, the mosaicked colour filter array (CFA) uses of a three-colour array of filters, to capture three images, each one for each colour, to later combine them and possibly obtain a coloured image. For clarification, in a CFA only one spectral component is computed at each pixel and the other spectral components are estimated through interpolation of the neighbouring pixels in a process that is called demosaicing. Finally, a multispectral filter array approach (MSFA) is a combination of more than three different band-pass filters to capture with high detail a large number of specific wavelengths in comparison with a CFA array [69]. These three combinations are presented in Figure 3.9.

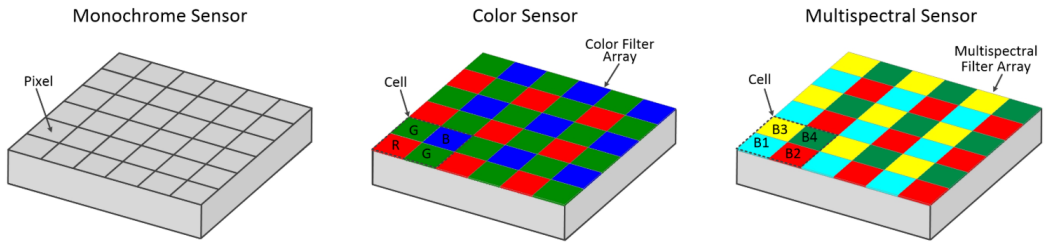

Figure 3.9: a) Monochrome sensor, b) colour filter array (CFA), c) multispectral filter array. [15]

In the design of a multispectral filter array, the spatial distribution of the different band-pass filters plays a very important role, especially when the number of bands is higher and therefore the transmitted wavelengths are closer. The filters, for example, can be arranged hexagonally, in a way that each pixel transmitting a specific spectral band is surrounded by six pixels of distinct bands. This configuration will be an advantage for the discussed demosaicing process where a full-colour image is reconstructed from the incomplete colour samples associated with the different band-pass filters, by an interpolation process [16]. It is also very important the uniform distribution of the filters of the same colour over the detector in order to avoid a degradation in the final full-colour image, [69] .

Ideally, the size of each filter of the array should be the pixel pitch of the detector. Nevertheless, the manufacturing process of MSFA detectors is of large complexity and the ideal concept of one filter per pixel has not been achieved yet without inquiring in a high cost of production. Because of that, usually, the size of each filter is designed to be 4x4 pixels or higher. An illustration of this concept is included in Figure 3.10.

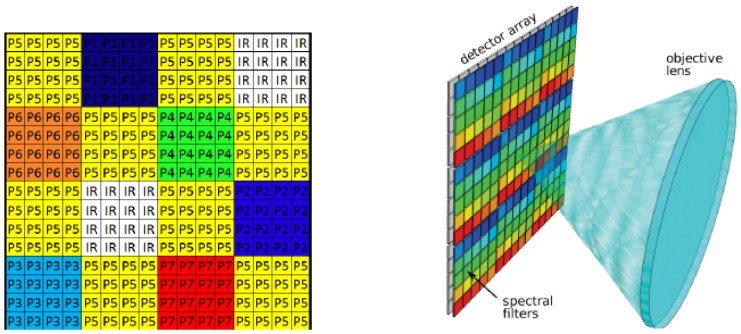

Figure 3.10: Spatial distribution of the band-pass filters in a multispectral array. [16] and [14] respectively.

Another disadvantage of an MSFA filter is the limit in the spectral band resolution. This is because an increase in the spectral resolution produces a corresponding loss in the total light flux that reaches the detector since each of the individual band-pass filters only allows to pass a specific beam of light. Therefore, a detector with a high quantum efficiency is required in order to incorporate a multispectral array [16]. That limits its use to the advanced HgCdTe, InSb, T2SL, InGaAs photodiodes in contrast to the low quantum efficiency detectors (lower than 40%) as QWIPs and extrinsic photodetectors.

Multispectral filters assemblies have been also developed for the thermal detector, in specific for the highly interesting microbolometers. This is the case of the 640x480 pixels and 25 μm pixel pitch microbolometer designed by the French manufacturer ULIS. It is implemented in the MISTIGRI (Micro Satellite for Thermal Infrared Ground Surface Imaging) space mission of the French space agency CNES. The microbolometer, which is uncooled, is designed for multispectral imaging in the wavelengths 8.6 μm, 9.1 μm, 10.3 μm and 11.5 μm. This capability is achieved by a multispectral array of four band-pass filters, as it can be seen in Figure 3.11, from [23].

One of the biggest problems that the MISTIGRI mission encountered, was the long time constants of the ULIS microbolometer. The response time of microbolometers

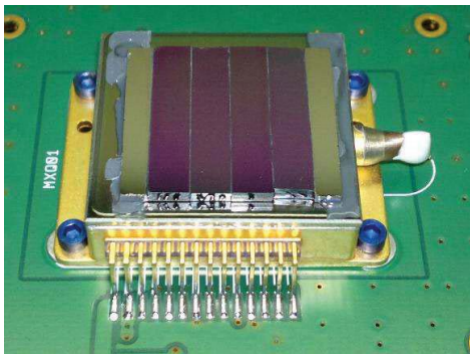

Figure 3.11: Four-bands LWIR microbolometer from the French manufacturer ULIS, used in the MISTIGRI satellite, with TDI capabilities. [17]

(time to reach 63% of the final output signal) is higher in comparison with photodetectors. The response time for the ULIS detector is 13.8 ms. This limits the operation of microbolometers in satellite mission. However, there are solutions, as the time-delay-integration (TDI) that can be used to improve this time constant. The TDI is described in Section 4.4.9.

3.2.2.2.3.1 Band-pass Filters construction

The main characteristics of a band-pass filter are the transmittance, the reflection and the absorbance. Then, as discussed before, they can be classified also into broadband pass filters and narrow band-pass filters. These properties are different depending on the material of the band-pass filter.

The first band-pass-filters employed metallic films. The metal film had a very high reflectance and absorbance. Then, it was coated with one or more dielectric thin films of appropriate refractive index and thickness in order to eliminate the reflection of the desired wavelengths while the others continued being reflected. Nevertheless, with the use of metallic filters, only a value of transmission in the order of 50% was achieved, due to the absorption factor of the metal films. Modern metallic band-pass filters improve the transmission properties by using a combination of metal films performing like the previously discussed Fabry-Perot filter [66].

Despite the improvements on metallic filters, the dielectric Fabry-Perot band-pass filter has become the most used. These filters are made of non-absorbing dielectric materials, and therefore, is possible to achieve large transmittance figures, higher than

90%. Furthermore, dielectric filters are implemented also with the multilayer Fabry-Perot interference technique. The higher number of layers and the higher number of cavities (space between the two first opposed layers of the cavity) the narrower the band-pass filter. For wide band-pass filters, it will be necessary to reduce the number of layers per cavity, but maintaining the total number of cavities to have the best properties of transmission [66]. Moreover, the dielectric filters can be coated to improve even more their properties and eventually reduce the number of layers needed and the total thickness of the band-pass filter. It is important to select the adequate materials for the specific spectral ranges in which the detector operates [70] [71].

Nowadays, with the use of micromachined technology, MEMS, is possible to develop Fabry-Perot cavities with a high degree of miniaturization. This supposes a great improvement in the performance of multispectral filter arrays [71].

3.2.2.2.3.2 Filters for dual band infrared imagers

State-of-the-art detectors with the capability of capturing the infrared radiation in two bands at the same time were discussed before. It is, for example, the case of the 'Condor II' HgCdTe photodetector from the Italian Leonardo company which at the moment is the best option for a multiband MWIR/LWIR CubeSat. These detectors are not only dual-band but also they can be used for multispectral imaging. For that later purpose, they require a set of band-pass filters as are needed by single band detectors but with the capability of reaching high transmission in both bands. To achieve this result, a dual-band antireflection coating needs to be added on the surface of each filter.

There are already available dual band coating for the infrared. These coatings are ticker than single band MWIR or LWIR coatings. Some examples of dual-band coatings are, zinc sulfide (ZnS) and yttrium fluoride (YF3) to be used in band-pass materials with a low to medium index of refraction; and germanium (Ge) for the materials with a high index of refraction. A combination of different coatings can also be used [72].

Once the band-pass filter has achieved a very high transmission in the MWIR and LWIR, is necessary to be sure that it will also block the region between 5 μm to 7 μm. The transmission vs wavelength plot of a dual band-pass filter is represented in Figure 3.12, [72] [73].

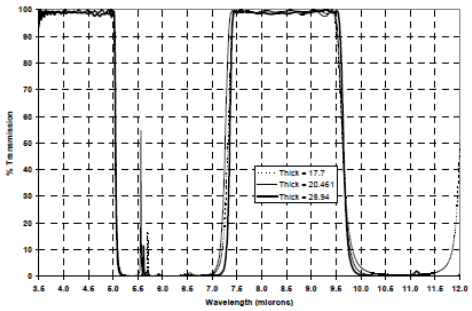

Figure 3.12: MWIR-LWIR dual-band pass filter. [18]

Moreover, it is also possible to build dual-band Fabry-Perot filters. It was discussed how Fabry-Perot filters offered the best properties of transmission and performance in the wavelength selection. Moreover, it was also seen the advances in the so-called FPF (micro Fabry-Perot filters) developed with the MEMS fabrication processes. In the construction of a dual-band Fabry-Perot filter, the main problem is the selection of a material with high reflectivity in both bands. After that, the Fabry-Perot cavity is constructed in a way that the first and second interference orders of it, correspond to the wavelengths of interest in the MWIR and LWIR region [19]. This concept is illustrated in Figure 3.13 a). Besides this, there is also the configuration in which the distance between opposite reflective surfaces in a Fabry-Perot filter, is modified by the use of a voltage to select the desired wavelength, Figure 3.13.

Therefore, after presenting these dual band-pass filters, the possible use of the 'Condor II' detector for the multiband CubeSat is even more interesting. Following this discussion there will be briefly presented the conventional optical devices used to split the light.

3.2.2.3 Dispersive prisms and diffraction gratings.

They are two of the most commonly used optical devices to produce the dispersion of the light. Starting with a dispersive prism, which is a device with an index of refraction that changes depending on the incident wavelength. Therefore the different colours of the light, associated each one to a wavelength, will be dispersed by the prism at different angles. On the other hand, a diffraction grating is an optical surface with a periodic structure that diffracts the incident light into multiple diffracted orders, and each of these orders is spectrally dispersed. By modifying the dimensions of

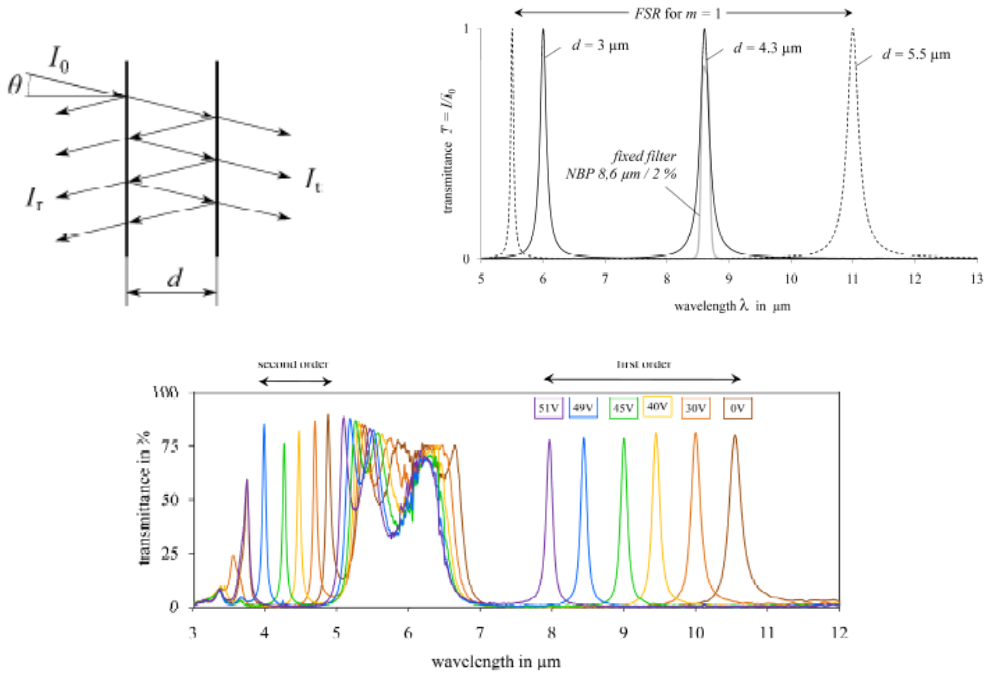

Figure 3.13: a) Fabry Perot cavity for the MWIR-LWIR wavelength selection, [16] b) interference orders of the Fabry-Perot cavity, c) interference orders of a voltage tunable Fabry-Perot cavity. [19]

the periodic structure, it will be possible to control the amount of dispersion of the wavelength in the orders [43].

These two optical devices are used in the so-call dispersive spectrometers. In this instrument, the light first enters into the imaging optics to be later directed into the dispersive optics element (prism or grating) to finally be projected into the detector FPA. Usually between the dispersive element and the detector there can be also used focusing or relay lens. Therefore, the light that reaches the detector will be split into its different colours or wavelengths what makes these instruments very adequate for multispectral and hyperspectral imaging [43] [74]. Multispectral corresponds to a lower number of wider bands, from 3 bands to 10 bands, while for hyperspectral imaging the number of bands is much higher, hundreds of bands, and therefore the wide of these bands is much smaller.

Nevertheless, it is very important not to confuse the use of a dispersive spectrometer in a scanning system or in a snapshot system. It was discussed how scanning instruments captures the light of the scene line by line, while snapshot instruments capture the light of the full scene in a unique shot.

In a traditional scanning mechanism, such as the pushbroom, the dispersive spectrometer instrument is designed to disperse the spectrum of light in one direction while the image is formed in the other direction in the detector FPA. The direction of dispersion needs to limit its extension to one pixel, if not, it will inquire in high chromatic aberrations. This is done line by line of the scene with the scanning instrument, to have at the end 2D image [74].

On the other hand, to use a prism or grating in a snapshot imager, it will be necessary to combine them with a band-pass device as the ones discussed in the previous section. Snapshot instruments using dispersive optics are in general very new instruments, the majority of them in development. This is the case for example of the image mapping spectrometer (IMS) instrument that combines an array of dispersive prisms with a lenslet array presented in Section 3.2.2.2.2, instead of using a multispectral array filter. This instrument allows to obtain multispectral images with a snapshot device, but it requires to have very precise optics to avoid image aberrations. The instrument is descrived in reference [14]. Another example could be to use a combination of a Fabry-Perot filter with a dispersive element.

It has been seen how prisms and gratings are very useful in multispectral/hyperspectral applications. Nevertheless, only scanning instruments with one of these dispersive elements have reached a good level of development. These devices have been used in several space missions as it could be for example the 'PRISMA' hyperspectral satellite mission launched in March 2019. This satellite from the Italian Space Agency, ASI, incorporated in a pushbroom scanning system, a prism to operate with 200 different bands [75].

For the CubeSat that is in development at the CSL the best option will be to use a multispectral array of filters if a snapshot technique is used, or gratings and prisms if a scanning device is used. Some configurations require from high precision in the optical design and, therefore, they could be not adequate to be used in a CubeSat.

As a remark, there have been already developed a CubeSats that uses a grating for multispectral capability in the Infrared region. The grating spectrometer utilized by the CIRAS CubeSat allows having a hyperspectral capability of 625 bands in the range from 4.08 μm to 5.13 μm. The spectrometer produces a 2D image at the detector FPA with one direction spatial and the other spectral. The CIRAS CubeSat use the scanning technique to capture the light coming from the scene. This CubeSat is described in detail in Chapter 7.

3.2.2.4 Dispersive grism

It is possible to make a combination of a prism and a grating in order to obtain another dispersive device known as grism. When the incoming light passes the grating part it is split into the different wavelengths but also it suffers from an angular deviation. The objective of the prims in a grism will be to refract the light back onto the straight path. This, for example, will reduce the field curvature aberration since the rays are redirected closer to the optical axis [74].

Dispersive grisms are very used for space applications, because their design and properties allow reducing the distances between the optical lenses and collimator after the grism, and therefore, to possibly have more compact optical instruments. Instruments as the NIRCam of the James Webb Space Telescope, for the 0.5 μm to 5 μm wavelength range, incorporate dispersive grisms [36].

3.3 Conclusions

Dual-band technology is already available at the market. The German AIM is offering a dual-band T2SL MWIR-MWIR, the American QimagiQ provides with a dual-band QWIP MWIR-LWIR photodetector and finally the Italian (manufacturing in the UK) Leonardo, offers a dual-band MWIR-LWIR HgCdTe. The main issue of these three detectors is their operational temperatures, lower than 100 K. All three materials have been used for a space mission. Some of them, like the QWIP detector, has major drawbacks as a quantum efficiency lower than 10 %. The reason while they are constructed is because of the relative facility to achieve dual-band QWIPs in comparison with other materials. These detectors are going to be also numerically compared in Chapter 6. At the moment, the Condor II, dual-band detector from Leonardo is the best option. Also because there has been positive feedback after contacting the company.

On the other hand, the multispectral technology. The use of band-filters is a very important option to take into account to reach multiband detectivity not only in a single band but also in the dual band. This is the case of the band-pass filters for dual-band infrared detectors. This allows, for example, to have a subdivision of bands inside each wide band of the Leonardo Condor II MWIR-LWIR detector. A very innovative idea for a future mission.

Several other optical filters have been also discussed for scanning and snapshot satellites. In a snapshot satellite, the best option is to use a multispectral array since the lenslet array still a very new technology. For the case of scanning systems, there are two options. On one side, the traditional prisms, gratings and grisms. On the other side, it can be also used band-pass filters, as it was done in the ULIS microbolometer incorporated in the MISTIGRI satellite mission. As a result, the first decision must be if the CubeSat, in this case, will be scanning or snapshot.

Chapter 4

Working principle of infrared detectors

4.1 Introduction

In general, infrared detectors are complex electronic devices adapted for the application in which they are used. As a result, there are differences not only between detectors of different materials but also between infrared detectors using the same material for the FPA. These differences are mainly located in the electronic module or read-out circuit (ROIC), attached to the FPA.

The ROIC will be characterized by specific time constants. Once the radiation from the target reaches the detector, it will be necessary to convert and compute it into a voltage/current that can be registered to have finally an infrared image. Each of the components of the ROIC will be in charge of one task in a defined interval of time. In this chapter it will be presented how the photons are read-out, differentiating between photodetectors and thermal detectors. Also, it will be done a differentiation between the different ROIC architectures CCD and CMOS.

It will be possible to see the limitations of thermal detectors in comparison with photodetectors. In addition to this, it will be presented a solution for solving the response time problem of thermal detector bolometers used in a satellite. This solution is the so-call time delay integration.

4.2 Types of focal plane arrays

The main element of an infrared imaging system is the FPA. There are several different FPAs architectures as it has been discussed in previous sections. This is the example

of the photoconductor, photodiode, QWIP and QDIP architectures, besides others as the state of the art barrier nBn/pBn architectures to reduce the dark current (the current that remains in the circuits even when the detector is switched off) present in infrared detectors. In addition to this, it is possible to do a more general classification of architectures, distinguishing between monolithic and hybrid architectures [7]. The main features of them are next discussed.

- **Monolithic architecture:** in this approach, the detection of the incoming light and the following readout is done in the detector material. It does not use an external circuit for the read-out. This technology appears in photodetectors as the PtSi Schottky-barrier detectors and is also characteristic of the uncooled silicon microbolometers. The main advantage that they offer is a reduction in the number of processing steps what is related with lower values of noise. In spite of this, this architecture has not reached the degree of development of hybrid photodetectors.

- **Hybrid architecture:** it is the structure used by the majority of infrared detectors. This is the case for HgCdTe, T2SL, InGaAs, InSb or QWIP photoconductors among others as modern VO_x microbolometer thermal detectors. It is also known as sensor chip assembly (SCA). In this approach, the material of the FPA and the chip containing the read-out circuits are different. The readout chip circuits are in general made of silicon. It is possible to find two different types of silicon addressing circuits, CCD and CMOS, which are going to be presented in the next section. Continuing with the hybrid structure, one of its main advantages is a higher fill factor (percentage of the pixel surface sensitive to radiation) in comparison with the monolithic structures. Another advantage is the possibility of separately optimize both components, the FPA and the read-out circuit in contrast with the complex optimization process of monolithic arrays [7].

4.3 The read-out process

The FPA sensitive part of photodetectors and thermal detectors capture differently the incoming infrared radiation. It has been presented how photodetector FPAs converts the incoming flux of photons into electrons, and then this charge will be integrated and processed in the read-out unit. On the other hand, the FPA of thermal detectors

reacts changing its temperature what will produce a variation in the resistance in the case of the bolometers or the electrical charge in the case of pyroelectric detectors. This last variation is going to be measured and computed by the read out-circuit. Therefore, even if they both have a hybrid architecture, the read-out in the CCD or CMOS addressing circuit will be different. As discussed before, the main two types of silicon read-out integrated circuits (ROICs), are CCD and CMOS. CCD refers to Charge-Coupled Device while CMOS refers to Complementary Oxide-Semiconductor. The differences between them are next presented, individually for each type of infrared detector.

4.3.1 Photodetectors

The FPA of a photodetector is first exposed to a signal of infrared radiation. This signal contains a flux of photons coming from the target, but also photons coming from the background of the target. After that, the hybrid architecture of the photodetector (FPA joined to the ROIC) will carry on two main functions. The conversion of photons to electrons and the conversion of the charge to voltage/current signal.

4.3.1.1 CCD architecture

In the CCD architecture, the conversion of the photons into electrons is performed in each pixel of the FPA. Each photon of light captured by the pixel will be converted to one or more electrons. The electrons obtained, during the exposure time of the pixels to the incoming radiation, will be stored in the pixel in the so-call potential wells. These potential wells have a capacity for a specific number of electrons. It is said that the detector is saturated or overexposed when the potential wells cannot store more electrons. This amount of electrons that the pixel can store is known as the full well capacity. It is a very important parameter since is very common to find in the manufacturer data sheets that a specific parameter has been calculated with for example 50% of full well capacity. The best conditions to take an image, in term of signal-to-noise ratio, will be to have an exposure time as closely as possible to the saturation [76] [20].

After the conversion of photons into electrons, in CCD detectors, the next step is to transfer the charge of each pixel to a capacitor in which it will be integrated. In order to do that, the charge of each pixel is moved downwards, row by row, towards a final row. This final row is known as readout register, as indicated in Figure 4.1 which

illustrated a CCD array. In the readout register row, the charge will be transferred horizontally along with the readout register until a capacitor [76] [1]. The charge of each pixel remains always separate from the charge of the other pixels [20].

At this point is where the so-call read-out process for the measurement of the charge starts. In the capacitor, the charge of electrons (for each pixel individually) will be integrated in order to convert it into a voltage or a current that can be measured. For example, a typical conversion factor is to obtain a voltage around 5 μV to 10 μV per electron. Nevertheless, the signal is usually very small, and therefore it needs to be amplified. This is done by an amplifier device. In addition to this, the capacitor is also connected to a reset transistor to clean it after each conversion to voltage, since there could be a remaining charge that at the end will increase the noise in the read-out. This read-out process is carried on for each pixel in order to have them registered and with an assigned voltage to each one. The last step is to digitize these values into grey values to finally have the desired infrared image [76] [20].

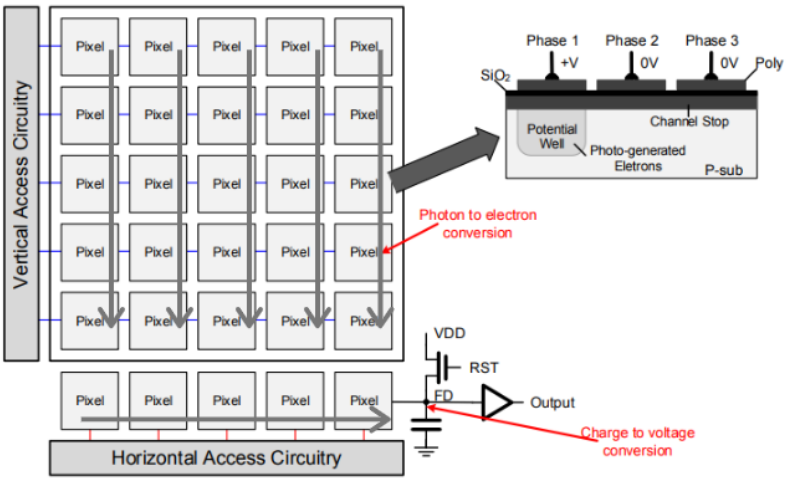

Figure 4.1: Operational principle of the CCD read-out circuit architecture.[20]

As a remark, there are different types of CCD architectures. The one explained is the full-frame architecture, but there is also the frame transfer, which includes a storage array section, for the charge, between the last row of the imaging area and the readout register. Also, there is the interline transfer CCD in which columns for imaging and columns for storage and charge transfer are intercalated through the array. Full-frame is the simplest architecture and in comparison with frame transfer, full-frame needs to use a shutter to stop the exposure time of the pixels. On the other hand, frame transfer can be continuously exposed to the incoming infrared radiation

since it has the storage array. Nevertheless, frame transfer devices are expensive and the sensor size is larger than full-frame [77]. The most commonly used for space instrumentations is the full-frame design [34]. Finally, the interline CCD architecture, which allows faster imaging in comparison with the other two architectures, but has the disadvantage of having a lower sensitive part [77].

4.3.1.2 CMOS architecture

In this read-out circuit approach, the conversion of the photons to electrons is carried on within the pixel, as in the CCD architecture, but in contrast, the conversion of the charge to a current/voltage in CMOS ROICs is individually done for each pixel but also within the pixel. Therefore, there is not a transfer of charge row by row to a readout register as in the case of CCD arrays [1].

In CMOS arrays there are also potential wells to store the converted electrons. Then the electron charge of each pixel is integrated into an in-pixel capacitor to convert it into a voltage and after it is amplified in an in-pixel amplifier since the signals are very small. In addition to this, each pixel also contains a reset transistor to clean up the charge of the pixels. Finally, all these pixels will be connected to a readout circuitry where the different voltages will be digitized into grey values computed to have the infrared image [20]. An illustration of a CMOS array is included in Figure 4.2.

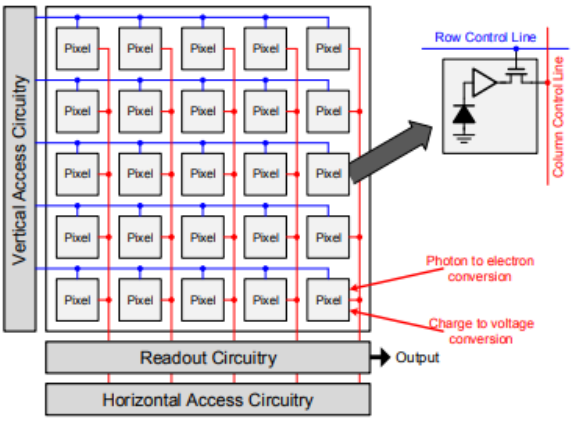

Figure 4.2: Operational principle of the CMOS read-out circuit architecture. [20]

4.3.1.3 CCD architecture vs. CMOS architecture

CCDs arrays were the first type of architecture developed for hybrid detectors (were the FPA and ROIC are two separate modules). After them, CMOS detectors appeared as a result of the research in high-speed read-out circuits. CMOS detectors allow reaching higher frames rates due to its velocity. Nevertheless, this increase in speed is related to a disadvantageous increase in the noise, which could limit the maximum size of the array [7] [78]. Therefore, the selection of a CMOS cannot be taken for granted. The selection of a CCD or a CMOS has to be selected depending on the requisites of the mission.

One of the first parameters of comparison may be the responsivity. Defined as the output voltage per unit of incident radiation. In this case, CMOS detectors offer a better response as a result of how they are internally constructed. Nevertheless, the uniformity of this response for the different pixels of the array is lower compared with a CCD under the same illumination conditions. Moreover, CCDs arrays are more sensitive to the incoming radiations. This is because detectors with a CMOS ROIC, have a lower dynamic range, which means, that they can store fewer electrons in the potential wells of the pixels which were described in the previous section [20] [78]. The fill factor (sensitive part of the pixel), is larger for CCD structures. Therefore, for the same incoming radiation, the quantum efficiency of the detectors which implements a CCD ROIC is higher than the CMOS detectors [20].

Referring to the circuit noise of both types of architectures, CCD present also some advantages over CMOS. This is related to higher complexity in the read-out circuits of the CMOS arrays. As long as each pixel has a capacitor, an amplifier and a reset transistor, the final total noise will be higher than in a CCD where the readout register is usually only one (or a fewer number) and can be easier optimized. The reset transistor and amplifier are also sources of noise. As a result, CCD can be larger than a CMOS detector for the same total noise [78]. As a remark, it is important to notice that in a CCD, if one pixel fails, all the row will be affected, while in CMOS the problem will be isolated to the pixel [1].

On the other hand, CMOS architectures offer very attractive characteristics. This is the case of a fast read-out process. The read-out, generally, starts once the exposure time of the pixels has finished. As a result, the frame rate, number of images per second, can be increased with the use of CMOS detectors. Also, the power consumption of CMOS is lower in comparison with CCD detectors [61] [78].

Other advantages of CMOS arrays, is that the implementation of a global shutter on them is easier than for a CCD [78]. A global shutter stops the exposure time of the pixels without using a physical movable part. The movable shutters are called rolling shutters. Both CMOS and CCD architectures can be used for snapshot imaging and scanning imaging.

4.3.1.4 CCD and CMOS architecture for space instrumentation

A very important feature is to compare the use of CCD and CMOS detectors in space missions. CCDs architectures have been largely used in space instruments. Their first use was in 1984 in the Russian Vega probe to image the comet Halley in 1986. After that, they have been used in mainly all the observation satellite missions. On the other hand, this is not the case for CMOS detectors [34].

The internal structure of CMOS detectors gives them a higher radiation hardness in comparison with CCD architectures. Under the same ionising radiation, CMOS pixels will be less degraded and damaged than CCDs, which is a very attractive characteristic due to the space environment nature. In addition to this, it was discussed before how power consumption was also better for CMOS detectors. Nevertheless, these two characteristics are overpassed by the higher dynamic range of CCD arrays [34] [20]. For some wavelengths of observation, the number of photons is very low and it will be very advantageous to possibly expose the pixels for a longer time in order to have a higher signal to noise ratio, SNR. Furthermore, CCD hybrid detectors are less noisy and that also positivelly influences in the SNR [20].

In the last two decades, the major use of CMOS detectors in space was for star trackers and inspection cameras. Despite this, nowadays the CMOS architecture has reached a high degree of development. For example, the Time Delay Integration (TDI) technique, that will be described later in this chapter, was only possible for CCD detectors until a few years ago. This is a method to increase the signal-to-noise ratio of the detectors, by accumulating the signal captured in successive pixels. It is commonly implemented in satellites with a scanning optical instrument [34]. Nevertheless, now is possible to find great advances in CMOS detectors with TDI functions, which increases the velocity of imaging and therefore reduces the time constants which are commonly a constraint for high demanding applications [20].

Another advantage of the use of CMOS detectors is their low power and also commonly lower size, two very positive features for their use in a CubeSat. Nowadays,

the majority of manufacturers of infrared detectors, as it could be the Israeli SCD or the Americans Teledyne or FLIR, offer a larger variety of CMOS detectors comparing with CCD detectors [5] [38] [79]. For example, the manufacturer Teledyne, has provided with CMOS detectors for the visible and near-infrared range to different ESA missions. This is the case of the ESAs and EUMETSATs Meteosat Third generation satellites. Also, the CMOS image sensor from Teledyne used for the ESAs JUICE mission [79]. Moreover, companies as Deltatec in Belgium are developing hyperspectral CMOS sensors for their use in satellites.

The main characteristics that differentiate CMOS and CCD architectures are presented in Table 4.1.

Parameter	CCD	CMOS
Responsivity	Lower	Higher
Uniformity of the response	Higher	Lower
Dynamic range	Higher	Lower
Fill factor	Higher	Lower
Read-out noise	Lower	Higher
Speed (read-out)	Lower	Higher
Complexity of construction	Lower	Higher
Power consumption	Higher	Lower
Radiation hardness	Lower	Higher

Table 4.1: Comparison of the main properties of CCD and CMOS ROIC architectures. The terms lower and higher are used to compare the parameters between them.

4.3.2 CCD and CMOS architectures for thermal detectors

In the last years, the advances achieved in the read-out circuits for thermal detectors are very noticeable. The type of thermal detector that presents more advantages to be implemented in a CubeSat is the MEMS microbolometer. It was seen that there are microbolometers with the monolithic and hybrid structure. Within the monolithic architecture, were the FPA sensitive part and the ROIC are made of the same material, it is possible to find a-Si CCD microbolometers and a-Si CMOS microbolometers. a-Si monolithic structures have advantages like a higher read-out velocity in comparison with hybrid microbolometers, but despite this, it is a technology still in development [61].

On the other hand, hybrid microbolometers have different materials for the FPA and the ROIC. The FPA is mainly made of VO_x while the ROIC is made of silicon. It

has been discussed before how the thermal detector converts the change in temperature of the FPA (due to the incoming radiation) into a measurable electrical parameter. For microbolometers, this physical parameter is a change in the resistances incorporated at each pixel. Then the ROIC, CCD or CMOS, will convert the electrical parameter signal into a voltage as it was done in the photodetector ROICs. Then the voltage will be registered into the corresponding processing unit. Therefore, the ROIC of thermal detectors contains also integrators and amplifiers, to obtain the final voltage [80]. At Figure 4.3 a) it is represented a microbolometer pixel and its integration into a CMOS read-out circuit. At Figure 4.3 b) it is represented the ROIC for one pixel for a CMOS detector.

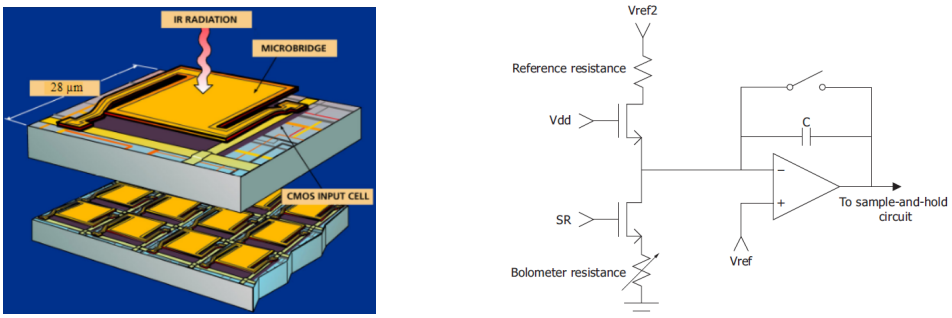

Figure 4.3: CMOS microbolometer a) pixel structure, b) circuit electronics of each CMOS pixel.[21]

Therefore, CCD and CMOS concepts are equal for photodetectors and thermal detectors. Again in the case of CMOS detectors, at the same pixel takes place the conversion of the change in the resistance to a signal; and the integration of this signal into a voltage and following amplification. In addition to this, it is possible to distinguish between three types of internal circuit architectures for the CCD and CMOS ROICs. Nevertheless, this is out of the scope of this project and they will be just cited. There are column-wise ROICs, serial ROICs and the most advanced, pixel-wise readout architecture [80].

4.4 Characteristics times of infrared detectors

The time constants, the noise and the sensitivity, are the three main parameters to take into account for the selection of an infrared detector. Moreover, for space applications, their role is even more important since the optical instrumentation will be under very constraining requisites. The satellites travel at a very high velocity and

that implies very fast imaging. In this case, a reduction in the time constants will be very advantageous, but on the other hand, it will imply in general an increase of the noise levels and therefore a loss of quality in the final image. Therefore, a compromise between the cited three main parameters must be carried on. In this section there will be presented the different time constants related to an infrared detector. As a remark, it is important to mention the complexity encountered into the determination and distinction of these times since between the different bibliographic sources there was not a clear distinction in the name used for the different terms. In addition to this, some of the assumptions made during the research process were clarified after contacting by e-mail with companies as the Americans Teledyne and FLIR, and the Belgian Xenics [50] [81] [38].

4.4.1 Integration time of the satellite

The optical instrument used in a satellite mission will be characterized by a specific spatial resolution. This spatial resolution can be described with the so-call ground sampling distance (GSD). Each of the pixels of the infrared FPA of the camera will be associated with an area in the ground. The imaging system cannot differentiate elements smaller than this area, which is equal to the square root of the ground sampling distance (for an array with the same number of pixels in the horizontal and vertical direction). The ground sampling distance can be defined also as the distance in the ground between the centre of two consecutive pixels of the FPA [1].

The integration time of the satellite will be the time needed to pass over the GSD distance. Therefore, its value depends on the GSD value and in the velocity of the satellite at a specific orbit. This relation is represented in Equation 4.1.

$$T_{int} = \frac{GSD}{v_{\text{sat,ground}}} \tag{4.1}$$

Where the GSD is in meters and v_{sat},ground, the velocity of the satellite with respect to the ground, is in meters/second. Nevertheless, in general, the integration time of the satellite is expressed in milliseconds.

For example, if the GSD is 100 m and the velocity of the satellite is 7.07 km/s, corresponding at an altitude of 550 m, the integration time will be close to 14 ms. This example will be used in the explanation of the other time constants for easier comprehension of the times.

4.4.2 Exposure time of the detector

In order to capture the incoming flux of infrared radiation, the pixels must be exposed to it. The time that they are directly capturing the photons is known as exposure time. There is a limit for this time and it is related to the dynamic range explained in the CCD. The dynamic range refers to the maximum number of photons that the array can receive before saturation [76]. As a result, it is not convenient to have an exposure time longer than the saturation time. If not, a shine and low quality image will be obtained because the system has been overexposed. The best exposure time is then when it is close to the saturation limit. At this point, the signal-to-noise ratio SNR will be the maximum possible. As an example, the FLIR 'Neutrino SWAP+C' has a well capacity of $7{\cdot}10^6$ electrons [38].

It is clear that the exposure time of the pixels depends on the illumination conditions. Shorter exposure times for bright scenes and the opposite for dark scenes. In addition to this, and following the logic, the exposure time cannot be larger than the integration time of the satellite, if not, the detector will be capturing photons from a different GDS. The exposure times can be very short in the order of microseconds or larger in the order of a few milliseconds, from the manufacturers datasheets.

In addition to this, a parameter to also take into account when selecting the exposure time is the sensitivity of the detector. Detectors with a larger sensitivity, that can be related with the specific detectivity D^*, need less time to capture the light from a specific scene in comparison with a less sensitive detector as it can be the case of a thermal detector [6].

4.4.3 Response time of the detector

The response time was presented in previous chapters as one of the detectors figures of merit. It was defined as the time that the detector output signal needs to reach 63% of its final value. In the case of thermal detectors, the response time is also known as thermal time constant.

For photodetectors, this time is in the order of microseconds. Its response time can be described by a step function. But for thermal detectors, and specially microbolometers, the response time is represented as an exponential function. The general rule is that a microbolometer needs three times its thermal time constant (response time) to reach a 95% of the final signal, and five times to reach a 99% of its final value.

For example, in the datasheet of the VO_x microbolometer 'Bird XGA' from SCD, it is indicated a thermal time constant (they refer to it as tau) of 8 ms for the STD, 8 μm to 14 μm infrared range setup. This 8 ms is the time to reach 63% of the final value. Therefore to have 95% of the signal it will be necessary 24 ms [49]. If your exposure time (time for the pixels capturing light) is lower than 24 ms, the final image will be blurred.

As a result, if it is needed at least 24 ms of exposure time, the detector will be not compatible with the 14 ms of integration time of the satellite example. In order to fit with the satellite requirements, the final image will be always blurred. This concept is equal for a snapshot or for a scanning system.

In general, the response time of thermal detectors is larger than 7 ms and it cannot be reduced even with cooling. However, there were already mentioned satellite missions using microbolometers, as the MISTIGRI or the FUEGO satellite missions [23] [35]. These two missions use a CCD microbolometer from the French manufacturer ULIS. In order to solve the problem of the response time they use the Time Delay Integration technique, among others, that will be presented in Section 4.4.9.

4.4.4 Integration time of the read-out circuit (ROIC)

It has been discussed how the first step to measuring the incoming flux of photons is to convert it into a charge of electrons in the case of a photodetector, and into a measurable signal coming from the change in resistance in the case of microbolometers. This is carried on by the FPA sensitive part. On the other hand, CCD and CMOS architectures perform the read-out of the signal.

The read-out time will be split into two parts. The circuit integration time and the read-out of the charge. The circuit integration time is independent and different from the exposure time [82]. It is defined as the time interval in which the charge is trap and retained into the potential wells of the FPA. It also includes the time in which the charge is transported towards the capacitor. The next steps, the conversion of the charge into a voltage and the registration of the voltage values are part of the second time, the read-out of the charge [83] [20] [82] [76].

Coming back to the circuit integration time, it begins after the reset transistor, responsible for cleaning the possible charge left from other frames, has finished its operation. Then, it will extend after the exposure time has finished. As a result, the exposure time can be shorter than the circuit integration time. It is commonly

used the term of effective exposure as the interval in which the sensor is exposing and integrating at the same time [20] [82].

The circuit integration time can go from microseconds to milliseconds. The time is selected according to the frequency in Hertz in which the circuits of the ROICs are operating. Usually, manufacturers provide with an interval of circuit integration times associated with a range of frequencies. The duration of these processes will be related also with the noise generated.

As a remark, it is commonly used in the bibliography, the exposure time and the circuit integration time concepts without distinction. This can only be done when the sensor has a global shutter and not a mechanical rolling shutter [83]. In the case of a global shutter, the integration time starts and finish at the same time for all the rows as it will be explained in Section 4.4.8.

4.4.5 Time for the reading-out of the charge

It covers, on one hand, the integration of the charge already in the capacitor to convert the charge into a voltage. On the other hand, it also covers the process after the capacitor where the voltage passes through an amplifier to be later registered. This is a very critical part in terms of noise generation. It always starts once the circuit integration has finished (from conversations with the manufacturer Teledyne [81]). Nevertheless, it can finish when the frame rate finishes or it can continue even when the next frame has already started. Therefore, it is possible to talk about two modes of read-out. Integrate then reading (ITR) or integrate while reading (IWR). In general, in the specifications of the infrared detectors, it is indicated in which mode the ROIC operates, or if it can eventually operate in both modes [84].

In the first mode integrate then reading (ITR), the circuit integration time and the read-out of the charge will always follow a sequential order, without interfering between them. This configuration allows enhancing the noise values of the ROIC. Nevertheless, the time between frames will be longer. In addition to this, there is also a time after the read-out of the charge for the reset transistor operation. This interval is also within the frame [84].

On the other hand, in the mode integrate while reading (IWR), it is possible to start the exposure time for the next frame and therefore also the circuit integration of the next frame without having finished the read-out of the charge of the previous frame. The reset transistor will act also in the next frame. This configuration allows to

have faster frame rates, but on the other hand, the interference between time constants will increase the noise levels of the device [84].

It is important to remark, these mode selected will not affect the response time of the infrared detector which is a fixed value.

4.4.6 Idling/clearing of the detector

After each observation or frame, in the capacitor and amplifier, there can be a residual charge from the last observation. If this charge is not cleaned up after each read-out, the noise of the detector will be higher and the observation will be contaminated by the information that does not correspond to the current frame. In order to avoid it, after each read-out of the charge, there is an interval of time to clean the remaining charge. This process is known as idling or clearing and it will be carried on by the reset transistor [20] [82].

4.4.7 Frame rate of the detector

This parameter defines the number of observations that an optical system can do in one second. The frame rate selection will be dependent on all the previously described time constants. For example, if the scene is very shiny, the exposure time will be reduced and the frame rate can be increased. The frame rate will be selected depending on the application. In the case of a snapshot satellite, the camera will take an image when it is at the centre of the scene area, and therefore the frame rate does not play an important role as it is the case for the exposure time.

The frame rate is usually presented with Hertz units. Continuing with the example of the SCD 'Bird XGA' infrared CMOS microbolometer, on the datasheet, it is indicated that it can reach 30 Hz and 60 Hz frame rates [5]. The Hz is the inverse of the second. The time between observations corresponding to 30 Hz frame rate, will be 33.33 ms. On the other hand, it was indicated how the time to reach 95% of the final output signal in the SCD detector, was 24 ms. Therefore, there is enough time to reach a proper signal within the frame. The read-out of the charge and the idling must be adapted to the remaining interval of time in this 33.33 ms.

But this detector offers also a 60 Hz configuration. 60 Hz frame rate corresponds to an image each 16.67 ms. But the response time is 24 ms. That means that the exposure time finish before the detector output signal has reached 95% of its final value. The cost of this faster frame rate will be a lower resolution, the image will be

blurred. Nevertheless, as it can be assumed, the detector is adapted to these higher frame rates. In order to do this, a technique known as binning or windowing of the pixels is used.

The objective of the binning is to combine the charge from several pixels of the detector. This will imply a reduction of the spatial resolution, but an increase in the read-out times. For example, the SCD detector is a CMOS 1024x768 pixels. If a binning of 4 pixels by 4 pixels is done, the detector will act as a 256x192 pixels FPA. The quality of the final image will be reduced, but on the other hand, the exposure times and read-out times are also reduced. As a result, the detector can operate at higher frame rates [85] [86].

All the discussed time constants are presented in Figure 4.4 to facilitate the understanding of them.

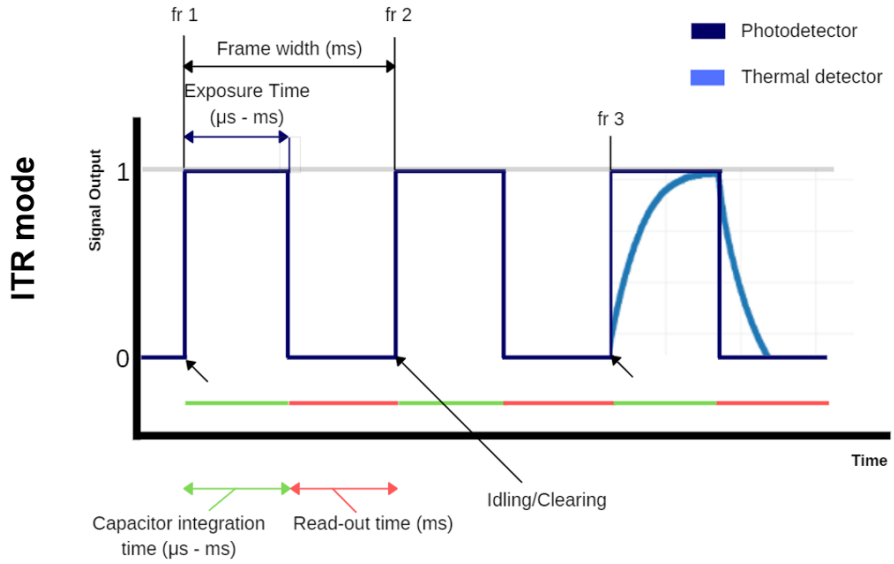

Figure 4.4: Characteristic time constants for the FPA and read-out circuits of infrared detectors. The read-out mode is ITR (integrate then read).

4.4.8 Controlling the exposure times

In general, traditional infrared detectors incorporate a mechanical shutter to control the exposure of the pixels to the incident radiation. This type of shutter receives the name of rolling shutter or chopper. The issue with this rotating device is that the pixels of the detector will be exposed at different times. When the trailing edge of the shutter passes over the first row of the detector this row is exposed to light and

then the shutter moves and the second row will be exposed, the similar procedure for all the pixels rows. At the end, when the trailing edge of the shutter passes over the last row, the other side of the shutter will start closing the first row exposed. As a result, the interval in which the circuit integration time takes place is different for the different pixels or rows (depending on if it is a CMOS or a CCD). It follows a sequence as it is illustrated in Figure 4.5 a). This configuration produces a lower noise and is less complex in terms of electronic design [22].

The problem of using a rolling shutter in a camera in movement, as it can be the case of a satellite optical system, is that the final image will suffer from distortion. Therefore, it is not a possibility to implement a rolling shutter for the optical instrument of a satellite. The infrared detectors that can be selected are the ones with a global shutter.

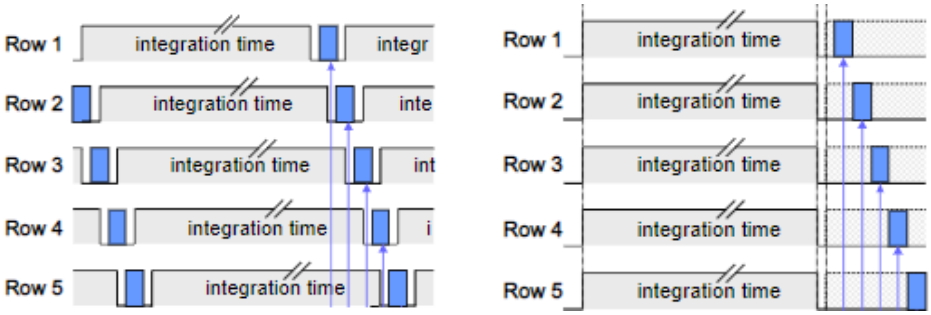

Figure 4.5: Differences in the exposure time control for a) rolling shutters, b) electronic global shutter. [22]

An electronic global shutter allows exposure all the pixels of the array at the same time. As a result, the circuit integration interval will occur at the same time for all the pixels. After that, each pixel or row will sequentially carry on the read-out process. This configuration is illustrated in Figure 4.5 b). The disadvantages of a global shutter are related to higher complexity of design besides larger values of noise in comparison with a rolling shutter [22]. Some manufacturers like the American FLIR, offer infrared detectors with both configurations, rolling shutter and global shutter. This is the case of the already cited type II superlattice 'Neutrino SWaP + C' photodetector for the MWIR range [38].

4.4.9 Response time solution for microbolometers thermal detectors. Time delay integration

The large response time of microbolometers is the main limit to use them in optical instruments for space missions. In the example discussed before, the integration time of the satellite was 14 ms, and the time for the microbolometer output signal to reach 95% of its final value was 24 ms. If the microbolometer is only exposed 14 ms, the resolution of the final image will be very low. A resolution that will not be acceptable for the majority of the space missions. Nevertheless, it is possible to find space missions that implement a microbolometer. This is the case of the MISTIGRI microsatellite, developed by the CNES [23]; the future FUEGO mission [35], developed by the CNES and the ESA; or also, the JEM-EUSO instrument that will be attached to the ISS [28]. The three main space agencies ESA, JAXA and NASA are in charge of the development of the JEM-EUSO instrument.

In order to capture the scene, these mission use a scanning pushbroom instrument. Furthermore, the three devices use a technique known as time delay integration (TDI) when capturing the scene. Thanks to the TDI, they manage to solve the problem of the long response time of microbolometers.

The main idea of time delay integration is to capture the light from the same scene several times with different pixels. It is commonly used in scanning devices with the CCD read-out architecture. However, there have been also developed CMOS ROICs with the capacity to so TDI. Traditional scanning sensors have only one row that displaces along the track with the satellite movement. The pixels of this row capture the ground scene only once. In contrast to this, TDI sensors have more than one row. The objective is to scan several times (with the different rows) the same scene. Then, the signal of the same scene captured by the different pixels is accumulated to have finally a high-resolution image [20].

In Figure 4.6 it is illustrated the TDI technique with a four rows sensor. In a time t1, the first pixel of the first row captures the object A, the signal is A1. In a time t2, the second pixel of the second row captures again the same object A, the signal is equal to A1, but it is represented as A2 because it is the sum of the two object signals. The same for a time 3, where A3 is the signal accumulated in the last three steps. As a remark, the exposure time is individual for each position, but the read-out is done only once at the end of the accumulation of all the signal rows.

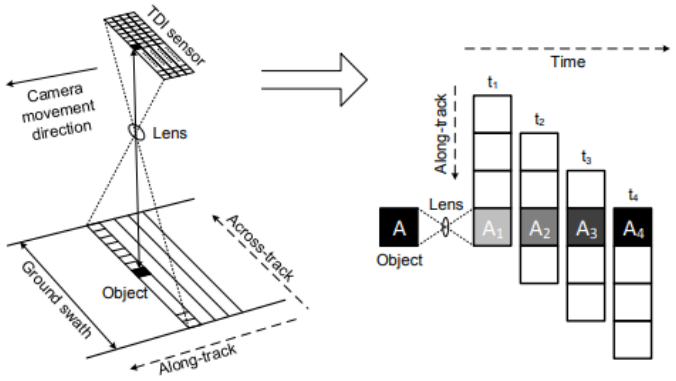

Figure 4.6: Time delay integration, TDI, concept to increase the signal received from the target; used to solve the response time problem of microbolometers. [20]

Depending on the number of signals accumulated, is possible to talk about TDI 4, TDI 10, etc. As an example, the detector TDI 480 from SCD, is a 480x6pixels sensor made of HgCdTe, able to do TDI in the LWIR. It is a TDI 6 detector and therefore the signal coming from the same object will be accumulated 6 times [5]. This detector is oriented to high resolution and sensitive purposes.

Another high interesting example is the microbolometer used by the mission MIST-IGRI which was already presented in the previous chapter of multispectral arrays. This 640x480 pixels and 25 μm pixel pitch sensor allowed multispectral imaging in the LWIR in the bands 8.6 μm, 9.1 μm, 10.3 μm and 11.5 μm. The detector, from the French manufacturer ULIS, was utilized within a scanning optical instrument. In order to solve the problem of the response time, it used a TDI of 30 lines for each of the four wavelengths of interest. The band-pass filters had the same width as it was illustrated in Figure 3.11. Each one of them covered 120 rows of the sensor. Then, inside each 120-row range, 30 lines were used to do TDI. It is not indicated in the bibliography the use for the other 90 lines for each band [23]. Nevertheless, and according to the research done in this chapter, it is understood that these lines were used for the read-out of the total signal captured.

An the end, this detector operated with four TDI 30. This technique can be considered as one of the main solutions for possibly use a microbolometer in a CubeSat.

One of the major drawbacks of the TDI technique is that it requires very precise optics. Each pixel of the TDI row must capture exactly the same scene as the previous and following pixel of the row. This may be an issue for very small CubeSats where it is not possible to incorporate very high precision optics but also a very precise attitude

control unit.

In addition to this, there are other two techniques useful to increase the signal that is reaching the detector. On one hand, these techniques cannot be compared to TDI, which is the best option for high demanding applications, but on the other hand, they can be used in combination with TDI techniques in order to reduce the TDI total number of lines.

The first technique consist in varying the pitch angle of the satellite along all the ground scene that is being imaged. This is known as satellite slowdown factor. As an example the MISTIGRI satellite had a slowdown factor of 1.92 [23].

The second technique is to over-sample the scene. This is done by having a larger pixel footprint than the ground sampling distance. In order to do that the detector array must be rotated 45 deg with respect to the direction of scanning of the satellite. This concept is presented at Figure 4.7 a). After the 45 deg turn, the footprint in ground of each pixel will be two times larger than the detector without applying the rotation. Therefore there will be captured also two times more signal for each acquisition, Figure 4.7 b). The drawback is that it will be necessary to do two acquisitions in order to capture each GSD area [23]. It is therefore a very interesting technique to take into account.

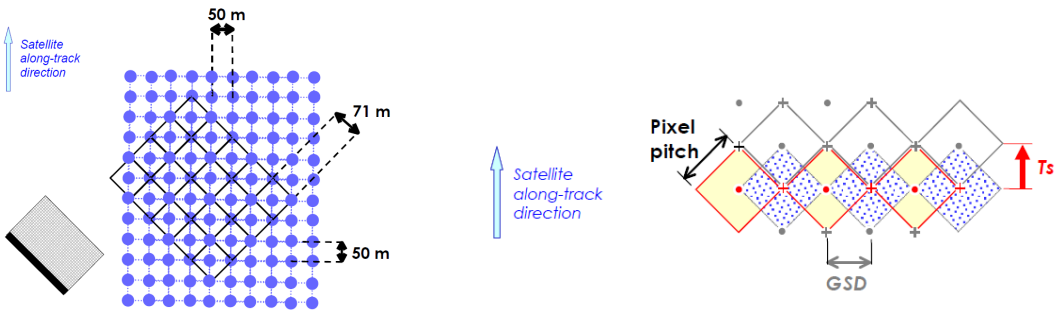

Figure 4.7: Over-sampling technique to increase the signal received from the ground, achieved by a rotation of 45 deg of the detector. [23]

As a conclusion, TDI is a solution for the long response time of microbolometers, but in the other hand it requires for a high precision optics and attitude control system. The other two techniques, the satellite pitch angle variation and the rotation of the detector 45 deg, may be used to reduce the requirements (number of rows) for the very demanding TDI technique.

4.4.10 Conclusions

The characterisation of all the time constants of an infrared detector is a process of high-complexity. In this chapter, it has been presented in a simplified way the working principle of infrared detectors.

Nowadays, the read-out process of the infrared detectors is mainly done with the CCD and CMOS read-out architecture or ROIC. While CCD read-out circuits are less noisy and less complex, CMOS ROICs are faster in the reading-out besides other properties as lower power consumption, higher responsivity, and higher radiation hardness.

The final objective for both structures is to create a thermal image. Nevertheless, as it can be assumed, the process is different for both architectures. In this chapter, it has been individually described the read-out process steps and characteristics times of each step for the CCD and CMOS technology.

CMOS technology has become a trend in infrared imaging detectors. Mainly all the new detectors available at the market are CMOS technology. CMOS detectors have been already used in space missions as it is the case of the Meteosat Third Generation of satellites. The detector for this mission was developed by the American Teledyne.

It has been also presented a solution for the large response times of thermal detectors microbolometers. These uncooled detectors were incompatible with a satellite mission since the integration time of the satellite (the time the satellites takes to pass over the target scene) was shorter than the response time of these detectors. As a result, with their use, the final image will be blurred. The solution presented is called as Time-Delay Integration TDI. The purpose is to capture the signal coming from a specific ground target several times with different pixels of the detector. This is traditionally done with CCD architectures detectors, however, new CMOS detectors allow also to do TDI. The main issue is that TDI requires high precision optics and, therefore, special caution has to be made in the optical design of the thermal imaging instrument.

The response time is one of the two main problems of microbolometers. The second one, the temperature resolution, will be covered in the next chapter and chapter 6.

Chapter 5

Temperature resolution and Signal-to-noise ratio of infrared detectors

5.1 Introduction

The description of the noise present in infrared detectors is a fundamental step for the precise determination of their performance. On one hand, this noise can arise from imperfections in the construction of the detector or appear during the read-out process as a result of a large number of microelectronic devices included. On the other hand, there are also natural sources of noise, as the noise created due to random fluctuations of the incoming flux of photons, the so-called shot noise.

The noise sources for photodetector and thermal detectors are different since their working principle is not the same. In this chapter, it will be analysed the different sources of noise for these two large groups of infrared detectors. Then, these noise figures will be used to calculate the other parameters that characterize the performance of infrared detectors. Like the noise equivalent power, NEP and the specific detectivity, D^*.

The next step in this chapter, is the analysis of the temperature resolution and SNR of the infrared detectors, not only in ground but also in the space environment. This will be very useful to know which detector fits with the requirements of the space mission.

5.2 Noise description in infrared photodetectors

The noise in photodetectors can be described in Ampere units or in Voltage units. It is possible to talk, therefore, about noise current and noise voltage. In photodetector is commonly use the definition of current noise [46]. In this section, there will be presented the three main sources of noise in photodetectors. These three main sources are the shot noise, the thermal noise and the flicker 1/f noise. These noises will be related to the previous chapter of the time constants, indicating which noise is produced in each of the steps for the read-out of the photon flux. In addition to this, it will be seen how in photodetectors the noise levels can be drastically reduced with the cooling.

5.2.1 Shot noise and Generation-Recombination noise

The shot noise is one of the three main types of noises that affects the performance of the photodetectors. In general, the shot noise is used to define the noise coming from the random fluctuations of a stream of electrons [87].

Before entering into the shot noise discussion, is important to remark that in general, the concepts of shot noise and generation-recombination (g-r) noise are utilized as if they were the same. Nevertheless, g-r noise must be applied for photoconductors, a type of photodetectors, and shot noise must be applied for photodiode photodetectors [46]. It was already discussed how photodiodes offered better performances in terms of detectivity and dark current than photoconductors for the infrared wavelengths.

Coming back to the shot noise, a general expression for its definition is presented at Equation 5.1, [46]. The units are [A].

$$i_{\mathrm{n,shot}} = \sqrt{2q\bar{i}\Delta f} \tag{5.1}$$

Where q is the electron elementary charge [C], $\bar{i}$ is the mean current [A], and Δf is the frequency bandwidth at which the detector circuits operates [Hz].

For a semiconductor structure, like the photodiodes, the shot noise main contribution is derived from the fluctuation of the number of charge carriers passing through the energy barriers of the photodiode FPA. These barriers are in non-equilibrium conditions [46]. The charge carriers were defined as the electrons that go from the valence band to the conduction band carrying the electrical current in a semiconductor. These

charge carriers are obtained after the conversion by the FPA of the incoming flux of photons into electrons.

Moreover, the incoming flux of photons is a combination of the signals coming from the ground scene and from the background that surrounds the scene. These two signals can be expressed with Equation 5.2 and Equation 5.3, [24].

$$i_{sig} = \phi_{p,sig}\eta q \tag{5.2}$$

$$i_{bkg} = \phi_{p,bkg}\eta q \tag{5.3}$$

Where $\phi_{p,sig}$, is the signal flux [photons/s], and $\phi_{p,bck}$ is the background flux [photons], η is the quantum efficiency (photons converted to electrons), and q is the electron elementary charge [C, coulombs]. The units are [A] for both equations.

As a remark, Equation 5.2 and Equation 5.3 can be also expressed as Equation 5.4 what can be useful for the radiometry budget computations [24].

$$i_{\text{ signal }} = \phi_{\text{p, sig }}\eta q = \phi_{\text{e,sig}}\eta q\frac{\lambda}{hc} \tag{5.4}$$

Where $\phi_{e,sig}$ is the signal flux in [W], λ is the wavelength of operation in [m], h is the Plancks constant [J·s] and c is the speed of light in vacuum [m/s].

In addition to the shot noise coming from the incoming flux of photons, in photodetectors, there can be considered other sources of shot noise. This is the case of the shot noise coming from the dark current of a photodiode [88]. The dark current was presented as a small electric current that remains in the detector circuits even where there are not photons entering into the detector.

Also, it has to be considered the shot noise during the circuit integration of the charge in the capacitor in CCD and CMOS read-out circuits [20].

If the previous contributions are introduced in Equation 5.1, a general expression for the shot noise can be obtained. This expression is presented in Equation 5.5. The units are [A].

$$i^2_{n_{\text{shot}}} = 4q^2 i_0^2 \Delta f + 2q^2\eta\phi_{p,sig}\Delta f + 2q^2\eta\phi_{p,bkg}\Delta f + i_{PA}2 \tag{5.5}$$

Where i_0 is the dark current [A], Δf, as cited before, is the frequency bandwidth of the detector circuits [Hz] and i_{PA} is the preamplifier noise.

The variance of the shot noise with the frequency of operation of the electronic circuits is discussed in Section 5.2.6.

As a conclusion, the shot noise cannot be reduced since it depends on the characteristics of the incoming light. The only exception in which it can be reduced is when the dark current is reduced, for example, by a larger cooling of the detector and therefore the contribution of the dark current to the shot noise is lower [88][89].

5.2.2 Dark current

It is defined as the electric current that flows through the circuits of the detector, even when there is no radiation entering into it. This parameter can be drastically reduced when the detector is cooled down. Also, this parameter can be reduced in photodetectors by the implementation of new internal architectures. This is the case of the barrier nBn/pBp photodetectors presented in Section 2.5.1.7 oriented to reduce the dark current values [56].

The dark current can be considered as a noise by itself, but also there is the cited shot noise coming from the dark current. A very important aspect to take into account is that the dark current will be smaller when the pixels of the array are smaller. Therefore the shot noise due to the dark current will be also smaller [89]. Nevertheless, it will be discussed later how for the calculation of the SNR is necessary to consider the area of the pixels and smaller pixels correspond to lower values of SNR.

5.2.3 Thermal noise or Johnson noise

It is the second main important noise to consider in photodetectors. The Johnson noise, also thermal noise, appears due to the fluctuation of the charge carriers velocity to maintain the thermal equilibrium in a semiconductor [46] [24]. In the literature is possible to find it also as Nyquist noise. It is given by Equation 5.6,[46]. The units are [A].

$$i_{n,j}^2 = 4\left(\frac{k_b T}{R}\right)\Delta f \tag{5.6}$$

Where k_b is the Boltzmann constant [J/K], T the temperature of the detector [K], Δf is the frequency bandwidth of the electronics of the detector [Hz] and R is the contribution of the semiconductor resistance and the load resistors in [ω = J/(A^2·s)].

The Johnson noise appears in three different ways. There is Johnson noise in the conversion of the photons to the electrons by the FPA sensitive part. Johnson noise in the read-out processes of the integrated circuits. And finally, Johnson noise in the reset transistor used to clean the charge remaining from the previous frame. This last contribution can be also referred individually as reset noise or KBTC noise [20] [90].

In photodetectors, the thermal noise can be drastically reduced with the cooling as it was with the dark current. This is one of the main reasons why cooler detectors offer better detectivities limits and noise figures.

As a remark, the Johnson noise must not be confounded with the temperature noise. The temperature noise is due to temperature fluctuations during the exchange of temperature between the detector sensitive part and the background. Nevertheless, this noise is negligible in cooled photodetectors, which is not the case for the thermal detector. It is detailed presented in Section 5.3.3 of thermal detectors.

5.2.4 Flicker noise 1/f

The 1/f noise appears due to a combination of stochastic fluctuations of the number of the charge carriers and fluctuations of their velocity [46]. It is related to imperfections in the material structure and the electrical contacts. As a result, it can be considered that all the electronic component of the infrared detector have a contribution into the 1/f noise. The 1/f noise is also known as flicker noise or modulation noise [24].

A very important feature is that the 1/f noise can be eliminated in photodiodes detectors by circuit engineering not allowing the bias current to flow through the diodes. It will be seen how in the case of uncooled thermal detectors this noise is always present [24]. The characterization of the flicker noise is a high complexity process. Commonly, Equation 5.7 from [24] is used for its description.

$$i_{n,f}^2 = K\frac{\overline{i}^{\alpha}\Delta f}{f^{\beta}} \tag{5.7}$$

Where K is a proportionality factor, known as the 1/f parameter, i is the average current flow through the detector [A], δf is the frequency bandwidth range of the detector circuits [Hz], α is a constant of value $\simeq 2$, and β is also a constant that ranges from $\simeq 0.5$ to 1.5 but in general it is approximately 1. f is the frequency of oscillation of the fluctuations that produce the flicker noise. Nevertheless, remark that there is not a clear definition for this f parameter in the different bibliographic sources consulted.

5.2.5 Pattern noise

This noise is coming from the non-uniformitivity in the operation of the pixels. Is a result of small mismatches between the different pixels of the FPA. For example, for the same illumination conditions, the response of some pixels will be slightly different from the response of other pixels [89][90].

Pattern noise in CMOS detectors has greater importance than in CCD detectors due to the differences in the construction [89].

5.2.6 Shot noise, Johnson noise and 1/f noise variation with the frequency bandwidth

The three main types of noises in photodetectors are dependent on the frequency bandwidth at which the electronics of the detector operates. As a result, it is possible to compare the relevance of these noises in function of the frequency. In Figure 5.1, it is represented the power spectral density (PSD) vs. the frequency of the circuits. The PSD describes the distribution of the power of the signal in function of the frequency. PSD is expressed in [W/Hz].

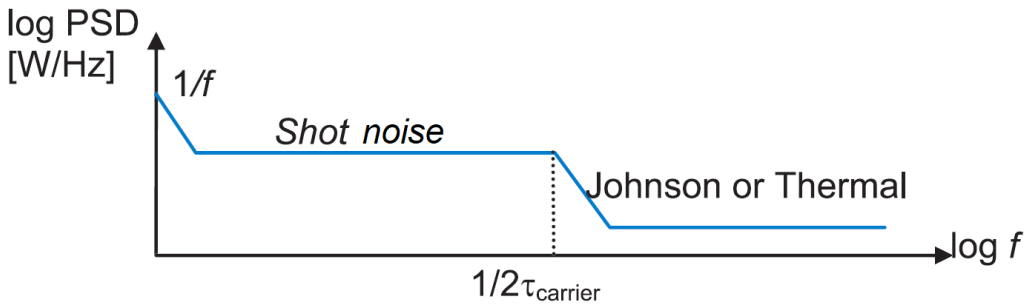

Figure 5.1: Power spectral density (PSD) of the different noise sources vs. the frequency of the detector electronics. Adapted from [24].

The flicker (1/f) noise is dominant in low frequencies, but its relevance quickly drops for higher frequencies [89].

The shot noise is dominant in the middle frequencies where it is white noise (the value does not change with the frequency). Later, it will decay in a frequency range proportional to the inverse of the carrier time. The carrier time describes the processes in which charge carriers are generated and eliminated [24].

Finally, the thermal noise is the dominant noise at high frequencies. It is white noise for all the frequencies [89].

The detector will be operated in the range of middle frequencies. Knowing that the charge carriers transport the signal and the noise, if the frequency bandwidth is increased longer than the inverse of the carrier time, there will be a higher noise but not a higher signal [24]. As a result, the detector frequency is set to this middle range.

5.2.7 Noise contributions in a photodetector

It is presented in Equation 5.8 the combination of all the noises that affect the performance of the photodiode photodetectors. This expression will be used in the noise equivalent power and SNR calculations in Section 5.6. An equivalent equation appears at reference [24]. As a remark, traditional noise calculations include the read-out noise as an additional parameter. Nevertheless, in this project, the read-out noise is divided and included in the shot noise, 1/f noise and Johnson noise as it has been described in previous subsections.

$$i_n^2 = 4q^2 i_0^2 \Delta f + 2q^2 \eta \phi_{p,sig} \Delta f + 2q^2 \eta \phi_{p,bkg} \Delta f + i_0 + i_{PA} 2 + 4 \left(\frac{k_b T}{R} \right) \Delta f + K \frac{\overline{i}^{\alpha} \Delta f}{f^{\beta}} \quad (5.8)$$

Furthermore, it is also commonly found in the bibliography the total noise of the photodetectors only as the shot noise. Considering that the other noises are sufficiently reduced due to the cooling and therefore not considered. Then, Equation 5.8 is more complete and, therefore, it will be also possible to analyse the different noise contributions at different temperatures.

5.3 Different noises in thermal detectors

The main property of thermal detectors is that they can operate at room temperatures. Nevertheless, this will be related to larger values of noise in comparison with cooled thermal detectors. In this section, there will be analysed in detail the different sources of noise of thermal detectors and in specific of the bolometers and miniaturized microbolometers. The different equations will be presented in terms of noise voltage.

In addition to this, it will be carried on a study about the effect of the cooling in a bolometer.

5.3.1 Flicker noise 1/f

The flicker noise appears due to the imperfections in the electrical contacts and the non-uniformity of the detector material. It is therefore dependent of the fabrication techniques utilised for the detector. As it was discussed in photodetectors, the measurement of this noise is a very complex process.

For state-of-the-art microbolometers, the 1/f noise is considered as the parameter that largely limits its performance, according to the references [21], [6], [91]. Flicker noise has a higher weight than the Johnson noise for the final computation of the noise in uncooled bolometers.

The value of the flicker current noise can be defined with the same expression used in photodetectors, Equation 5.7. However, in thermal detectors, the noise is commonly expressed in terms of voltage. The so-call flicker current voltage is defined in Equation 5.9, using the same parameters of the equation for photodetectos and substituting the current by a voltage, [48]. The units are [V].

$$v_{n,f}^2 = K\frac{\overline{V}^{\alpha}\Delta f}{f^{\beta}} \tag{5.9}$$

In addition to this, the flicker noise is also limiting the minimum pixel size of microbolometers. This is because the 1/f noise increases as the pixel size decrease [6].

5.3.2 Thermal noise or Johnson noise

In thermal uncooled bolometers, this noise is due to temperature fluctuations of the resistances used to measure the incoming flux of photons. This noise is dependent on the temperature of the bolometer [48] [10]. In Section 5.3.7, it will be analysed the cooling of a bolometer, with the purpose of reducing the Johnson noise.

It can be defined also with Equation 5.6 in terms of current, considering that R is now the resistance of the bolometer. On the other hand, in terms of voltage is defined according to Equation 5.10, [24]. The units are [V].

$$i_{n,j}^2 = 4\mathrm{k_B}\mathrm{TR}\Delta f \tag{5.10}$$

Where k_b is the Boltzmann constant [J/K], T the temperature of the detector [K], Δf is the electrical bandwidth [Hz] and R is the resistance of the bolometer. [ω = J/($\mathrm{A}^2\cdot$s)].

5.3.3 Temperature noise and radiative thermal exchange noise

Temperature noise is due to temperature fluctuations in the detector. From one side, these fluctuations are coming from variations in the rate at which heat is transferred between the detector sensitive element and the surrounding substrate in contact with it. From the other side, fluctuations in the radiative heat exchange between the detector and the background at different temperature [24]. This last contribution can be found in the bibliography as a radiative thermal exchange noise. Moreover, temperature noise is also known as phonon noise. It is important not to confuse the temperature noise with the thermal/Johnson noise.

The fluctuations in the temperature can be expressed with Equation 5.11, [24] [10].

$$\overline{\Delta T^2} = \frac{4k_b K T^2 \Delta f}{K^2 + (2\pi f)^2 C^2} \tag{5.11}$$

Where k_b is the Boltzmanns constant [J/K], K is the thermal conductance [W/(m*K)], C is the heat capacity [J/K], T is the temperature of the detector [K], f is the unit of bandwidth [Hz], and δf is the frequency bandwidth [Hz]. The 2π comes because this noise is given for a 2π field of view.

It can be used the equation of reference [91] to describe the temperature noise in [V]. This equation has not been included since it depends on a large number of parameters defined in the reference.

Ideally, thermal detectors are temperature noise limited instead of Johnson noise limited. It will be later discussed, as it will be done for the Johnson noise, the effects of cooling a bolometer into the temperature noise.

5.3.4 Read-out noise

The read-out circuits of thermal detectors, like it could be the CCD or CMOS ROIC of a microbolometer, are also a source of noise. The resistances used within these ROICs are producing Johnson noise. Moreover, the capacitors and amplifiers have considerable importance in the generation of flicker noise. Also, it can be considered the noise contribution of the analogue to digital converters used in bolometers [20].

5.3.5 Noise contributions in thermal detectors

The different sources of noise in thermal detectors are grouped in Equation 5.12, the units are [V]. This expression will be used in the definition of the noise equivalent

power as discussed in the photodetectors noise analysis.

$$V_n^2 = K\frac{\overline{V}^{\alpha}\Delta f}{f^{\beta}} + 4\mathrm{k_B}\mathrm{TR}\Delta f + RO_n^2 + T_n \tag{5.12}$$

Where RO_n is the read-out noise and T_n is the temperature noise. It is split from the other source of noises according to the common methodology followed by the bibliography.

5.3.6 Noise model of bolometer uncooled thermal detectors

The characterization of the noise in bolometers is a complex process due to a large number of parameters involved. For example, the total Johnson noise (read-out noise included) depends on the resistance of the bolometer sensitive part, the resistances of the ROIC, the frequency of operation of the detector circuits and the temperature of the detector. For the thermal noise, it is needed the responsivity of the detector, the thermal conductance and thermal capacity of the bolometer and the frequency among others as the temperature of the detector and the absorption of the bolometer membrane.

Therefore, there is not any manufacturer that provides with all this information to detailed compute the noise of a specific detector. It can be compared the total noise but not each of its components individually. As a result, a research was done with the aim of finding a project that could provide with all the parameters that determine a bolometer. Among the different papers published, the reference *Uncooled Infrared Bolometer Arrays Operating in a Low to Medium Vacuum Atmosphere: Performance Model and Tradeoffs, [91]* was considered as the most accurate model.

This article individually analyses the contributions of the four main noises of a bolometer thermal detector. The noises are computed with Voltage units. The sum of these four contributions is equal to the total current voltage. Now, this voltage can be substituted into the theoretical equation of the noise equivalent temperature difference (NETD), which is also used in Section 5.5.2. The NETD or temperature resolution is the minimum change in the temperature of the target that can be measured by the detector.

Then, in this article it is also determined the NETD in [mK] that corresponds to each noise. The sum of all the contributions is equal to the total NETD. With the equations and parameters of this article, there were computed the values of Table

5.3.6. The computed values for the NETD were checked with the values presented in the document.

Noise	Value	Unit	NETD	Value	Unit
$v_{1/f}$	3,753	V	$NETD_{1/f}$	0,026	K
$v_{johnson}$	1,245	V	$NETD_{johnson}$	0,008	K
$v_{thermal}$	1,011	V	$NETD_{thermal}$	0,007	K
v_{roic}	1,434	V	$NETD_{roic}$	0,010	K
v_n	4,325e^{-6}	V	-	-	-
NETD	0,029	K	NETD	0,029	K

Table 5.1: Contribution of each source of noise to the noise equivalent power (NETD).

The importance of Table 5.3.6 is that it confirms that the largest noise of bolometers is the 1/f (flicker) noise. As a remark, the detector is a 640x480 pixels, 28 μm pixel pitch, and 11.7 ms thermal time constant (time for 63% of the final output voltage) VO_x bolometer. In addition to this, all the calculations were done with the bolometer at 300 K, room temperature.

5.3.7 Cooling down a microbolometer

One of the main questions that emerged during the development of this project is what will happen if we cool down a microbolometer. Looking at the bibliography there are examples of semiconductor bolometers and high-temperature superconducting bolometers operating at temperatures lower than 100 K, [6]. These two types of bolometers were presented in Section 2.5.2.1, as the promising future thermal detectors. On the other hand, there are no references about the operation of a VO_x or a-Si, microbolometer at temperatures lower than room temperature (around 300 K).

Looking back to the discussion of the previous section, it was seen how the main noise in state-of-the-art VO_x bolometers, is the flicker noise. The 1/f noise does not depend on the temperature of the microbolometer FPA. However, the Johnson noise and temperature noise depend on the temperature of the FPA.

The objective is to change the temperature of the FPA in the noise model of the previous section from 300 K to 200 K. This 100 K difference may be obtained by using passive cooling instead of using a cooler. The results obtained after the reduction of the temperature are illustrated in Table 5.3.7.

It can be seen how the values of NETD decreased from 29.49 mK to 28.63 mK. That represents a very small reduction in the noise for a very big change in the temperature

Noise	Value	Unit	NETD	Value	Unit
$v_{1/f}$	3,753	V	$NETD_{1/f}$	0,026	K
$V_{johnson}$	1,017	V	$NETD_{johnson}$	0,007	K
$V_{thermal}$	0,674	V	$NETD_{thermal}$	0,005	K
V_{roic}	1,434	V	$NETD_{roic}$	0,010	K
V_n	$4{,}198e^{-6}$	V	-	-	-
NETD	0,028	K	NETD	0,028	K

Table 5.2: Results obtained after cooling down to 200 K a microbolometer.

of the detector. As a conclusion, there is no reason to cold down a microbolometer. The main noise is the 1/f noise and it cannot be reduced by the temperature.

In addition to this, it is important to maintain the microbolometer at a constant temperature. This is done by the use of a thermo-electrical cooler (TEC), which was already introduced at Section 2.5.2.4. Using a TEC, the microbolometer will be always measuring the change in temperature of the signal captured without be influenced by fluctuations of the thermal detector itself. However new microbolometers as the 'Bird 17 μm ceramic packing' from SCD,[5], or the 'Pico-1024' and the 'Pico-640' from the French manufacturer ULIS,[11], are TEC-less compatible and they also have a global electrical shutter (shutter-less).

5.4 Noise figures of merit

5.4.1 Noise Equivalent Power (NEP)

It is one of the main figures of merit of infrared detectors. It is used to describe the sensitivity of the sensor and to calculate the signal to noise ratio. It can be understood as the amount of absorbed power in the detector that generates on it an output signal equal to the detector noise. It is defined for the unit of frequency. Therefore, in other words, the NEP is the quantity of incident light absorbed by the detector that results in a signal-to-noise-ratio SNR equal to 1 for a given output bandwidth in Hz [92].

This parameter complements the responsivity parameter providing with the minimum detectable incoming flux. It is defined for cooled and uncooled detectors.

In addition to this, the NEP is commonly expressed as the ratio between the noise and the responsivity. This definition is presented in Equation 5.13, [24]. A smaller NEP indicates better sensitivity and lower noise in the output signal. The units of NEP are $W/Hz^{1/2}$.

$$NEP = \frac{i_n}{R_I \cdot \sqrt{\Delta f}} = \frac{v_n}{R_V \cdot \sqrt{\Delta f}} \tag{5.13}$$

Where i_n is the noise current [A], R_I is the current responsivity [A/W], v_n is the noise voltage [A], R_v is the voltage responsivity [V/W] and Δf is the electrical frequency bandwidth [Hz]. The value of the v_n is the total noise obtained for photodetectors and thermal detectors, Section 5.2.7 and 5.3.5 respectively.

A very relevant feature is the definition of the electrical frequency bandwidth. As explained in the previous chapter, there is not a common definition for all the times that characterize an infrared detector. After comparing different bibliographic sources, it was considered the definition of references [93] [6] [94] [48], for the electrical frequency bandwidth. Where it is defined the electrical frequency bandwidth Δf, according to Equation 5.14.

$$\Delta f = \frac{1}{2\Delta t} \tag{5.14}$$

Δt is defined by the bibliography as the 'bias pulse duration', as an integration time or as the noise bandwidth of the read-out circuits. At Section 4.4.4, it was explained how the integration time of the circuits (independent of the exposure time of the pixels), is the time in which the charge is integrated in the capacitor during the read-out. Moreover, in all the noises described in previous sections, it was present the frequency bandwidth Δf of the circuits. Therefore, this frequency bandwidth of the circuits will be calculated with Equation 5.14, once it is known the integration time of the circuits.

The order of magnitude of the integration time of the circuits varies between the microseconds to the milliseconds. Moreover, the integration time of the circuits can be longer than the exposure time of the pixels (time the pixels are capturing the incoming radiation) but usually the bibliographic references do not make a distinction between then. For example in the data sheet of the 'Neutrino SWaP+C Series' T2SL infrared detector from FLIR [38], it is indicated that the integration time of the circuits is programmable between 100 μs to 16 ms.

After that, it was also discussed how the exposure time of the pixels is lower than the frame rate of the detector. For example, in photographic cameras for ground applications, the exposure time is in the order of the half on the frame rate [95]. If, for example, the frame rate is 60 Hz, the corresponding time is a picture each 16.6

ms, (1/60 Hz), and the exposure time of the pixels will be 8.3 ms. However, it does not need to be considered always half of the frame rate, varying with respect to the application.

As a result, in order to calculate the SNR from the NEP, it will be necessary to consider the time constants of the circuits of the detector.

For example, in several of the SCD infrared detectors is cited that the NETD is measured at a frame rate of 30 Hz. From this 30 Hz it can be derived the integration time of the circuits.

Coming back to the NEP, it can be related to the SNR with the use of the Equation 5.15. This expression is obtained by introducing the responsivity equation (output voltage divided by incoming power),Equation 2.6, into the previous definition of the NEP.

$$NEP = \frac{v_n}{R_V \cdot \sqrt{HZ}} = \frac{i_n}{R_I \cdot \sqrt{Hz}} = \frac{v_n}{\frac{V}{P \cdot A} \cdot \sqrt{Hz}} = \frac{P \cdot A \cdot v_n}{I \cdot \sqrt{Hz}} = \frac{P \cdot A}{\frac{I}{in} \cdot \sqrt{Hz}} = \frac{P \cdot A}{SNR \cdot \sqrt{Hz}} \tag{5.15}$$

Knowing that V is the output voltage in [V], P is the incident power per unit of area [W/m^2] and A is the detector pixel active area [m^2].

Therefore, it is clear that the NEP varies with the frequency. In addition to this, the NEP value is dependant of the infrared wavelength range. This is because the NEP is defined in terms of the responsivity which varies with the wavelength. The minimum value of NEP is reached at the wavelength where the detector responsivity is maximum. If the value of NEP is known in a specific wavelength, to calculate the minimum NEP, it can be used the expression of the Equation 5.16, [94].

$$NEP(\lambda) = NEP_{\min} \times \frac{R_{\max}}{R(\lambda)} \tag{5.16}$$

This discussion can be clarified with one example. Supposing an infrared detector with a NEP value of 10^{-9} W/Hz$^{1/2}$ operating with an electrical frequency bandwidth of 1Hz. That means that the sensor can detect a signal power of one nanowatt with an SNR equal to 1 after an integration time of 0.5 seconds.

5.4.2 Specific Detectivity, D*

This parameter was already defined in the main figures of merit of infrared detectors. It has a higher relevance than the NEP. The NEP was just defined with the unit

of frequency. What allows the specific detectivity, D*, is to compare the different detectors depending not only in the frequency but also in the active area of the pixels. As it can be assumed, it can be also used to compare detectors of the same material and different pixel areas. For understanding purposes, Equation 2.11 has been recovered in Equation 5.17. The specific detectivity is defined in units of [cm·Hz$^{1/2}$/W], also called Jones [24].

$$D^* = \frac{\sqrt{A\Delta f}}{\text{NEP}} = \frac{(A_d \Delta f)^{1/2}}{v_n} R_v = \frac{(A_d \Delta f)^{1/2}}{i_n} R_i = \frac{(A_d * \Delta f)^{1/2}}{P} * (SNR) \tag{5.17}$$

On it, Δf is the electrical bandwidth of the circuits of the detector. All the conclusions reached in the NEP parameter about the time constants are also used in the specific detectivity.

Moreover, it was presented the conclusion achieved in determining that the value of the specific detectivity does not vary with the altitude. It is only dependant on the frequency bandwidth of the electronics, the infrared wavelength range and the active area of the pixels.

5.4.3 Minimum Resolvable Temperature Difference (MRTD)

The MRTD is a parameter used to measure the performance of an infrared imager system, more than specifically the detector.

It defines the probability of detection and recognition of low contrast details in a target. Four white bars in the ground form the target. The purpose of the MRTD is to specify the minimum temperature difference between the bars and the background to detect the bars [40].

This parameter is defined with the angular spatial frequency, f$_s$, and the NETD, besides other parameters as the system modulation transfer function (MTF) to which it is inversely proportional. Therefore, while the NETD defines only the temperature resolution, the MRTD combines the temperature resolution with the target spatial details. An expression for the MRDT is presented in Equation 5.18, [6]. The units are [K].

$$\text{MRTD}\,(f_s) = K\,(f_s)\,\frac{\text{NETD}}{\text{MTF}\,(f_s)} \tag{5.18}$$

Where K(f_s) is a function containing elements as the target signal-to-noise-ratio, the detector subtenses angles, the frame rate, the characteristics of the scanning procedure and the angular spatial frequency, f_s. The process to obtain this function K is of very high complexity [6][48].

Moreover, it is important not to confuse the concept of angular spatial frequency, f_s, and spatial frequency, f. The former is calculated as the distance from the target to the thermal imaging system, in meters, divided by the spatial period, in meters also, between the centers of the 4-bars. It is expressed in [cycles/rad] [96]. On the other hand, the spatial frequency is defined as the inverse of the spatial period between the bars. The units are [cycles/m], and it is the one used for the determination of the MTF.

The MTF defines the ability of a lens to transfer contrast with a specific resolution from the object to the image. The resolution can be understood as the ability of an imaging system to distinguish details in the objects. On the other hand, the contrast defines how the different minimum and maximum intensities values of the object plane are transferred from the object plane to the image plane [97].

The MRTD will not be considered for the comparison of the different detectors in this project. However, this parameter must be taken into account for future analysis of the optical system.

5.5 Temperature resolution. Noise Equivalent Temperature Difference (NETD)

The NETD is defined as the minimum temperature change of the target, in Kelvin, that can be detected by the optical instrument. In other words, the NETD defines the minimum temperature change that will produce an output signal in the detector of the same value as its total voltage/current noise. The NETD describes the temperature resolution of the detector [40].

It is possible to find several references in the bibliography describing the calculation of the NETD. However, not all the models considered the same parameters for the determination of the NETD. This figure is usually computed by an experimental method instead of a theoretical determination.

The NETD is a parameter provided by mostly all infrared detector manufacturers. One of the main objectives of this project was to understand with deep detail the

NETD to possibly compute the temperature resolution of the imager in space. This is the minimum detectable change in temperature in the agricultural crops that can be detected. For agricultural monitoring, the optical system needs to detect changes in temperature of at least 0.5 K,[98], as it will be discussed in Chapter 7. Next, it will be explained how the NETD is measured in the ground and then how it is computed in space.

5.5.1 NETD measurement in ground

The first step was to be sure of how the NETD is calculated in a laboratory in the ground. There were several references in the bibliography about how this measurement is carried on. However, since this parameter has critical importance, it was decided to directly get in touch with the manufacturers. There were responses by the French Sofradir [99], the American FLIR [38] and the Chinese Hope-Wish Technologies Inc [25]. Sofradir and FLIR are well-known manufacturers of infrared detectors for ground and space mission. Sofradir develops photodetectors and FLIR mostly also photodetectors but also thermal detectors as the microbolometer incorporated in the camera 'TAU-2'. On the other hand, Hope-Wish Technologies develops infrared thermal cameras for ground applications. The contact with Hope-Wish was very useful to certify that the NETD is measured with the same procedure by the different manufacturers.

To measure the NETD, first, the detector is pointed to a black body at a temperature. There are no optical devices in front of the detector. The distance to the black body is set between 2 cm to 5 cm (FLIR procedure). The exposure time of the detector is set to halfway its dynamic range. The dynamic range is the maximum number of photons until the saturation of the detector. Then, the black body is set to a temperature of usually 298 K. In the words of Hope-Wish Technology, the blackbody has to stabilize before starting with the measurements. The radiation received by the black body corresponds to the wavelength range to which the detector material is sensitive.

Starting with the measurement is important to have in mind that the NETD is not measured for an exact instant. The NETD is a temporal noise and therefore it is measured in an interval of time and in several frames.

After the measurement, a histogram of all the pixel values is obtained. This histogram appears in Figure 5.2. As a remark, this Figure was provided by Hope-Wish Technologies but it can be found also in the reference [26].

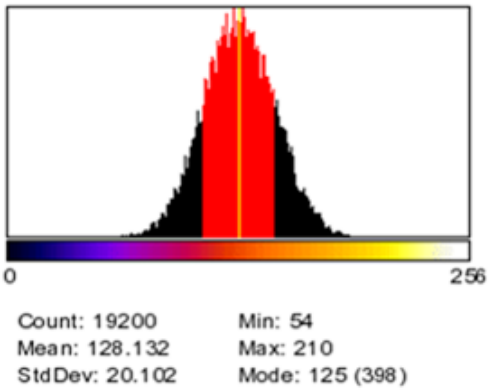

Figure 5.2: Histogram of all the values of the pixels obtained during the NETD measurement. [25][26]

Finally, the NETD value is defined through the standard deviation of the histogram which is converted to mK. In Figure 5.3, it is illustrated the differences in temperature resolution between two cameras with different NETD.

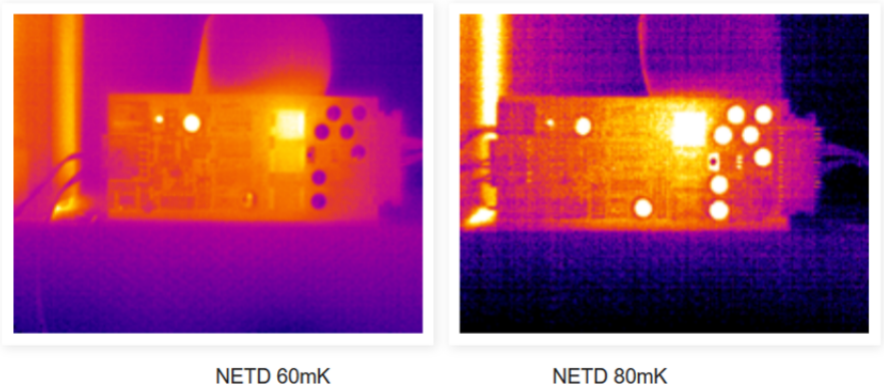

Figure 5.3: Difference in temperature resolution of two cameras with different NETD pointing at the same scene.[26]

A very important point that has not been yet commented, is that the NETD depends on the F-number. The F-number is traditionally defined as the ratio between the diameter of the pupil and the focal length. However, no lens are used in the determination of the F-number. The NETD of the datasheets is given not only for a specific temperature and frame rate but also for a specific F-number. In photodetectors, a specific F-number can be set by modifying the aperture of the cold shield located inside the dewar which also contains the filters and FPA of the detector (discussed in Figure 2.11). For example, in the data sheet of the HgCdTe photodetector 'HiPIR

Engine HOT' from the German AIM, it is indicated a NETD of 25 mK for a cold shield F-number of F/2.2.

In the case of thermal uncooled detectors, since there is no lens and no dewar, all the computations that have been found in the manufacturers are expressed for an equivalent F-number of 1. For example, the 'Ceramic 640' microbolometer from SCD indicates a NETD of 35 mK measured with a 298 K black body, 60 Hz frame rate and an F-number of F/1 [5].

To be sure that the NETD for thermal detectors and photodetector is calculated in the same way, new conversations were made with FLIR. The engineer from FLIR that helped us was Christel Roderick. The answer received is next cited: *Fundamentally, the NETD is measured the same way for both types of cameras. The cooled cameras must be measured at mid-scale, and this is not required for bolometers.*

In a second conversation, he confirmed how the NETD of the 'Neutrino SWaP-C' infrared photodetector is 25 mK for a cold shield F-number of F/5.5 [38]. Then in order to compare it with a thermal detector of F/1, it is necessary to normalize the NETD to F/1. This is done by Equation 5.19.

$$\mathrm{NETD_{F/1}} = (1.0 \div \mathrm{X})^2 \times \mathrm{Y} \tag{5.19}$$

Where X is the cold shield F-number and Y is the NETD for the X F-number.

For example, for the Neutrino detector F/5.5 and NETD 25 mK, using Equation 2.4 it is obtained a $\mathrm{NETD}_{F/1}$ of 0.8 mK. As a remark, this detector from FLIR is the most advanced photodetector found during this project in 2019. For the AIM F/2.2 and NETD 25 mK, the normalized NETD is 5.2 mK what is a more common value for photodetectors.

Therefore it can be seen how the NETD of photodetectors is several times better than the NETD for thermal detectors, usually between 35 mK and 50 mK.

5.5.2 Noise Equivalent Temperature Difference, NETD, theoretical model

For the theoretical calculation of the NETD, it will be used the expression of Equation 5.20. This formula has been check with several bibliographic references, [91], [6], [100] [93]. There are other very interesting models, like the one presented in reference [101] that considers a higher number of parameters in the determination of the NETD.

However, the Equation 5.20 was used to avoid as much as possible assumptions in the value of these parameters. The units are [K].

$$NETD = \frac{4 \cdot F^2}{D \cdot A \cdot \phi_{\lambda 1-\lambda 2} \cdot \pi \cdot \left(\frac{dP}{dT}\right)_{\lambda 1-\lambda 2}} \tag{5.20}$$

Where F is the F-number of the cold shield, A is the active area of the pixel [m^2], ϕ is the transmission of the filter located before the FPA sensitive part of the detector, $\frac{dP}{dT}$ is the radiant power of the black body in a specific temperature, and in a specific wavelength, the units are [$W/(m^2 \cdot K \cdot sr)$]; D, is the detectivity of the detector [W^{-1}].

It is important not to confuse the specific detectivity, D^*, in [$m \cdot Hz^{1/2}/W$] with the detectivity D in [W^{-1}]. Also not to confuse it with the NEP which has units of [$W/Hz^{1/2}$]. The detectivity D, cannot be used to compare different detectors, in contrast with the specific detectivity D^* defined per unit of frequency and area. The advantage of using the detectivity, D, is that it will be not necessary to make assumptions in the value of the electrical bandwidth. The value of the detectivity does not change with the altitude.

Another equivalent expression that can be used for the determination of the NETD is presented in Equation 5.21, [100].

$$NETD = \frac{4 \cdot F^2 \cdot v_N}{R \cdot A \cdot \phi_{\lambda 1-\lambda 2} \cdot \pi \cdot \left(\frac{dP}{dT}\right)_{\lambda 1-\lambda 2}} \tag{5.21}$$

Where v_n is the noise voltage [V], and R is the responsivity of the detector [V/W].

In the manufacturers data sheets, it will appear the NETD measured in the ground and the conditions of the measurement, usually 300 K black body and between 30 Hz and 60 Hz frame rate; the F-number used in the measurements; the pixel pitch of the pixel; and usually the fill factor (percentage of the pixel surface sensitive to the incoming radiation).

The noise voltage v_n is not usually given but it can be calculated. For example, in all the data sheets of the SCD microbolometers appears the so-call typical response in [V/K]. With the NETD and Equation 5.22,[35], it can be calculated the noise voltage, v_n.

$$NETD[mK] = \frac{v_{\text{noise}}[\mu V]}{\text{R}[mV/K]} \tag{5.22}$$

Finally, $\frac{dP}{dT}$ represents the radiant power of the black body derived in function of its temperature. It can be followed a simple procedure for its calculation. First, the

radiance of a black body at a specific temperature is calculated with Planck's law. It will be necessary to integrate the Plank equation in the wavelength range at which the detector operates. But this wavelength range is provided by the manufacturer. For example, the NETD of the microbolometer 'Ceramic Bird 640-HS' from SCD, has been measured in an interval from 8 μm to 14 μm as indicated in the data sheet [5]. Therefore, the Plancks law has to be integrated between 8 μm to 14 μm. This is a fixed parameter. In other words, it must be used the same values that the manufacturers utilized in the calculations. Before the integration of the radiance, it is necessary to derive the Planck's law in function of the temperature of the black body. Then, this derivate is the one finally integrated between 8 μm to 14 μm, [6] [93].

The final expression appears in Equation 5.24, while Equation 5.23 is the Planck's law. The units of the Plack's law are W/(sr$\cdot$ m^3). The units of the $\frac{dP}{dT}$ expresion are [W/(m$^2\cdot$K $\cdot$ sr)].

$$L(\lambda, T) = \frac{2hc^2}{\lambda^5 \left(\frac{hc}{e^{\lambda k T}} - 1\right)} \tag{5.23}$$

$$\frac{dP}{dT} = \int_{\lambda_a}^{\lambda_b} \frac{\partial M(\lambda)}{\partial T} d\lambda \tag{5.24}$$

Where h is the Plancks constant in [J $\cdot$ s], k is the Boltzmanns constant in [J/K], c is the velocity of the light in vacuum [m/s], λ is the wavelength in [m] and T is the temperature of the target in [K].

For example, in the range between 8 μm to 14 μm, and temperature of the black body of 300 K, the value of $\frac{dP}{dT}$ is 0.828 W/(m$^2\cdot$K $\cdot$ sr). The values included in the table of Figure 5.4 represent the product of $\frac{dP}{dT}$ times π for different wavelengths ranges and temperatures of the black body. The π is coming from the definition of the solid angle (π/4$\cdot$F^2), included in the two NETD equations presented. The solid angle is defined in Section 5.6. This Table has been extracted from a book available at the library at the CSL, [27], and is also available at reference [6]. All the values has been check with the model of Equation. 5.24.

After this discussion, in the Equation 5.20, there is only the unknown of the detectivity, D, in [W]; and in the Equation 5.21, there is only the unknown of the responsivity, R, in [V/W]. For a complete comprehension, two examples are next included.

First, the SCD, 'Bird 384' VO_x microbolometer 384x288 pixels. With a NETD of 50 mK, measured in the range from 8 μm to 14 μm, temperature of the black body

λ_a μm	λ_b	$T = 280$ K	$T = 290$ K	$T = 300$ K	$T = 310$ K
3	5	1.1×10^{-5}	1.54×10^{-5}	2.1×10^{-5}	2.81×10^{-5}
3	5.5	2.01×10^{-5}	2.73×10^{-5}	3.62×10^{-5}	4.72×10^{-5}
3.5	5	1.06×10^{-5}	1.47×10^{-5}	2.0×10^{-5}	2.65×10^{-5}
3.5	5.5	1.97×10^{-5}	2.66×10^{-5}	3.52×10^{-5}	4.57×10^{-5}
4	5	9.18×10^{-6}	1.26×10^{-5}	1.69×10^{-5}	2.23×10^{-5}
4	5.5	1.83×10^{-5}	2.45×10^{-5}	3.22×10^{-5}	4.14×10^{-5}
8	10	8.47×10^{-5}	9.65×10^{-5}	1.09×10^{-4}	1.21×10^{-4}
8	12	1.54×10^{-4}	1.77×10^{-4}	1.97×10^{-4}	2.17×10^{-4}
8	14	2.15×10^{-4}	2.38×10^{-4}	2.62×10^{-4}	2.86×10^{-4}
10	12	7.34×10^{-5}	8.08×10^{-5}	8.81×10^{-5}	9.55×10^{-5}
10	14	1.3×10^{-4}	1.42×10^{-4}	1.53×10^{-4}	1.65×10^{-4}
12	14	5.67×10^{-5}	6.1×10^{-5}	6.52×10^{-5}	6.92×10^{-5}

Figure 5.4: Incoming power received by a black body at different temperatures in different wavelength ranges. The measurement are done in ground with units of W/(cm^2·K)[27]

300 K and F-number of the cold shield equal to F/1. The pixel pitch is 25 μm and the fill factor is 75 % [5]. The transmittance of the microbolometer high-pass filter (to limit it for the LWIR range) has been considered to be 0.9.

The computed value of D is 9.6 $\cdot 10^{10}$ W^{-1}. This value was checked with the reference [28]. This reference is a real NETD model developed by the engineering company SENER, for the study of the microbolometers of JEM-EUSO instrument of the International Space Station. The equations are not provided, but in contrast, the final results are. The value of D, for this microbolometer by the SENER model, is 1,03$\cdot 10^{11}$ W^{-1}. There is just a slight difference in the values that can be arising from a small difference in one of the parameters considered, like for example the exact value of 50 mK NETD. To be sure, the equation was used with several other microbolometers obtaining similar values from the model of the OUFTI-CubeSat and the SENER model.

A second example, the HgCdTe photodetector 'HiPIR Engine HOT' from the German AIM [37]. It is indicated a NETD of 25 mK measured in the range from 3.4 μm to 4.8 μm, the temperature of the black body 300 K and F-number of the cold shield of F/2.2. The detector is 1024x768 pixels and 10 μm pixel pitch. The fill factor is assumed to be 75 %. Substituting this values into Equation 5.20 it is obtained a detectivity, D, of 9.7 $\cdot 10^{13}$ W^{-1}. The product $\frac{dP}{dT} \cdot \pi$ for the 3.4 μm to 4.8 μm range is 0.049 W/(m^2·K).

5.5.3 NETD measurement in space

Once it has been certified with the reference that the model considered in the ground is correct, the next step will be to apply the Equation 5.20 or Equation 5.21, but this time with the optical parameters of the satellite in space. The values that do not change with the altitude are the responsivity, R, the detectivity D, and the pixel size characteristics. These assumptions were done according to the theory. Nevertheless, in order to be sure in this critical step, it was contacted the manufacturer Sofradir from France which has a large heritage of infrared photodetectors in Space [99].

The answer received by Mr Jean-Baptiste Bel from Sofradir is next cited: *Through several qualifications performed we do not have significant evolution of the Dark current or noise hence no evolution of the NETD in Space compare to on the ground.*

Coming back to the NETD equation, the parameters used in space are next defined. Starting with the F-number of the cold shield, which now is the F-number of the optical systems (diameter of the pupil divided by the focal length). Then the $\frac{dP}{dT}$ W/(m^2·K · sr) is set to be in the range of operation of the optical system. For example, if the detector was tested in the ground between 8 μm to 14 μm, now in the formula in space, it can be set an $\frac{dP}{dT}$ from 8 μm to 10 μm, or 10 μm to 12 μm, or 9.5 μm to 11 μm, etc. But this range must be between 8 μm to 14 μm the wavelengths tested in the ground if not the detectivity D calculated will be not correct considered.

Finally, the filter transmission is also considered but now is necessary to take into account three new parameters. The transmission of the optics; the transmission of the atmosphere in the wavelength range selected; and the ground emissivity since the Earth is not a perfect black body. For the emissivity of the Earth, it can be considered a value of 0.97 in the MWIR and 0.997 for the LWIR [102]. The final expression for the NETD in space appears in Equation 5.25.

$$NETD = \frac{4 \cdot F^2}{D \cdot A \cdot \phi_{\lambda 1-\lambda 2} \cdot \varphi_{\lambda 1-\lambda 2} \cdot \delta_{\lambda 1-\lambda 2} \cdot \tau_{\lambda 1-\lambda 2} \cdot \pi \cdot \left(\frac{dP}{dT}\right)_{\lambda 1-\lambda 2}} \tag{5.25}$$

Where φ is the emissivity of the Earth, δ is the transmission of the optics and τ is the atmosphere transmittance.

Continuing with the example of the SCD, 'Bird 384', with a NETD in the ground of 50 mK. In the JEM-EUSO model, it is plotted the variation of the NETD for this detector in the wavelength ranges 10 μm to 12 μm, 10 μm to 11 μm and 11 μm to 12 μm, [28]. In order to check the OUFTI model, the same wavelength ranges

were selected. The results obtained appear in Figure 5.5 b). At Figure 5.5 a) it is represented the JEM-EUSO model.

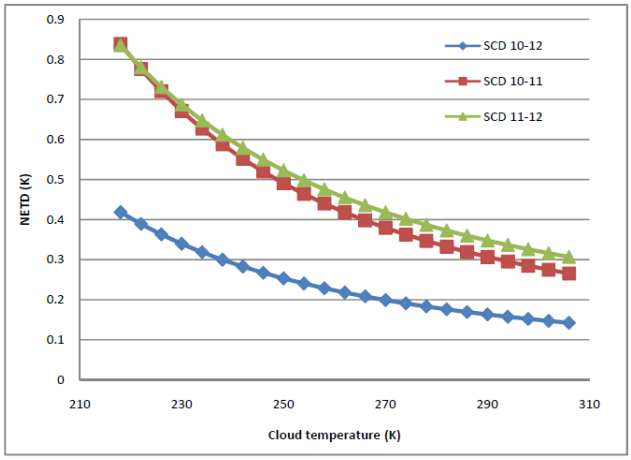

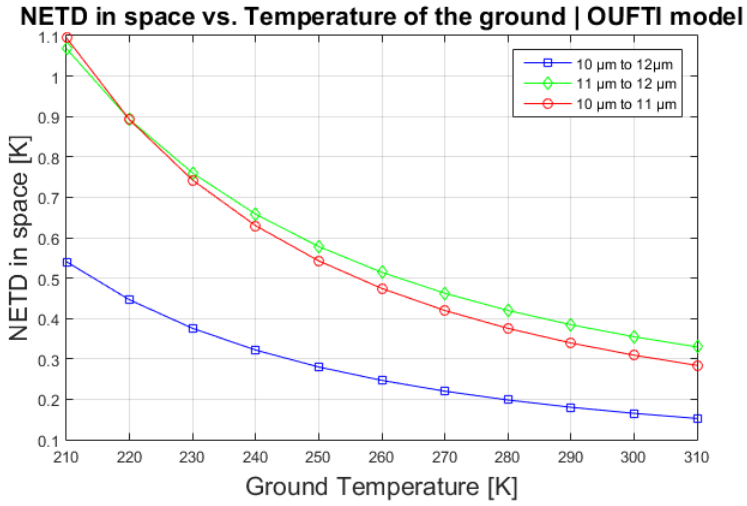

Figure 5.5: NETD vs. Temperature of the ground for the SCD 'Bird384' microbolometer a) Model developed to the JEM-EUSO instrument by SENER Engineering [28], b) Model developed for the OUFTI CubeSat.

This model was tested with the other microbolometer detectors analysed by SENER in the JEM-EUSO instrument. For all of them, the results were very satisfactory as it was with the 'Bird 384'.

This allows concluding that a correct model for the measurement of the temperature resolution in space has been achieved. This was one of the main objectives of the project.

This model will be used in the chapter 7 of this project to compare the different detectors. Also, it will be presented there the requisites in term of temperature

resolution for a space mission to possibly select the correct detector.

5.5.4 NETD for different optical instruments

After the previous discussion, it could emerge the idea that for larger optical instruments the degradation of the NETD in space will be lower. In other words, if the diameter of the pupil is larger, the signal captured is also larger, and since the NETD depends on the radiation received, it will be lower affected. Nevertheless, this assumption cannot be considered as correct.

For example, lets assume that the same detector is used in two optical systems that have the same F-number, but one of them is much larger in terms of diameter and focal length than the other. The two optical systems are proportional and because of that, the F-number is equal for both. Even if the larger one is capturing more radiation, the NETD in space will be equal to the small optical instrument. This is possible because of Equation 5.26 which has to be fulfilled. If the same F-number and the same pixel size (same detector) is used, and one of them has a larger pupil diameter than the other, it must be necessary to change either the ground sampling distance, GSD, or the altitude of the satellite, h. For a higher diameter of the pupil, the GSD will be smaller if the same altitude is maintained. As a result, the radiation received by both optical instruments is going to be the same. The NETD will be the same. Other parameters like the airy disk, 2.44 · F-number · wavelength, will be the same for both optical systems. It has been included in Figure 5.6 a schematic drawing of the elements involved in the formula for an easier comprehension.

$$iFOV = \frac{GSD}{h} = \frac{\text{Pixel-size}}{F \cdot \text{ Diameter-pupil}} \tag{5.26}$$

5.6 Signal-to-noise ratio (SNR)

The signal-to-noise ratio is one of the main fundamental figures that characterize the performance of an optical system. It is defined as the ratio between the signal coming from the target that reaches the detector and the total noise of the detector. The total noise has been already described for photodetectors and thermal detectors in Section 5.2.7 , and in Section 5.3.5, respectively, in [A] units or [V] units.

The signal, is the power in [W] received from the target. The detector is characterised by a responsivity defined as the output voltage/current per unit of received

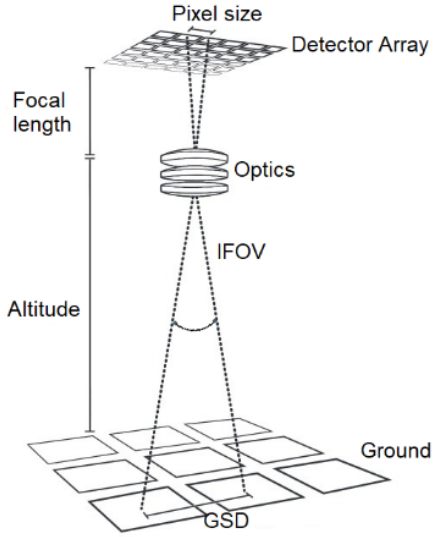

Figure 5.6: Geometrical description of an infrared imager system. Adapted from [29]

power in [A/W] or [V/W] respectively. This responsivity has to be multiplied by the incoming power in [W]. Therefore, the final signal used in the computation of the SNR is the output voltage or output current. This principle is described in Equation 5.27, adpated from [24]. The SNR is an adimensional parameter.

$$SNR = \frac{P \cdot R}{v_n} \tag{5.27}$$

The value of P, the incoming power in [W], is calculated using Plancks law for the radiation of a black body. Before the integration of this equation over the desired wavelength range, it is multiplied by the etendue of the optics. The etendue is the product of the pixel active area times the solid angle of the optics. The solid angle, in steradian [sr], describes the cone of radiation formed between the target and the pixel. It is a parameter that depends on the F-number of the optics [1]. Then the expression is integrated into the desired wavelength range as it is indicated in Equation 5.29. To not get into confusion, this power is the one computed in Earth. The power in space will be explained in the next subsection.

$$Etendue = ps^2 \cdot f_f \cdot \frac{\pi}{4 \cdot F^2} \tag{5.28}$$

$$P(\lambda, T)_{ground} = \int_{\lambda i}^{\lambda e} \frac{2hc^2}{\lambda^5 \left(\frac{hc}{e^{\lambda k T}} - 1\right)} \cdot Etendue \tag{5.29}$$

Where ps is the pixel size in [m^2] and f_f is the fill factor.

In addition to this, it was seen in the NETD Equation 2.4, and Equation 2.4, how the ratio of the responsivity by the noise voltage is equivalent to the detectivity, D, in [W^{-1}]. Therefore the SNR can be also calculated with Equation 5.30.

$$SNR = P \cdot D \tag{5.30}$$

For the SNR it can be used also the Equation 5.17, if it is known the specific detectivity, D^* or the noise equivalent power, NEP.

As an example, the SNR will be calculated for the 'Bird 384' used in the NETD measurements. This microbolometer has a detectivity of $9.6 \cdot 10^{10}$ W^{-1}. The black body temperature (the target of the NETD experiment), will be set between 260 K and 320 K. For the wavelength range between 8 μm to 14 μm. Now, using Equation 5.30, it can be obtained the Figure 5.7, variation of the SNR of the detector with the temperature of the target. Everything computed in the ground.

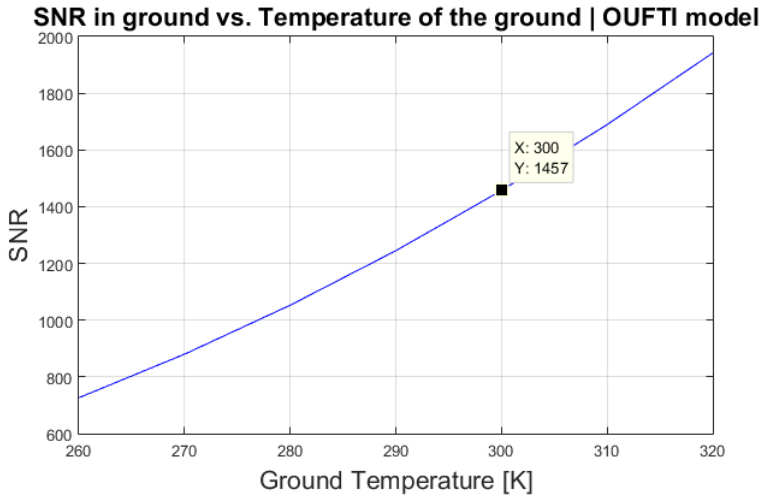

Figure 5.7: SNR vs. Temperature of black body for the SCD microbolometer 'Bird 384' F number 1

The graph of Figure 5.7 shows how the SNR increases with the temperature of the scene as it can be assumed. With a value of SNR in the order of 1457 for a black body at 300 K., These values are very high but is important to see that the F-number used is very low.

The same procedure was realized for the HgCdTe photodetector 'HiPIR Engine HOT' example. The NETD is 25 mK for a cold filter F-number of F/2.2. The result appears in Figure 5.8. It can be seen how the SNR is higher for the same temperature in comparison with the microbolometer. The reason why the values are not much

larger than the microbolometers is because not only the F-number is higher F/2.2 (it is in the denominator of the solid angle equation), but also the radiation in the MWIR range is lower than in the LWIR range. The power received at 300 K, for this setup is 1.229 W.

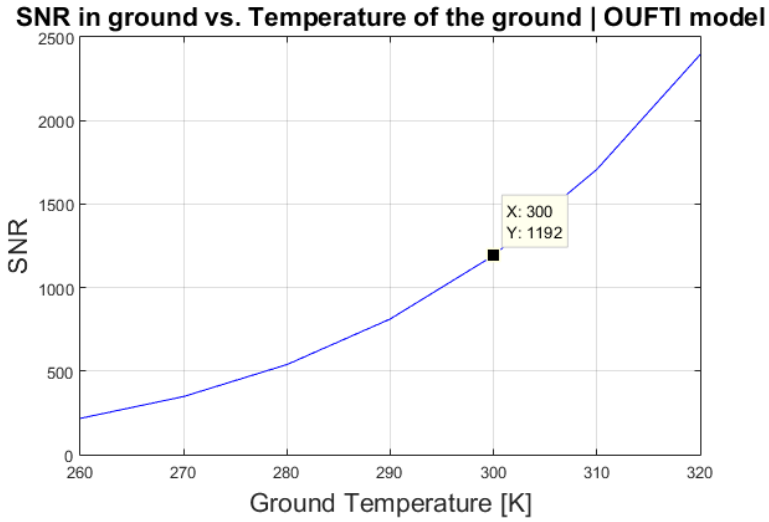

Figure 5.8: SNR vs. Temperature of black body for the German AIM HgCdTe photodetector HiPIR EngineHOT F number 2.2.

5.6.1 SNR in space

For the computation of the SNR in space, it can be used the same procedure as in the ground. The difference will be the power received since the detectivity D, in W^{-1}, does not change with the altitude.

In space, the satellite is receiving radiation from the Sun, the albedo, the Earth and the satellite itself. These different sources of power can be calculated with the use of the Plancks law, and the respective solid angles and transmittance considerations. The detailed study of these different power is included in the Master Thesis [102]. On this document, it was determined how for the LWIR, 8 μm to 14 μm range, and for the MWIR, 4.4 μm to 5 μm range, the contribution of the ground in the total power is much larger than the one coming from the albedo. This is not the case for the MWIR 3.6 μm to 4.2 μm range, where the contribution of the albedo is very important.

After several tests, it has been considered that for the computation of the SNR in the space it will be taken into account only the power coming from the Earth. The SNR will be computed for wavelengths larger than 4.4 μm. For the 3.6 μm to 4.2 μm

range where the albedo highlights over the ground power, it will be necessary to create a model to correctly analyse the SNR, what can be very interesting to do in future projects in the topic.

The power coming from the ground, in [W], is computed considering the Planks law, the etendue of the optics, the emissivity of the ground and the transmittance of the optics. The exact model is presented in the Master Thesis of reference [102].

For example, in the microbolometer used in previous sections ('Bird 384'), it is computed an SNR in space, using Equation 5.30, of 559.6 for a surface temperature of the Earth of 300 K. The wavelength range considered is between 8 μm to 14 μm; the value of the etendue was calculated with an F-number of the optics of the satellite of F/1.4; the transmittance of the optics was set in 0.8; and finally the emissivity of the Earth was considered as 0.97 [102]. In Figure 5.9, it is represented the SNR in space for this microbolometer at different ground temperatures. Therefore, the SNR has turned from 1457 (Figure 5.7) with an F/1 at 300 K in the laboratory; to 559.6 in space at F/1.4 and 300 K ground temperature.

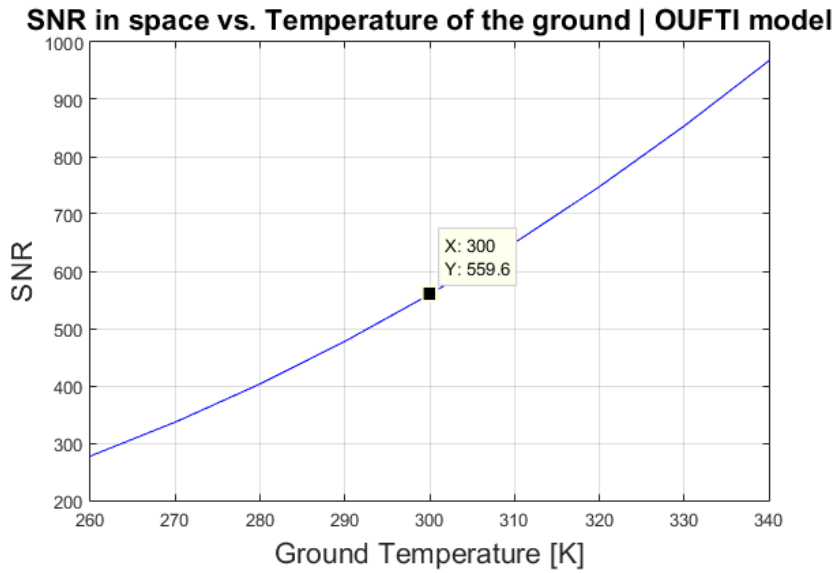

Figure 5.9: SNR in space vs. Temperature of the ground for the SCD microbolometer 'Bird 384' F number 1

5.6.2 Specific detectivity

The last step in this chapter will be to compute the specific detectivity, D* in [m·Hz$^{1/2}$/W]. This parameter is very useful to compare different detectors. However, this parameter

is very complex to determine theoretically. The next model has to be considered as an approximation for the real values.

The starting point is to express the equation for the NETD in terms of specific detectivity [m·Hz$^{1/2}$/W], instead of the detectivity [W^{-1}], [6] [101].

$$NETD = \frac{4 \cdot F^2 \cdot \Delta f^{1/2}}{D^* \cdot A^{1/2} \cdot \phi_{\lambda 1-\lambda 2} \cdot \pi \cdot \left(\frac{dP}{dT}\right)_{\lambda 1-\lambda 2}} \tag{5.31}$$

Where Hz$^{1/2}$ is the frequency bandwidth of the circuits of the detector [Hz], discussed already in Section 5.4.1. It was defined as the inverse of two times the integration time of the circuits in [s]. The second unknown is the specific detectivity D*.

The frame rate at which the NETD is calculated is usually provided by manufactures. For example, in the SCD 'Bird 640 Ceramic' microbolometer it is indicated that the NETD was computed at 60 Hz [5]. The integration time of the circuits is commonly defined to be equal to the exposure time, which can be also considered as half of the frame rate. For example, a frame rate of 60 Hz corresponds to an image each 16.67 ms, the integration time of the circuits can be considered as 8.33 ms and therefore the Hz$^{1/2}$ of the NETD equation will be 7.75 Hz$^{1/2}$. Despite this, the value of the integration time of the circuits can go from μs to ms has it was explained. The manufacturers provide with the frame rate but not with the exact integration time of the circuits. Moreover, the specific detectivity is also not provided and therefore it was not possible to check the final values. In Figure 2.17, it was presented a graph with all the common detectivity values for the main photodetectors and thermal detectors. It is assumed that all of them have been measured with the same time constants, nevertheless, it is also not indicated the value of these ones.

As an example, it will be calculated the specific detectivity for the 'Ceramic Bird 640'. The SCD detector is 35 mK NETD, for the 8 μm to 14 μm range, with a 17 μm pixel pitch, F/1, and assumed 80% fill factor and 0.9 filter transmission. It was discussed before that this microbolometer was tested at 60 Hz frame rate and therefore it is also assumed an 8.33 ms integration time of the circuits. Introducing these values into Equation 5.31, it is obtained a value of 2.84$\cdot$ 10^7 m·Hz$^{1/2}$/W for the specific detectivity. If the specific detectivity equation is recalculated for different integration times of the circuits, the specific detectivity increases until a value of 8.03$\cdot$ 10^8 m·Hz$^{1/2}$/W. Looking back to the figure of all the specific detectivities, it can be seen how thermal detector values are in the order of 10^6 m·Hz$^{1/2}$/W to 10^7 m·Hz$^{1/2}$/W

or higher like the ideal thermal detectors with a value between 10^8 m·Hz$^{1/2}$/W to 10^9 m·Hz$^{1/2}$/W. Therefore it can be seen how the values obtained in the model of this project are in the correct order. It will be necessary to know the exact value of the time constant used by the manufacturers for further investigations.

The same procedure was carried on with the HgCdTe 'HiPIR Engine HOT' from AIM. There were considered the same assumptions in terms of fill factor, filter transmission and time constants than in the previous example. The specific detectivity obtained for an 8 ms integration time of the circuits was $2.31 \cdot 10^8$ m·Hz$^{1/2}$/W extending until $6.54 \cdot 10^9$ m·Hz$^{1/2}$/W for an integration time of the circuits of 10 μs. The values for the D* of HgCdTe photovoltaic infrared detectors in Figure 2.17 are in the order of 10^8 m·Hz$^{1/2}$/W to 10^9 m·Hz$^{1/2}$/W for the MWIR range at 77K. The AIM detector is optimized to work at 160 K FPA temperature, which may introduce also differences respect to the 77K HgCdTe photovoltaic detectors of the global figure of the detectivities.

5.7 Conclusions

This chapter summarises the different sources of noise that limit the performance of infrared photodetectors and thermal detectors. It has been seen, how the noise in photodetectors is considerably lower than in thermal detectors. However, photodetectors need to be cooled in order to operate. This makes them bigger, which can be incompatible with small CubeSat missions.

Both, infrared photodetectors and thermal detectors microbolometers, have been used in several satellite missions. For example, the MISTIGRI mission used an LWIR microbolometer for agriculture monitoring.

The main source of noise in microbolometers is the 1/f (flicker) noise. It is due to imperfections in the construction and joints of the different pixels of the focal plane array. The second source of noise in the Johnson noise. Microbolometers have a very small size, and therefore, it emerged the idea to passively cooling a microbolometer in order to improve its performance. With the model described in this chapter, it has been tested a reduction in the temperature of a microbolometer from 300 K to 200 K. The results demonstrated that there is no any advantage in cooling down a microbolometer. Only a slight reduction in the noise was achieved. The main noise is the 1/f noise and it does not depend on the temperature of the detector.

The main achievement of this chapter was to create a model to compute the temperature resolution and signal-to-noise-ratio, of all types of detectors, in the ground and in the space environment. This model was checked with the results obtained for the JEM-EUSO instrument that will be incorporated in the International Space Station. For the development of the model, it was necessary to directly get in touch with several manufacturers of infrared detectors, Sofradir, Teledyne, FLIR, Xenics and Hope-Wish Technologies.

Now, with the data provided in the manufacturers data-sheets, is possible to compute the performance of the detectors in different conditions and ground temperatures what will be very useful to possibly compare the different detector technologies. The selection of the best detectors using this model is included in Chapter 7.

Chapter 6

CubeSat and satellite missions in the infrared

6.1 Introduction

In the last three decades, several satellite missions in the infrared wavelength range have been developed. Some of these missions have been discussed in previous sections. For example, it was presented the MIR instrument of the James Web Space Telescope which incorporates an HgCdTe photodetector. On the other hand, it is also possible to find infrared technology in CubeSats.

In this chapter, there will be cited different CubeSat and satellite mission of high interest for the project. The infrared technology of these missions can be used as a reference for the OUFTI CubeSat development. The devices presented can be used as a reference for further investigations in a specific subsystem and its relation with the other subsystems of the CubeSat.

6.2 CubeSat missions

- **CIRAS CubeSat:** The acronym of CIRAS stands for CubeSat Infrared Atmospheric Sounder. It is a 6 U multispectral CubeSat for the MWIR 4.08 μm to 5.13 μm range. It has been developed by the NASA/JPL to be launched in 2019. This CubeSat will be used for temperature and water vapour sounding. It is a highly interesting CubeSat mission due to the technology that it incorporates. The detector is a cutting-edge barrier T2SL nBn/pBn detector operating at a temperature of 150 K developed by the American Lockheed Martin Santa Barbara Focalplane. This detector is characterised by a very low 1/f noise and

cost comparing with HgCdTe (MCT) detectors operating at similar temperatures and in the same wavelength range. As a result, it requires fewer calibrations in space which is a very attractive feature for a CubeSat mission. The quantum efficiency of the detector is higher than 70 %. The detector is 640x512 pixels. There are unused pixels and only an equivalent 625x506 pixel detector is used [30]. [103]

The cryocooler used is a low vibration and large lifetime coaxial micro pulse tube (MPT) developed also by Lockheed Martin.

The optical instrument is a scanning device. It has a multispectral capability of 625 channels. One channel for each used row of the detector. The instrument used to split the light is a grating. The device, so-call MWIR grating spectrometer (MGS) has been developed by Ball Aerospace and the JPL. This MGS device produces the dispersion of light forming a 2D image in the FPA. The 504 pixels is the spatial direction while the 625 pixels is the spectral direction [103].

In terms of spatial resolution, the GSD of the CubeSat will be varied between 3 km to 13.5 km through binning of the detector. The altitude of the CubeSat is indicated to be between 400 km and 600 km. In terms of temperature resolution, it is set an objective NETD lower than 0.25 K for a target temperature of 250 K.

In addition to this, the CubeSat has a total mass of 14 kg [103] [30]. All the discussed components of the CIRAS CubeSat are illustrated in Figure 6.1.

- **EON-IR CubeSat:** The Earth Observation Nanosatellite Infrared, is going to be a future 12 U CubeSat for Earths remote sensing developed by NASA/JPL. This CubeSat has not been developed yet, but it is cited due to the importance and relation with the future OUFTI CubeSat of the Centre Spatial de Liège. The CIRAS CubeSat is oriented as a technology demonstrator for the future EON-IR. It is oriented also for the MWIR [104].

- **ISARA CubeSat:** The Integrated Solar Array and Reflectarray Antenna CubeSat stand for a technology demonstrator launched in December 2017. It was developed by NASA/JPL. This 3U CubeSat was used for telecommunication purposes. In addition to this, in one of the 1U units, it was incorporated the CUMULOS (CubeSat Multispectral Observation System) instrument.

  This instrument contained three infrared cameras. The first one included a

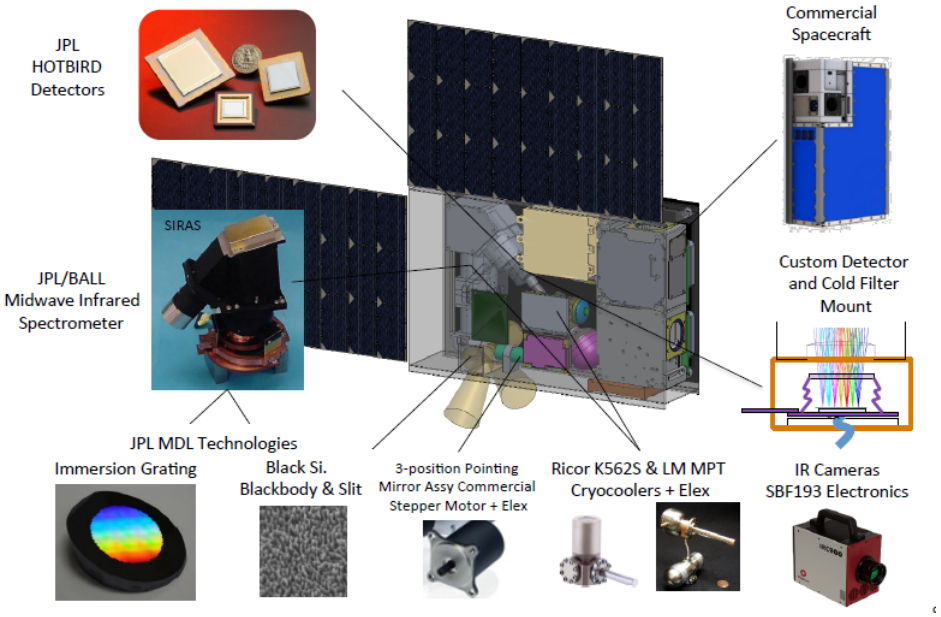

Figure 6.1: Optical subsystem of the 6U CubeSat CIRAS from NASA/JPL.[30]

CMOS 1280x1024 pixels detector for the visible (0.4 μm to 1.0 μm). The second one a FLIR InGaAs 640x512 pixels detector for the SWIR 0.9 μm to 1.7 μm range. And the third one a VO_x CMOS microbolometer 640x512 pixels for the LWIR 7.5 μm to 15.5 μm range [31]. In Figure 6.2 it is illustrated the ISARA CubeSat.

The LWIR camera is the Tau 2 instrument from the American FLIR. The temperature resolution of the camera is 50 mK with an F-number of F/1.2, [38]. This camera is going to be also used in the Phoenix CubeSat developed by the Arizona State University in the US.

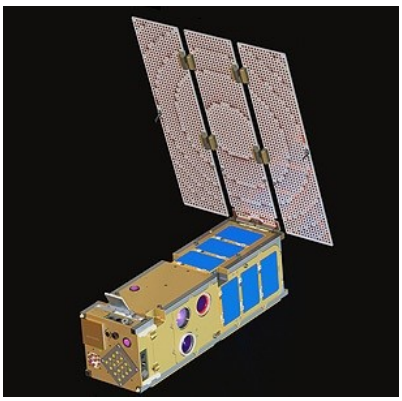

Figure 6.2: 3U ISARA CubeSat for telecommunications, implementing a triple camera for the SWIR, LWIR infrared observation.[31]

- **MMO CubeSat:** The Mars Micro Orbiter is a 12 U CubeSat developed also by NASA. It was presented in section , describing the filter wheel that it used for multiband observation in the infrared. As a remember, this CubeSat incorporated three cameras, one for the visible range and two for the LWIR range, The infrared detector for the LWIR are microbolometers 17 μm pixel pitch and 640x480 pixels FPA. With the use of an eight-position filter wheel, the MMO CubeSat achieves multiband performance in the LWIR [13].

- **COSINE HyperScout:** it is a hyperspectral imager module for the very near infrared (VNIR) range from 0.4 μm to 1.0 μm. This module of only 1.1 kg incorporates an onboard data processing computer for the image processing, and therefore reducing the amount of data that has to be downloaded. This device allows for hyperspectral operation in 50 bands and it has been incorporated in CubeSats developed by the European company GOMSpace [105].

6.3 Satellite missions

As it was discussed before, infrared technology has been used several times in satellite missions and also instruments for the International Space Station, ISS. In Table 6.3, there are listed some of this mission, highlighting the infrared detectors incorporated in the different optical instruments. As a remark, the cutting-edge HgCdTe photodetectors are the most commonly used due to their reliability and flight heritage. These two properties are very suitable for space missions.

6.4 Conclusions

For the OUFTI CubeSat, the most important reference is the CIRAS CubeSat. It implements a photodetector for multiband imaging in the MWIR. In addition to this, the EON-IR 12 U CubeSat is also of extreme importance. At the moment, there is no detailed information about this mission besides that it will be a larger version of CIRAS CubeSat. The optical design of these two missions can be also considered as a starting point for saving time for the OUFTI mission development.

Moreover, there are not CubeSat missions incorporating a thermal detector, microbolometer, for the MWIR. There have not been developed CubeSats operating in dual-band MWIR-LWIR with the use of a thermal detector. As a result, it will be a

Satellite/Mission	Infrared detector	Wavelength
Cassini-Huygens (DISR ins.)	InGaAs PD	SWIR
ENVISAT (SCIAMACHY ins.)	InGaAs PD	SWIR (2.4 μm cut-off)
PROBA-V (Multispectral ins.)	InGaAs PD	SWIR
HST (WFC3 ins.)	HgCdTe PD	SWIR
WFIRST Telescope	HgCdTe PD	SWIR
Euclid Mission	HgCdTe PD	SWIR
JWST (NIRCam, NIRSpec, NIRISS, MIRI ins.)	Teledyne HgCdTe PD	0.6 μm - 5 μm
Meteosat Satellite (FCI ins.)	Sofradir HgCdTe PD	LWIR
GCOM (SGLI ins.)	Sofradir HgCdTe PD	LWIR
JWST (MIRI ins.)	Raytheon Si:As PD	5 μm - 29 μm
WISE mission	DRS and Raytheon Si:As PD	LWIR
Spitzer Space Telescope (SST)	Si:As PD	LWIR
Landsat Continuity Mission (TIRS ins.)	QWIP PD	MWIR
HyspIRI (HyTES ins.)	Multicolor QWIP FPA	7.5 μm 12 μm
EO1 mission (ALI ins.)	Single FPA multispectral, Si and HgCdTe PD	0.433 μm - 2.35 μm.
JAMI Meteorological Mission	2x HgCdTe PD	0.55 μm - 12.5 μm
PARISIR ins. for atmosphere monitoring	InSb/HgCdTe dual band PD	SWIR
Atmospheric Infrared Sounder (AIRS ins.)	BAE Sys. HgCdTe PD	3.7 μm - 15.4 μm
Crosstrack Infrared Sounder (CrIS)	Teledyne HgCdTe PD	3.5 μm 15.4 μm
FUEGO Mission	Microbolometer	8 μm 12 μm
Mistigri Mission	Microbolometer	8.6 μm 11.5 μm
JEM-EUSO ins. for the ISS	Microbolometer	LWIR
PICASSOCENA (IIR ins.)	Microbolometer	LWIR
EMBERSAT	Microbolometer	LWIR
2001 Mars Odyssey mission (THEMIS ins.)	Microbolometer	6.8 μm - 14.9 μm
Orbital Express Mission, ASTRO satellite	Microbolometer	LWIR
Aquarius SACD mission (NIRST ins.)	Microbolometer	LWIR

Table 6.1: Infrared subsystems of diverse satellite missions. ins. stands for instrument, PD for photodetector, LWIR, for 8 μm or larger wavelengths, MWIR for the range 3 μm - 5μm, SWIR, for wavelengths from 1 μm to 3 μm. From references, [23] [33], [34], [35], [28],[36]

real success to develop a CubeSat with such characteristics. An idea that has to be taken into account for the OUFTI mission.

Chapter 7

Results and analysis of the different detectors offered by the manufacturers

7.1 Temperature resolution requisites for the mission

The main objective of this project is to test the performance of infrared detectors in the space environment. In the previous chapter, it was achieved a model to compute the noise equivalent temperature difference (NETD), the signal-to-noise ratio (SNR) and the specific detectivity, D^* not only in the ground but also in the space environment. There were obtained different values for some of the detectors tested. The next step will be to interpret these values in order to know if finally, the detector fits with the requirements of the mission.

A research was done looking for different satellite mission oriented to the Earths observation. There were found for some mission the requisites and constraints in terms of temperature resolution and eventually also the SNR that characterize their optical instruments.

One of the missions of higher interest in the MISTIGRI satellite. This mission has been cited several times along the project. It is oriented to monitor irrigated fields and to detect the plant water stress. The satellite, developed by the French space agency, CNES, and Thales Alenia Space, is oriented to be a microsatellite with two optical instruments. One for the VNIR range and the other for the LWIR range [23].

The LWIR instrument of the MISTIGRI mission includes a microbolometer from the French manufacturer ULIS. This microbolometer contains over its surface a four

TIR instrument	**TIR1**	**TIR2**	**TIR3**	**TIR4**	**Requirement**
NETD 290 K	0.2 K	0.3 K	0.5 K	0.6 K	<0.5 K

Table 7.1: Temperature resolution requisites for the MISTIGRI satellite in the LWIR range. [23]

band-pass filters for multispectral observation in the LWIR. On the report of the mission, it is included the SNR and NEDT budget requirements which are presented in Table 7.1. The pupil diameter of the optical instrument is 270 mm at an altitude of 720 Km. On this table is indicated that the temperature resolution has to be lower than 0.5 K, [23]. The system will detect changes of at least 0.5 K in the temperature of the crops. For the SNR it has been set a value higher than 100.

Another example is the JEM-EUSO instrument that will be installed in the International Space Station, ISS. This instrument incorporates also a microbolometer working in the LWIR range. The objective will be to monitor the cloud temperatures with a NETD value lower than 0.5 K. It is also a multiband instrument and the requirement of < 0.5 K are applied for all the bands [28].

A third example is the FUEGO mission with components from ALCATEL Space and THALES Optronique besides an infrared microbolometer from Sofradir in France. It was a mission for the detection of fires in low illumination conditions and during the nights. The temperature resolution was a NETD lower than 0.4 K for a 300 K black body temperature, [35].

In addition to this, a very detailed study of the temperature and spatial resolutions for different satellite purposes is included in reference [98]. This document collects the requirements that different satellite missions had in the thermal infrared. For example, the European Remote Sensing Information Service, ERSIS, mission, had a NETD requisite between 0.1 K and 0.5 K at 300 K black body temperature, for the crop hydric stress measurement. The spatial resolution of this instrument was 200 m. The ERSIS satellite was also used for fire detection for which the NETD requirement was only between 1.5 K and 2 K since the signal captured is much higher [98].

In conclusion, and according to the discussed example, it has been determined a temperature resolution requisite for the OUFTI mission of <0.4 K.

7.1.1 Differences between the MWIR and the LWIR band

In the introduction chapter, there were presented the differences between the MWIR and the LWIR band. For a higher comprehension of this chapter, there are going to be cited again the main characteristics of both bands.

The maximum peak of the Earths radiation is in the 8 μm to 14 μm range. Observing in this band it is possible to have a higher sensitivity observing at ambient temperature objects. Also, in mist and smoke atmospheric conditions, the transmission in the LWIR range is better. This high sensitivity could be a disadvantage for high-temperature objects. For example, a fire or a volcano. Then the MWIR range 3 μm to 5 μm is more appropriate for hotter objects. Other advantages of the MWIR band are a higher contrast (the variation of the power received with the temperature) and high transmissivity in conditions of very high humidity. In addition to this, the emission of the Earth constituents is different for the MWIR and the LWIR range [40].

The objective of this chapter is to analyse all the possibilities. From single band detectors to the cutting edge dual-band detectors.

7.2 Single-band detectors

In the conclusion of Section 2.6, there were summarized the properties of the best infrared single band detectors. However, not all of them are available at the moment in the market. This is the case for example of the QDIP photodetectors, tested at the laboratory and offering larges performance in terms of detectivity and dark current at high temperatures. Another example may be the high temperature superconducting thermal detectors.

In this chapter, there will be analysed only the detectors already available in the market that can be interesting for the OUFTI mission. Moreover, there have been excluded from the list manufacturers as the American Raytheon, since they do not sell their technology in Europe.

7.2.1 Single-band MWIR detectors

The main infrared detectors for the MWIR range are the photodetectors. Thermal detectors are not commonly used for the MWIR. With exception of the microbolometer used by the FUEGO mission for fire detection in this range. Nine photodetectors will be compared in this section. The selection process was realized considering the

temperature of operation and the size of the detectors as the major constraints. In addition to this, there have been considered detectors with different FPA materials. The detectors selected appear at Appendix A.

All the parameters used have been extracted from the manufacturer's datasheets with special caution in the F-number used to perform the ground tests at the laboratory. The parameters that are going to be analysed are the NETD in space, the SNR in space, the SNR in the ground, the detectivity, and the specific detectivity. In addition to this, each parameter is going to be measured for each detector at 280 K, 300 K and 320 K.

The measuring procedure is next explained.

- **Detectivity:** In the ground, the detectors are measured in a specific wavelength range, for an F-number. The temperature of the black body observed is in general 300 K. There are exceptions like in the LEO-LP MW detector from Sofradir, measured at 293 K. This has been taken into account during the calculations. With this information and using Equation 5.20, the detectivity in [W^{-1}] is measured. The optical filter transmission parameter has been always considered as 0.9. The fill factor is assumed to be for all the detectors equal to 0.56 [5]. The detectivity is unique and it does not change with the altitude of the satellite.

- **NETD in the space:** it is computed using Equation 5.25. The transmission of the optics is for all detectors 0.9. The F number considered for the optical instrument of the satellite will be also for all the detectors equal to F/1.4. An important point will be the wavelength range considered for the analysis. It was discussed how the model developed starts at 4.4 μm since the model does not consider the radiation coming from the albedo which is very important for wavelengths lower than 4.2 μm. For the 4.4 μm to 5.1 μm region, it is considered for the MWIR a value of 0.614 of the atmospheric transmittance. The ground emissivity is 0.97 for the MWIR range.

- **SNR in the ground:** calculated with equation 5.30, considering always 0.75 fill factor of the pixel.

- **SNR in space:** computed with the Equation 5.30 for wavelengths higher than 4.4 μm for the reason discussed in the space NETD. The power coming from the Earth, the only one considered, is adapted to the wavelength range in which the

measure is carried on. The wavelengths ranges are included in the result tables. The transmission of the optics is 0.9 and the F-number in space always F/1.4.

- **Specific detectivity:** this parameter is calculated assuming always a frame rate of 60 Hz, and according to Equation 5.31, to obtain m·Hz$^{1/2}$/W. Fill factor, 0.56.

A cautious measuring was carried on. All the results obtained for the three range of temperatures, 280 K, 300 K and 320 K, are included in the tables of Appendix A.

7.2.1.1 Analysis of the results obtained in the MWIR

For the different parameters, it was obtained:

- **Detectivity:** it is a very important parameter for the calculation of the NETD and SNR. Since it is not dependent on the frequency, fewer assumptions were done, and therefore the exactitude of the NETD and SNR values is higher. However, it cannot be used to compare the different photodetectors, in contrast with the specific detectivity which is defined per unit of frequency bandwidth and active area of the pixel.

- **SNR in the ground:** the values of the SNR are proportional to the temperature of the black body. Higher temperatures mean higher SNR. The four detectors with a higher SNR in a wide MWIR range (3.6 μm to 5 μm), are the LEO-LP MW, the HiPIR-Engine HOT, the SuperHawk and the IRnova Dag MW. The three first ones are HgCdTe photodetectors, while the IRNove Dag MW is a T2SL. This performance was expected according to the bibliography of chapter 2. The highest value, 861.8, at temperature of the black body 280 K is the LEO-LP MW, HgCdTe photodetector for a wavelength range between 3.7 μm and 4.8 μm. The second one, the HOT Hawk with, 830.8 SNR at 280 K black body, in a wavelength range form 3 μm to 5 μm.
  In a similar wavelength range, from 4.4 μm to approximately 5 μm, the HOT Hawk values of SNR are higher. In addition to this, the HOT Hawk can operate at higher temperatures, until 175 K, and therefore it is the one selected. On the other hand, the third detector with the highest SNR in the wide MWIR range, the IrNova Dag MW, has a higher SNR than the HgCdTe HOT Hawk for the 4.4 μm to approximately 5 μm range. Nevertheless, the temperature of operation is

much lower, 80 K. The same problem of temperature affects the InSb Pelican-D JT 640.

Comparing the Kinglet 640 with the Mini Blackbird 1280, the SNR of the Kinglet is higher for the same wavelength range. A difference that comes from the different F-number but also from the pixel size. The Mini Blackbird has a smaller pixel size, and this is usually related to smaller SNR values has it has been explained in this project. Comparing the HiPIR Engine HOT and the HOT Neutrino Swap C, the values of this last one are higher for a similar wavelength range. The HOT Neutrino Swap C is T2SL and therefore the cost will be lower. However, the HiPIR Engine can operate at 160 K in contrast with the 130 K of the HOT Neutrino SWAP C.

In conclusion, the HOT Hawk offers very adequate values of SNR in the ground, nevertheless it is comparably bigger than the HiPIR Engine HOT or the HOT Neutrino Swap C. On the other hand, the cost of the T2SL HOT Neutrino will be lower than the other two HgCdTe photodetectors.

- **SNR in space:** in space, it has been considered that the detector is installed in an optical instrument with an F-number of F/1.4. The best SNR in space is for the LEO-LP MW. The difference with respect to the others is very big even taking into account that the detector was measured with a black body at 293 K in the ground. This HgCdTe detector is definitely a good decision if a large SNR is required.

  After the LEO-LP MW, it can be found the HOT Neutrino SWAP C with a value of 85.48 of SNR at a temperature of the ground of 272 K (280 K temperature of the black-body times the Earth Emissivity). The values of the SNR considerably increase with the temperature until 359.5 in the 4.4 μm to 5.0 μm range at 291 K temperature of the ground for the HOT Neutrino SWAP C. The 80 K operational temperature IRnova Dag MW, has also values of SNR close to the HOT Neutrino SWAP-C.

  For the SCD detectors, Kinglet 640 and Mini Blackbird 640 it has not being possible to compute a value of the SNR in space since the model of equations starts in 4.4 μm as discussed before.

  Is important to remark that there has not been found a document with the specific values of SNR for a specific detector in order to make a comparison. However, these values are computed from the detectivity obtained in the NETD

model which was check and corrected with the JEM-EUSO ISS instrument values [28].

- **NETD in space:** as it can be expected, the NETD values are also inversely proportional to the temperature of the ground. Higher temperatures are related to a higher incoming signal. For the NETD in space, computed also for an F/1.4. The two detectors with the best temperature resolution are again the LEO-LP MW and the HOT Neutrino Swap C. Is important to see how the values of NETD is very low. It cannot be compared with thermal detectors since at the moment any of them has been considered for the MWIR. Nevertheless is the LWIR it will be seen also the huge differences between photodetectors and thermal detectors for the same range.
  In conclusion, any of the photodetectors selected will accomplish the discussed temperature resolution requisites for this mission.

- **Specific detectivity:** the two detectors offering the best specific detectivities are the SCD Kinglet 640 and the Mini Blackbird 1280. However, the specific detectivity was measured in the 3.6 μm to 4.2 μm range in contrast with the other detectors measured from 3.6 μm to 5 μm. For the other detectors, the higher values are assigned to the HiPIR Engine HOT and the HOT Hawk detectors. Both HgCdTe detectors. According to Figure 2.17, HgCdTe detectors offer the highest detectivities in the MWIR range. Also, the order of magnitude obtained is according to the cited figure (here the D^* m·$Hz^{1/2}$/W and in Figure 2.17, the D^* is in cm·$Hz^{1/2}$/W, to avoid any confusion). Even if this parameter is the one with the large assumption considered, the frequency bandwidth, it can be seen how the values are in the correct order.

7.2.1.2 MWIR Conclusions

From the nine detectors analysed, the Kinglet 640 and Mini Blackbird 1280 are considered as the less appropriate sensors for the mission. Even if they operate at very high temperatures, they have the drawback of an operation wavelength in the range of 3.6 μm to 4.2 μm. In this range, as it has been discussed, the importance of the albedo is very high, and therefore, worst measurements can be done in comparison with the 4.4 μm to larger wavelength range.

The detector HgCdTe LEO-LP MW has shown the highest values of SNR not only in ground but also in space. The problem can be the 110 K operational temperature. The other very important HgCdTe detector is the HiPIR Engine HOT, with one of the highest specific detectivities. In addition to this, it has a very small size and operational temperature of 160 K. However, the SNR in space is lower comparing with the HOT Neutrino Swap C also with a very small size. The temperature resolution is also higher for the HOT Neutrino Swap C.

For a CubeSat mission, it is not worthy to the extra size of the LEO-LP MW detector in order to have the best performance. As a result, there has been selected the HgCdTe HiPir Engine HOT and the T2SL HOT Neutrino Swap C as the best detectors for the MWIR.

7.2.2 Single-band LWIR detectors

For the LWIR range, there have been considered three photodetectors and the four best thermal detectors microbolometers available at the market. The objective is to see if it is possible to accomplish the requirements of the mission with a cutting-edge microbolometer. These detectors are included in Appendix A.

The procedure followed for the measurements is similar to the one realized in the MWIR range. For the calculations, there will be used again a 0.9 of optical transmission, 0.9 of filter transmission and F/1.4 for the F-number of the optical instrument in space. The fill factor is 0.56 for all the detectors except for the two ULIS a-Si microbolometers were it has been considered a 0.64 fill factor following the manufacturer datasheet. For the emissivity of the Earth, it has been considered a value of 0.9812 for the wavelength range between 8 μm to 14 μm. The atmospheric transmission in the LWIR is set in 0.902. Finally, for the specific detectivity, it is considered a 60 Hz frame rate. As a remark, the model is valid for wavelengths larger than 8 μm.

The results obtained, again for 280 K, 300 K and 320 K temperature of the black body, are also included in Appendix A.

7.2.2.1 Analysis of the results obtained in the LWIR

For the different parameters, it was obtained:

- **Detectivity:** the microbolometers not only have in common that they have been tested between the 8 μm to 14 μm, but also, all of them are 17 μm pixel

pitch. Moreover, it was cited in this project how all the microbolometers are measured in the laboratory with an equivalent F-number F/1 in the ground. This will be very helpful to compare them. Between the four microbolometers, the higher detectivities in [W^{-1}] are given by the Bird 640 Ceramic Packing detector. The ULIS Pico 640 Gen 2 has the second best detectivities. On the other hand, the detectivity cannot be used to compare the photodetectors since the pixel size and wavelength range are different.

- **SNR in the ground:** as it was expected, the SNR in the ground for the same temperature of the black body, is considerably higher in photodetectors than in thermal detectors. The best SNR figures are achieved by the Pelican-D LW STD, with a value of 2681 in the ground. The Hawk LW photodetector SNR figures are just half of the Pelican-D LW ones. This is a positive result since the Pelican-D LW is a T2SL detector and the Hawk LW is a HgCdTe detector. The cost of T2SL is usually lower than HgCdTe detectors.
  On the other hand, for microbolometers, it is again the Bird 640 Ceramic Packing detector which has the higher SNR in the ground. The figures of the ULIS Pico 640 Gen 2 are also very elevated, for example, an SNR of 644.5 at 300 K temperature of the blackbody is obtained in the wavelength range between 8 μm to 10 μm.

- **SNR in space:** similar results are obtained for the SNR in space of microbolometers. Continuing with the previous example, the ULIS Pico 640 Gen 2 has now an SNR of 235.7 in the wavelength range between 8 μm to 10 μm observing a ground target of 299 K.
  It is important to take into account that the radiation received in the LWIR from the Earth is larger than the one received in the MWIR range. However, LWIR photodetectors are not as optimized as MWIR photodetectors. The NETD of LWIR photodetectors is larger than MWIR products. This is why there are not big differences in the SNR values obtained with the MWIR and LWIR photodetectors.
  A very important aspect is that the values obtained for the SNR of LWIR photodetectors in space are larger than the SNR figures in the ground. It is known that the power received in space is lower than in the ground. The reason why the values are higher is due to the definition of the discussed etendue of the optics,

and also in the high values of optical transmittance for the LWIR range. In the ground, for example, for the Hawk Long detector the F-number is F/2; for space optical instrument is F/1.4. In the MWIR range, the F-number F/1.4 it was also lower than the typical F-number of photodetectors, nevertheless, in the MWIR there was a big lose of power due to the low transmission of the atmosphere. If not, the values would have been also larger.

- **NETD in space:** equal to the MWIR range, all the LWIR photodetectors accomplish the 0.4 K temperature resolution requisite. This is not the case for all the microbolometers. The Bird 640 Metallic Packing and the Pico1024 Gen2, for a ground temperature of 279 K, already overpass the 0.4 K limit in the 10 μm to 12 μm range. Only in the 8 μm to 14 μm and 8 μm to 10 μm, the 0.4 K requisite is achieved for these two detectors.
  On the other hand, the Bird 640 Ceramic Packing and the Pico 640 Gen 2, fulfil the requirements for all the wavelength ranges analysed.

- **Specific detectivity:** the values of the specific detectivity are larger for the Bird 640 Ceramic Packing and the Pico 640 Gen 2, measured at the same 60 Hz frame rate, than the other two microbolometers. However, in this case, is not possible to do a significant comparison of the specific detectivities between photodetectors and thermal detectors. This is because it is not known if the photodetectors and microbolometers have been exactly measured at an equal frame rate. This is a point to investigate in future projects.

7.2.2.2 LWIR Conclusions

The results obtained show how it is possible to reach the temperature resolution requisites with two of the microbolometers. The Bird 640 Ceramic Packing and the Pico 640 Gen 2. Between these two microbolometers, the performance of the Bird 640 Ceramic Packing is slightly better. The Bird 640 Ceramic Packing is made of Vo_x while the Pico 640 Gen 2 is made of a-Si. It was discussed how a-Si microbolometers have bigger Johnson noise figures in comparison with Vo_x. The NETD of the Pico 640 Gen 2 is 40 mk, while for the Bird 640 Ceramic Packing is 35 mK. However, the fill factor of the Pico 640 Gen 2 is larger since a-Si material is easy to implement with CCD and CMOS read-out circuits.

It is very important to remark, that the SCD Bird 640 Ceramic Packing, it is also available at the manufacturer website with a 1024x728 pixels FPA size. The values of the NETD, pixel pitch and F-number are the same ones. Therefore all the values of SNR and NETD computed with the OUFTI model for the SCD Bird 640 Ceramic Packing are the same ones than the 1024x728 version. This is because the calculations are done per unit of pixel active area. The size of the FPA does not influence. In the 1024x728 pixel version, it is clearly indicated that the ROIC is CMOS.

Another positive aspect is that there was successful contact with both manufacturers ULIS and SCD, ensuring that it is possible to buy without restrictions their products.

As a remark, it was seen how the temperature resolution and SNR of photodetectors are larger than microbolometers. However, considering that they need to be cooled at a T lower than 100 K, they are finally not considered as an option for the LWIR range.

7.3 Multi-band detectors

Infrared detectors capturing light in two bands of the electromagnetic spectrum are already available at the market. These detectors can operate dual-band in the MWIR or dual-band MWIR-LWIR, as the state of the art Condor II Dual waveband from the Italian Leonardo. In this section, there will be analysed the four most promising technologies for multiband detection. The objective is to see if it is better to use two detectors or if only one is a possibility.

7.3.1 Multi-band photodetectors

There are three manufacturers of infrared dual-band photodetectors. These are the German AIM, the Italian (manufacturing in the UK) Leonardo and the American QiamgiQ, [37] [32] [39]. The properties of the dual-band detectors from these companies are included in Appendix A.

It is important to notice that only the Leonardo Condor II is able to operate in the two bands MWIR-LWIR at the same time. Moreover, the Condor II can discriminate between wavelengths when capturing at the same time. Furthermore, each band can be also used in a dedicated individual mode. In the laboratory, the detector was tested

in dual-band and in single-band. It is indicated at the datasheet the NETD for each band in single mode and the NETD for each band on the dual-band mode.

For the measurements, there will be considered the same assumptions than in the MWIR and LWIR range. A fill factor of 0.56 for all the three detectors. Also a 60 Hz frame rate. The other figures, like the transmissivities and ground emittances, will be the same ones considered for the single-band MWIR and LWIR detectors.

7.3.1.1 Analysis of the results

The results obtained for 280 K, 300 K and 320 K are next analysed.

- **Detectivity:** it can be seen how for the same detector, there are different values of the detectivity in W^{-1} since the wavelength ranges and NETD values are different. For example, the Condor II has four different NETD values. One for the MWIR band in single mode, one for the LWIR band in single mode, one for the MWIR band in dual mode and finally one for the LWIR band in dual mode. For this detector, the Leonardo Condor II, it can be seen how the best performance in terms of detectivity is achieved in the MWIR band for the single and dual modes. This is because of the lower values of NETD in the MWIR band. As discussed before, the radiation received in the LWIR range is larger but the materials are not so well optimized. For the Eagle 256, the same is happening. Better detectivities in the MWIR range.

- **SNR in the ground:** the single mode values of the SNR for the Condor II are higher than the Eagle 256 for the same wavelength ranges. Only the value of the MWIR band of the Eagle 256 overpass the SNR of the MWIR band in dual-mode of the Leonardo Condor II. On the other hand, the AIM Dual-color detector has larger values of SNR in comparison to the Condor II and Eagle 256 for the wavelength 4.4 μm to 5.3 μm. In this MWIR band, the SNR of the AIM Dual-color is 636.8 in comparison with the 396.8 value of the Eagle 256. Both observing a black body at 280 K.

- **SNR in space:** the NETD values of the dual-band photodetectors is larger than the discussed single-band photodetectors. This influences the SNR obtained in space. This is why in the dual-band detectors, lower values of SNR are obtained. For example, at 299 K temperature of the ground, the SNR for the wavelength range 4.4 μm to 5 μm of the Condor II detector is 45.2 for the single mode; in

the single band photodetectors for the same range, the SNR was in the order of 90.

On the other hand, the values of the SNR in the LWIR bands are much higher than the ones in the MWIR. This was expected according to the results obtained for single band MWIR and LWIR detectors. The Eagle 256 has the best value of SNR in space for the LWIR, but it needs to be considered that the wavelength range is different from the one of the Condor II. In comparison, for example, with LWIR microbolometers, the dual-band photodetectors figures of SNR are higher as it can be expected from the discussion of the previous section.

- **NETD in space:** all the detectors accomplish the requisites of the mission in terms of temperature resolution for the MWIR and LWIR band.

- **Specific detectivities:** the specific detectivities are better for the same wavelength range in the Leonardo Condor II. Not only for the single mode but also for the dual mode. However, as in microbolometers, it is not indicated if the frame rate was the same for the testing of the four configurations. Therefore it will be necessary to contact the manufacturer to be sure about this parameter.

7.3.1.2 Multi-band photodetectors conclusions

Between the Condor II dual-band and the Eagle 256, it has been seen how the performance in terms of SNR and temperature resolution is larger in the Condon II for the single band mode. In addition to this, Eagle 256 is a QWIP detector, characterised with very low quantum efficiencies, in the order of 10 %, and therefore, it is considered not appropriate for the mission. Recent communications with the Leonardo manufacturer has ensured that the Condor II can be bought without restrictions. Therefore, the Condor II is selected as the best option for a dual-band infrared mission.

On the other hand, the AIM dual-color MWIR-MWIR detector has lower detectivity and SNR figures in comparison with other MWIR single band detectors. As a result, it is considered that the best option for dual-band in the MWIR will be to use a band-pass filter over a single-band infrared detector.

7.3.2 Multi-band microbolometers

In general, all the microbolometers have a high-pass filter over their surface to limit their responsivity to the LWIR range of the electromagnetic spectrum. It is known

that the responsivity of microbolometers is equal for all the wavelengths. They cannot discriminate between the radiations coming from the different bands. In contrast, photodetectors have a point of maximum responsivity in the cut-off wavelength.

Removing the high pass filter, it is possible to obtain a wideband 3 μm to 14 μm microbolometer. This has been done by the Israel manufacturer SCD in one of their microbolometers. It is the Bird 640 Ceramic Packing BB Wideband. This detector has been adapted from the Bird 640 Ceramic Packing single-band. Therefore, they share the pixel pitch, F-number and FPA size. The NETD of the wideband microbolometer is 35 mK for the 3 μm to 14 μm wavelength range according to the specifications. The NETD of the single band Bird 640 Ceramic Packing was also 35 mK but for the 8 μm to 14 μm range.

If this detector is used in the wideband, 3 μm to 14 μm, it will be not useful, for the reasons discussed before. It will be not possible to differentiate from the radiation coming from the MWIR and the radiation coming from the LWIR. What it has to be done, is curiously, to put again a filter over the detector. But this time the filter can be for the transmission of the MWIR band only. In other words, it will be possible to have an equivalent single band MWIR microbolometer.

The objective of this section is to see the performance in terms of temperature resolution and SNR for an MWIR microbolometer. Moreover, it is also tested the microbolometer with a filter for the LWIR region. It will be seen how the values are slightly worse than the single band LWIR Bird 640 Ceramic Packing microbolometer, because as it has been explained, now the NETD is 35 mK measured for an interval from 8 μm to 14 μm.

The model of equations used is the same as for the other detectors. The MWIR bands are computed with the same assumptions of a single band MWIR detector. The same for the LWIR band. As a remark, the fill factor is 0.56 and the frame rate 60 Hz, equal to the other sections.

7.3.2.1 Analysis of the results

The results obtained computed for 280 K, 300 K and 320 K appear at Appendix A.

- **Detectivity:** as it was expected, the value of the detectivity in [W^{-1}] is lower for the wideband detector than in the single band Bird 640 Ceramic Packing detector. For the wideband the detectivity is $1.84{\cdot}10^{11}$ W^{-1}, while for the single LWIR band detector the value is $2.97{\cdot}10^{11}$ W^{-1}. As a remark, recap that the

detectivity is calculated in the laboratory, and then this parameter does not change with the altitude.

- **SNR in the ground:** the SNR in the ground is much larger for the LWIR band than in the MWIR band. It is clear that the radiation received in the LWIR is higher. For example, observing a 280 K black body, the SNR is 311.1 for the 8 μm to 10 μm range. For the LWIR, the values of SNR obtained are lower comparing with the ones of the Condor II multiband photodetector in the dual-band mode at the same wavelength range. For the 8 μm to 10 μm range and 280 K temperature of the black body, the Condor II has an SNR of 1924.

- **SNR in space:** similar results are obtained in the SNR in space for the wide band Bird 640 Ceramic Packing BB detector. It can be seen how the values of the SNR in the LWIR bands are larger than 100.
  On the other hand, the values of SNR when the microbolometer is used in the MWIR, are extremely low. These values increase with the temperature of the ground, as expected. The MWIR microbolometer will be limited for has to be used for very high-temperature scenes.

- **NETD in space:** this is the point of higher interest in the mission. For better comprehension, there has been done a graph of the NETD vs. temperature of the ground, included in Figure 7.1. On it, it is possible to see how the best figures for temperature resolution are reach in the 10 μm to 12 μm and 8 μm to 12 μm wavelength ranges. Also, it can be seen how for temperatures of the ground lower than 280 K, the temperature resolution is worse than the 0.4 K requisite for these last two wavelengths ranges. On the other hand, in the 11 μm to 12 μm and 10 μm to 11 μm range, it is not accomplished the 0.4 K temperature resolution requisite.
  A similar graph for the MWIR range is included in Figure 7.2. The values of NETD in space with an MWIR microbolometer are far above the requisites. Only at temperatures of the ground higher than 360 K figures are close to the 0.4 K objective. Therefore it is clear that an MWIR microbolometer cannot be used to capture with detail regular temperature ground surfaces (in the order of 300 K).

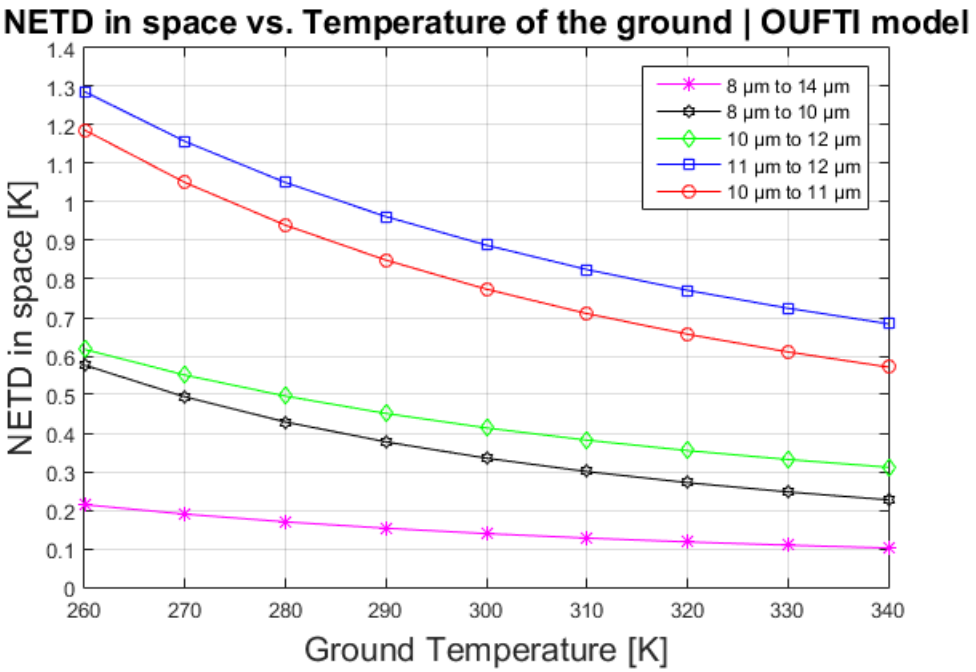

Figure 7.1: Computed values of temperature resolution for the wide band detector Bird 640 Ceramic Packing BB from the Israel manufacturer SCD. The detector has a band-pass filter for the LWIR.

- **Specific detectivities:** the value of the specific detectivity is $1.85{\cdot}10^{7}$ m·Hz$^{1/2}$/W, lower than the single band Bird 640 Ceramic Packing, but in the correct order of magnitude according to Figure 2.17, which compared photodetectors and thermal detectors specific detectivities.

7.3.2.2 Multi-band microbolometers conclusions

The wideband Bird 640 Ceramic Packing BB accomplish the temperature requisites in the 10 μm to 12 μm and 8 μm to 12 μm wavelength range. The values of the SNR and the NETD are worse than the single-band Bird 640 Ceramic Packing. If the mission is oriented exclusively to the LWIR, the single-band microbolometer must be chosen.

On the other hand, it is not possible to use exclusively a microbolometer MWIR for the mission. The temperature resolution requisites are far away to be accomplished.

However, this detector has big potential. The same detector material responds to all the infrared electromagnetic range, in contrast with single-band photodetectors. Therefore, one possibility can be to use half of the detector focal plane array for the MWIR range and the other half for the LWIR range. At the bibliography, there are

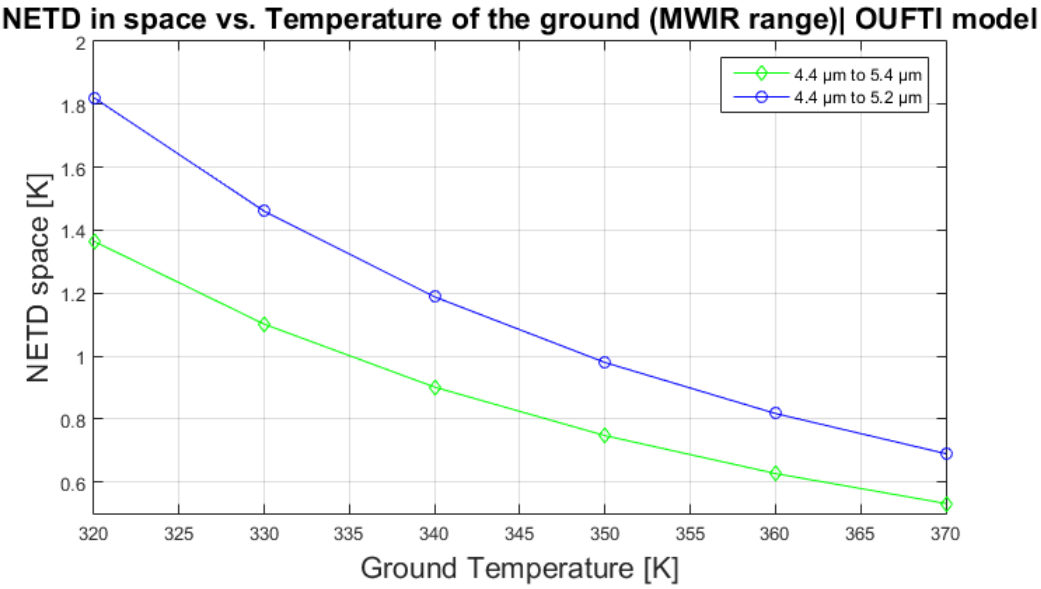

Figure 7.2: Temperature resolution for the wide band microbolometer Bird 640 Ceramic Packing BB used with a band-pass filter for the MWIR range.

examples of multi-band microbolometers in the LWIR. This is done with the use of optical band-pass filters, like in the ULIS microbolometer of the MISTIGRI mission.

In contrast, there has been found only one research in dual-colour MWIR-LWIR microbolometers. The team of reference [106] developed a dual-band microbolometer based on a tunable micromirror located under the detector surface. The micromirror used the concept of a Fabry Perot cavity explained in Section 3.2.2.1.3. This micromirror device had the possibility to move between to positions in order to create two different Fabry Perot cavities and therefore to be MWIR and LWIR wavelength selectable.

In addition to this, there is one manufacturer specialized in customization of the microbolometers. The company is INO in Canada. This manufacturer has developed several dual-band LWIR microbolometers.

If the wideband Bird 640 Ceramic Packing BB is made dual-colour, it can be used for thermal LWIR operation in normal conditions, and eventually in the MWIR range when the ground temperature is very high.

Comparing with the Condor II multiband detector, the performance of the dual-colour Bird 640 Ceramic Packing BB microbolometer is lower. However, a microbolometer is considerably cheaper and smaller. Moreover, it does not require cooling. These are very positive properties for a CubeSat.

At the moment, there has not be developed any dual-band infrared CubeSat. As a result, it can be an astounding opportunity to be the first ones in developing a dual-band either photodetector o microbolometer CubeSat.

Chapter 8

Conclusions and future perspective

The main goal of this project was to study the different infrared detector technologies, their use in the space environment and their implementation in a CubeSat mission.

There are two main types of infrared detectors, photodetectors and thermal detectors. Photodetectors have a greater performance in terms of sensitivity, temperature resolution and signal-to-noise ratio compared with a thermal detector. However, the photodetectors have a huge disadvantage. They need to be cooled to temperatures lower than 150 K in order to operate. To do that, it is necessary to join the photodetector with a cooler. As a result, photodetectors have usually a large size what may suppose a limitation for small CubeSat designs. On the other hand, the thermal detectors operate at room temperatures, about 300 K, and therefore they do not need from an additional cooler. The photodetectors are also considerably more expensive than thermal detectors.

In this project, there have been defined two main bands of the infrared electromagnetic spectrum. The Mide-Wave Infrared Range (MWIR) from 3 μm to 5 μm, and the Long-Wave Infrared Range (LWIR) from 8 μm to 14 μm. The photodetectors are the main reference for the MWIR range, in contrast, in the LWIR range it is possible to find photodetectors and thermal detectors. For thermal imaging, the LWIR range is mainly used for high sensitivity remote sensing, since the peak of radiation coming from the Earth is within this band. On the other hand, the MWIR range is used in missions where the sensitivity is not the most important parameter besides observations of high-temperature objects. The radiation coming from the MWIR and LWIR band is also different depending on the atmospheric conditions and the weather.

There is a large number of materials used for infrared detectors. These detectors are commonly sensitive to only one band of the infrared radiation. At the moment,

the best photodetectors for the MWIR band, available at the market, are the HgCdTe, InSb and Type II Superlattices sensors, T2SL. This detectors have been used in several satellite missions. The major drawback is their low operational temperature. As a result, new materials and architectures have emerged offering very high performances at high temperatures in comparison with the three previously cited materials. Nevertheless, these technologies are not yet offered by the manufacturers, as it is the case of the promising quantum-dot infrared photodetectors. Therefore, they can not be considered for a near CubeSat mission. It is necessary to discard other detectors as the quantum-well infrared photodetectors due to its low quantum efficiency, about 10 %, incompatible with this mission.

For the LWIR band, the main detectors are the HgCdTe, T2SL and extrinsic photodetectors besides the microbolometer thermal detectors. All of them are available at the market and have also a large flight heritage in satellite missions. Again, other very promising technologies as the high-temperature superconducting bolometers cannot be considered for a near mission since they still in development.

But the most interesting technology analysed in this project is defined by the dual-band infrared detectors. These detectors are sensitive in two bands of the infrared electromagnetic radiation. This is the case of the impressive HgCdTe Condor II dual-band detector from the Italian manufacturer Leonardo, sensitive to the MWIR and LWIR band. However, this detector shares the drawback of the other photodetectors. It needs to be cooled at temperatures lower than 100 K in order to operate.

Another option covered in this project is to have a multispectral detector. The objective is to divide each of the wide bands MWIR and LWIR into several bands respectively, to possibly select the wavelengths of higher interest. In order to do this, in a snapshot satellite, the best option is to use a multispectral array of band-pass filters. On the other hand, for a scanning satellite besides the use of band-pass filters, it is also possible to use prisms, gratings and grisms. It has been cited how these band-pass filters can be used not only in single-band detectors but also in dual-band detectors.

The next step in the project was to test the performance of these detectors in the space environment. In order to do that, there was carried on a detailed study of the internal structure of the detectors.

The process to obtain a thermal image in photodetectors and thermal detectors is different. There are not only differences in the way in which the incoming radiation is

captured, but also in the read-out process of this radiation. To each step of the read-out, there is assigned a specific time constant. One of them is the response time. The response time was defined as the time to reach a 63 % of the final output value of the signal. While in photodetectors the response time is in the order of microseconds, in thermal detectors it is in the order of milliseconds. The time that the satellites take to pass over the target is known as satellite integration time. The problem encountered is that the response time of the thermal detectors was larger than the integration time of the satellites. As a result, a blurred image will be obtained, what is not compatible with the mission. The solution to this problem was found in a technique known as time delay integration. The purpose is to capture the signal coming from a specific ground target several times with different pixels of the detector. Therefore, in the end, the signal will be strong enough to have a proper thermal image. This can be done not only in CCD read-out architectures but also in CMOS architectures. One problem of this technique is that it requires very precise optics what may be an issue in small CubeSats.

The performance of photodetectors and thermal detectors is limited by the noise of their internal structure. However, the noise in photodetectors is considerably smaller than in thermal detectors. One of the achievements of this project was to test what will happen if a microbolometer thermal detector is passively cooled down in order to reduce the noise. It was tested to cool down a microbolometer from 300 K to 200 K. The result obtained showed that there is not an advantage in cooling down a microbolometer since their main noise, the flicker (1/f) noise, does not depend on the temperature of the detector.

The internal noise is related to the temperature resolution of the detector. This is defined by the Noise Equivalent Temperature Difference, NETD. It describes the minimum change in the temperature of two consecutive targets that can be detected by the thermal imager. This parameter is measured in the ground and it is in the order of a few millikelvins. The purpose of this project was to translate this measurement to the space environment, in order to know the temperature resolution of the imager once the satellite is in space. It can be stated that a model that allows computing these calculations has been developed in this project. This model was checked with the results of the future JEM-EUSO instrument for the International Space Station. In addition to this, the majority of the assumptions done were consulted contacting

directly with the main manufacturers of infrared detectors, Sofradir, Teledyne, FLIR and Xenics among others.

The conditions in which the different detectors are tested in the ground are indicated in the manufacturer data-sheets. The model developed in this project allows to compute: the temperature resolution of the detectors in space, the signal-to-noise ratio of the detector in the ground, the signal-to-noise ratio of the detector in space and the specific detectivity of the detector. This, for the different wavelength ranges and different materials of infrared detectors.

The model was tested with a total of 20 different detectors, including single-band MWIR or LWIR detectors, dual-band photodetectors and thermal wide band detectors. It was set a temperature resolution requisite of 0.4 K in space.

In the MWIR the best performances were achieved with the single-band HgCdTe HiPir Engine HOT detector from the German AIM, and the T2SL HOT Neutrino Swap C from the American FLIR. These photodetectors operate at a respective temperature of 160 K and 130 K. In addition to this, both of them are available in Europe.

In the LWIR band, it was demonstrated how it is not worth it to use a photodetector, since the 0.4 K temperature resolution requisite can be achieved with the microbolometers Bird 640 Ceramic Packing from the Israeli manufacturer SCD and the Pico 640 Gen 2 from the French manufacturer ULIS. Slightly better performances were achieved with the SCD detector.

For the multi-band MWIR-LWIR operation, the photodetector Condor II from the Italian manufacturer Leonardo was selected as the best option among the other multi-band photodetectors. Moreover, there has been a very positive contact with this manufacturer.

Finally, it was tested the powerful Bird 640 Ceramic Packing BB in its wideband version from the manufacturer SCD. This detector is sensitive to the 3μm to 14 μm band. A microbolometer cannot distinguish between the radiation coming from the different wavelengths in contrast with photodetectors. Therefore, it will be necessary to use a filter to either the MWIR or the LWIR band. After the calculations, it was seen how this detector accomplished the temperature requisites with a band-pass filter in the LWIR. However, this requisites there were not achieved with a filter for the MWIR band. Nevertheless, a microbolometer for the MWIR band can be very useful to observe high-temperature objects. A dual-band microbolometer, half for the

MWIR half for the LWIR, will be an astounding opportunity to do something never done in a CubeSat.

As a remark, the future work in the topic has to be oriented into a deep research of the time delay integration techniques besides to extend the model of the temperature resolution for a wider wavelength range.

In this project, it has been demonstrated the feasibility of an optical instrument including an infrared detector capturing light from two bands. The use of either a dual-band photodetector or a dual-band microbolometer will be a revolution for science demonstration in a CubeSat. It can be the first CubeSat mission of these characteristics, and, therefore, it is clear that it will be a huge success.

Appendix A

Performance of the different detectors for the infrared

This Appendix includes the computed values of the Noise Equivalent Temperature Difference, NETD, and the signal-to-noise ratio, SNR, for the detectors available in the market that can be used in a CubeSat. The explanation of all the results obtained is included in Chapter 7 of this document.

Manufacturer	**Detector Name**	**Material FPA**	**λ range**	**Size FPA (pixel x pixel)**	**Pixel pitch**	**NEDT**	**F number**	**FPA T**
Sofradir (France)	LEO-LP MW	HgCdTe	3.7 μm to 4.8 μm	640 x 512	15 μm	20 mK 293 K	F/5.5	110 K
AIM (Germany)	HiPIR-Engine HOT	HgCdTe	3.4 μm to 4.8 μm	1024 x 768	10 μm	25 mK 300 K	F/2.2	160 K
Leonardo (Italy/UK)	HOT Hawk	HgCdTe	3 μm to 5 μm	640 x 512	16 μm	17 mK	F/2.8	80 K up to 175K
Leonardo (Italy/UK)	SuperHawk	HgCdTe	3.7 μm to 4.95 μm	1280 x 1024	8 μm	20 mK	F/2.8	>110 K
SCD (Israel)	Pelican-D JT 640	InSb	3.6 μm to 4.9 μm	640 x 512	15 μm	20 mK	F/3	80 K
SCD (Israel)	Kinglet 640 SLC	XBn	3.6 μm to 4.2 μm	640 x 512	15 μm	23 mK	F/2.5	150 K
SCD (Israel)	Mini Blackbird 1280	XBn	3.6 μm to 4.2 μm	1280 x 1024	10 μm	<25 mK	F/3.4	150 K
FLIR (USA) Available for Europe	HOT Neutrino Swap C	T2SL	3.4 μm to 5.0 μm	640 x 512	15 μm	<25 mK	F/5.5	130 K
iRNova (Sweeden)	IRnova Dag MW	T2SL	3,7 μm to 5,1 μm	640 x 512	15 μm	20 mK	F/4	80 K

Table A.1: Specifications of the different single-band MWIR detectors. [37] [5] [38] [32]

Detector	**λ range [μm] F/number**	**Detectivity [W^{-1}]**	**NETD space 272 K (K)**	**SNR ground 280 K**	**SNR space 272 K**	**Specific detectivity, D* [m·Hz$^{1/2}$/W]**
LEO-LP MW	3.7 to 4.8 F/5.5	$4.6{\cdot}10^{14}$	-	861.8	-	$4.43{\cdot}10^{7}$
	4.4 to 4.8 F/5.5	$4.6{\cdot}10^{14}$	0.007	490.9	188.4	$4.43{\cdot}10^{7}$
HiPIR-Engine HOT	3.4 to 4.8 F/2.2	$9.7{\cdot}10^{13}$	-	541.6	-	$2.47{\cdot}10^{8}$
	4.4 to 4.8 F/2.2	$9.7{\cdot}10^{13}$	0.071	291.6	17.9	$2.47{\cdot}10^{8}$
HOT Hawk	3 to 5 F/2.8	$6.7{\cdot}10^{13}$	-	830.8	-	$1.03{\cdot}10^{8}$
	4.4 to 5 F/2.8	$6.7{\cdot}10^{13}$	0.024	543.9	31.48	$1.03{\cdot}10^{8}$
SuperHawk	3.7 to 4.95 F/2.8	$2.7{\cdot}10^{14}$	-	723	-	$2.07{\cdot}10^{8}$
	4.4 to 4.95 F/2.8	$2.7{\cdot}10^{14}$	0.027	483.3	31.55	$2.07{\cdot}10^{8}$
Pelican-D JT 640	3.6 to 4.9 F/3	$9.1{\cdot}10^{13}$	-	707.1	-	$1.0{\cdot}10^{8}$
	4.4 to 4.9 F/3	$9.1{\cdot}10^{13}$	0.026	443	37.77	$1.0{\cdot}10^{8}$
Kinglet 640 SLC	3.6 to 4.2 F/2.5	$2.0{\cdot}10^{13}$	0.022	501.2	-	$4.57{\cdot}10^{8}$
Mini Blackbird 1280	3.6 to 4.2 F/3.4	$7.7{\cdot}10^{14}$	0.013	461.1	-	$3.41{\cdot}10^{8}$
HOT Neutrino Swap C	3.4 to 5.0 F/5.5	$2.1{\cdot}10^{14}$	-	573.7	-	$2.0{\cdot}10^{7}$
	4.4 to 5.0 F/5.5	$2.1{\cdot}10^{14}$	0.009	382.8	85.48	$2.0{\cdot}10^{7}$
IRnova Dag MW	3,7 to 5,1 F/4	$1.3{\cdot}10^{14}$	-	752.1	-	$4.44{\cdot}10^{7}$
	4.4 to 5.1 F/4	$1.3{\cdot}10^{14}$	0.012	555.8	52.72	$4.44{\cdot}10^{7}$

Table A.2: Results obtained for the single-band MWIR detectors at 280 K.

Detector	**λ range (μm) F/number**	**Detectivity [W^{-}1]**	**NETD space 291 K (K)**	**SNR ground 300 K**	**SNR space 291 K**	**Specific detectivity, D* (m·Hz$^{1/2}$/W)**
LEO-LP MW	3.7 to 4.8 F/5.5	$4.6{\cdot}10^{14}$	-	1885	-	$4.43{\cdot}10^{7}$
	4.4 to 4.8 F/5.5	$4.6{\cdot}10^{14}$	0.004	1031	405.3	$4.43{\cdot}10^{7}$
HiPIR-Engine HOT	3.4 to 4.8 F/2.2	$9.7^{*}{\cdot}10^{13}$	-	1197	-	$2.47{\cdot}10^{8}$
	4.4 to 4.8 F/2.2	$9.7^{*}{\cdot}10^{13}$	0.039	612.7	38.52	$2.47{\cdot}10^{8}$
HOT Hawk	3 to 5 F/2.8	$6.7{\cdot}10^{13}$	-	1801	-	$1.03{\cdot}10^{8}$
	4.4 to 5 F/2.8	$6.7{\cdot}10^{13}$	0.013	1122	67.73	$1.03{\cdot}10^{8}$
SuperHawk	3.7 to 4.95 F/2.8	$2.7{\cdot}10^{14}$	-	1553	-	$2.07{\cdot}10^{8}$
	4.4 to 4.95 F/2.8	$2.7{\cdot}10^{14}$	0.015	1002	67.88	$2.07{\cdot}10^{8}$
Pelican-D JT 640	3.6 to 4.9 F/3	$9.1{\cdot}10^{13}$	-	1534	-	$1.0{\cdot}10^{8}$
	4.4 to 4.9 F/3	$9.1{\cdot}10^{13}$	0.014	922.3	81.25	$1.0{\cdot}10^{8}$
Kinglet 640 SLC	3.6 to 4.2 F/2.5	$2.0{\cdot}10^{14}$	0.011	1193	-	$4.57{\cdot}10^{8}$
Mini Blackbird 1280	3.6 to 4.2 F/3.4	$7.7{\cdot}10^{14}$	0.006	1097	-	$3.41{\cdot}10^{8}$
HOT Neutrino SWAP C	3.4 to 5.0 F/5.5	$2.1{\cdot}10^{14}$	-	1236	-	$2.0{\cdot}10^{7}$
	4.4 to 5.0 5.5	$2.1{\cdot}10^{14}$	0.005	789.9	183.9	$2.0{\cdot}10^{7}$
IRnova Dag MW	3.7 to 5.1 F/4	$1.3{\cdot}10^{14}$	-	1588	-	$4.44{\cdot}10^{7}$
	4.4 to 5.1 F/4	$1.3{\cdot}10^{14}$	0.007	1137	113.4	$4.44{\cdot}10^{7}$

Table A.3: Results obtained for the single-band MWIR detectors at 300 K.

Detector	**λ range (μm) F/number**	**Detectivity [W^{-}1]**	**NETD space 310 K (K)**	**SNR ground 320 K**	**SNR space 310 K**	**Specific detectivity, D* (m·Hz$^{1/2}$/W)**
LEO-LP MW	3.7 to 4.8 F/5.5	$4.6{\cdot}10^{14}$	-	3747	-	$4.43{\cdot}10^{7}$
	4.4 to 4.8 F/5.5	$4.6{\cdot}10^{14}$	0.002	1976	792.3	$4.43{\cdot}10^{7}$
HiPIR-Engine HOT	3.4 to 4.8 F/2.2	$9.7^{*}{\cdot}10^{13}$	-	2406	-	$2.47{\cdot}10^{8}$
	4.4 to 4.8 F/2.2	$9.7^{*}{\cdot}10^{13}$	0.023	1174	75.3	$2.47{\cdot}10^{8}$
HOT Hawk	3 to 5 F/2.8	$6.7{\cdot}10^{13}$	-	3567	-	$1.03{\cdot}10^{8}$
	4.4 to 5 F/2.8	$6.7{\cdot}10^{13}$	0.008	2117	132.4	$1.03{\cdot}10^{8}$
SuperHawk	3.7 to 4.95 F/2.8	$2.7{\cdot}10^{14}$	-	3041	-	$2.07{\cdot}10^{8}$
	4.4 to 4.95 F/2.8	$2.7{\cdot}10^{14}$	0.009	1897	132.7	$2.07{\cdot}10^{8}$
Pelican-D JT 640	3.6 to 4.9 F/3	$9.1{\cdot}10^{13}$	-	3029	-	$1.0{\cdot}10^{8}$
	4.4 to 4.9 F/3	$9.1{\cdot}10^{13}$	0.008	1753	158.8	$1.0{\cdot}10^{8}$
Kinglet 640 SLC	3.6 to 4.2 F/2.5	$2.0{\cdot}10^{14}$	0.006	2250	-	$4.57{\cdot}10^{8}$
Mini Blackbird 1280	3.6 to 4.2 F/3.4	$7.7{\cdot}10^{14}$	0.003	2346	-	$3.41{\cdot}10^{8}$
HOT Neutrino SWAP C	3.4 to 5.0 F/5.5	$2.1{\cdot}10^{14}$	-	2431	-	$2.0{\cdot}10^{7}$
	4.4 to 5.0 5.5	$2.1{\cdot}10^{14}$	0.003	1490	359.5	$2.0{\cdot}10^{7}$
IRnova Dag MW	3.7 to 5.1 F/4	$1.3{\cdot}10^{14}$	-	3065	-	$4.44{\cdot}10^{7}$
	4.4 to 5.1 F/4	$1.3{\cdot}10^{14}$	0.004	2128	221.7	$4.44{\cdot}10^{7}$

Table A.4: Results obtained for the single-band MWIR detectors at 320 K.

Manufacturer	**Detector Name**	**Material FPA**	**λ range**	**Size FPA (pixel x pixel)**	**Pixel pitch**	**NEDT**	**F number**	**FPA T°**
AIM (Germany)	HiPIR-640 LW	HgCdTe	7.6 μm to 9.0 μm	640 x 512	15 μm	30 mK	F/2.05	70 K
Leonardo (Italy/ UK)	Hawk LW	HgCdTe	8 μm to 10 μm	640 x 512	16 μm	32 mK	F/2	Up to 90K
SCD (Israel)	Pelican-D LW STD	T2SL	9.3 μm cut-off	640 x 512	15 μm	15 mK	F/1.6	<100 K
SCD (Israel)	Bird 640 Metallic Packaging STD	VOx Micro-bolometer with TEC	8 μm to 14 μm	640 x 480	17 μm	<50 mK	F/1	300 K
SCD (Israel)	Bird 640 Ceramic Packaging HS	VOx Micro-bolometer TEC-less	8 μm to 14 μm	640 x 480	17 μm	<35 mK	F/1	300 K
ULIS (France)	Pico1024 Gen2	a-Si micro-bolometer TEC-less	8 μm to 14 μm	1024 x 768	17 μm	<50 mK	F/1	300 K
ULIS (France)	Pico 640 Gen 2	a-Si micro-bolometer TEC-less	8 μm to 14 μm	640 x 480	17 μm	<40 mK	F/1	300 K

Table A.5: Specifications of the different single-band LWIR detectors. [37] [5] [38] [11]

Detector	**λ range (μm) F/number**	**Detectivity W^{-1}**	**NETD space 279 K (K)**	**SNR ground 280 K**	**SNR space 279 K**	**Specific detectivity, D ($m \cdot Hz^{1/2}/W$)**
HiPIR-640 LW	7.6 to 9.0 F/2.05	$6.2 \cdot 10^{12}$	0.023	2040	-	$3.12 \cdot 10^{7}$
Hawk LW	8 to 10 F/2	$3.5 \cdot 10^{12}$	0.025	1323	1929	$2.09 \cdot 10^{7}$
Pelican-D LW STD	8 to 9.3 F/1.6	$8.2 \cdot 10^{12}$	0.019	2681	2863	$1.12 \cdot 10^{8}$
Bird 640 Metallic Packaging STD	8 to 14 F/1	$2.1 \cdot 10^{11}$	0.150	1053	403.3	$2.094 \cdot 10^{7}$
	8 to 10 F/1	$2.1 \cdot 10^{11}$	0.380	351.6	128.2	$2.094 \cdot 10^{7}$
	10 to 12 F/1	$2.1 \cdot 10^{11}$	0.440	368.5	163	$2.094 \cdot 10^{7}$
Bird 640 Ceramic Packaging HS	8 to 14 F/1	$2.9 \cdot 10^{11}$	0.105	1504	576.1	$2.99 \cdot 10^{7}$
	8 to 10 F/1	$2.9 \cdot 10^{11}$	0.266	502.3	183.1	$2.99 \cdot 10^{7}$
	10 to 12 F/1	$2.9 \cdot 10^{11}$	0.307	526.5	232.8	$2.99 \cdot 10^{7}$
Pico1024 Gen2	8 to 14 F/1	$1.8 \cdot 10^{11}$	0.150	1053	403.03	$1.96 \cdot 10^{7}$
	8 to 10 F/1	$1.8 \cdot 10^{11}$	0.380	351.6	128.8	$1.96 \cdot 10^{7}$
	10 to 12 F/1	$1.8 \cdot 10^{11}$	0.440	368.5	163	$1.96 \cdot 10^{7}$
Pico 640 Gen 2	8 to 14 F/1	$2.3 \cdot 10^{11}$	0.120	1316	504.1	$2.45 \cdot 10^{7}$
	8 to 10 F/1	$2.3 \cdot 10^{11}$	0.304	439.5	160.2	$2.45 \cdot 10^{7}$
	10 to 12 F/1	$2.3 \cdot 10^{11}$	0.351	460.7	203.7	$2.45 \cdot 10^{7}$

Table A.6: Results obtained for the single-band LWIR detectors at 280 K.

Detector	**λ range (μm) F/number**	**Detectivity W^{-1}**	**NETD space 299 K (K)**	**SNR ground 300 K**	**SNR space 299 K**	**Specific detectivity, D ($m \cdot Hz^{1/2}/W$)**
HiPIR-640 LW	7.6 to 9.0 F/2.05	$6.2 \cdot 10^{12}$	0.018	2799	-	$3.12 \cdot 10^{7}$
Hawk LW	8 to 10 F/2	$3.5 \cdot 10^{12}$	0.020	1940	2838	$2.09 \cdot 10^{7}$
Pelican-D LW STD	8 to 9.3 F/1.6	$8.2 \cdot 10^{12}$	0.014	3989	4258	$1.12 \cdot 10^{8}$
Bird 640 Metallic Packaging STD	8 to 14 F/1	$2.1 \cdot 10^{11}$	0.123	1457	559.6	$2.094 \cdot 10^{7}$
	8 to 10 F/1	$2.1 \cdot 10^{11}$	0.300	515.6	188.5	$2.094 \cdot 10^{7}$
	10 to 12 F/1	$2.1 \cdot 10^{11}$	0.369	505.5	223.5	$2.094 \cdot 10^{7}$
Bird 640 Ceramic Packaging HS	8 to 14 F/1	$2.9 \cdot 10^{11}$	0.086	2081	799.4	$2.99 \cdot 10^{7}$
	8 to 10 F/1	$2.9 \cdot 10^{11}$	0.207	736.6	269.4	$2.99 \cdot 10^{7}$
	10 to 12 F/1	$2.9 \cdot 10^{11}$	0.256	722.2	319.3	$2.99 \cdot 10^{7}$
Pico1024 Gen2	8 to 14 F/1	$1.8 \cdot 10^{11}$	0.123	1457	559.6	$1.96 \cdot 10^{7}$
	8 to 10 F/1	$1.8 \cdot 10^{11}$	0.296	515.6	188.5	$1.96 \cdot 10^{7}$
	10 to 12 F/1	$1.8 \cdot 10^{11}$	0.369	505.5	223.5	$1.96 \cdot 10^{7}$
Pico 640 Gen 2	8 to 14 F/1	$2.3 \cdot 10^{11}$	0.098	1821	600.4	$2.45 \cdot 10^{7}$
	8 to 10 F/1	$2.3 \cdot 10^{11}$	0.237	644.5	235.7	$2.45 \cdot 10^{7}$
	10 to 12 F/1	$2.3 \cdot 10^{11}$	0.293	631.9	279.4	$2.45 \cdot 10^{7}$

Table A.7: Results obtained for the single-band LWIR detectors at 300 K.

Detector	**λ range (μm) F/number**	**Detectivity W^{-1}**	**NETD space 319 K (K)**	**SNR ground 320 K**	**SNR space 319 K**	**Specific detectivity, D ($m \cdot Hz^{1/2}/W$)**
HiPIR-640 LW	7.6 to 9.0 F/2.05	$6.2 \cdot 10^{12}$	0.014	3695	-	$3.12 \cdot 10^{7}$
Hawk LW	8 to 10 F/2	$3.5 \cdot 10^{12}$	0.016	2715	3982	$2.09 \cdot 10^{7}$
Pelican-D LW STD	8 to 9.3 F/1.6	$8.2 \cdot 10^{12}$	0.016	5652	6031	$1.12 \cdot 10^{8}$
Bird 640 Metallic Packaging STD	8 to 14 F/1	$2.1 \cdot 10^{11}$	0.104	1942	747.4	$2.094 \cdot 10^{7}$
	8 to 10 F/1	$2.1 \cdot 10^{11}$	0.240	721.6	264.6	$2.094 \cdot 10^{7}$
	10 to 12 F/1	$2.1 \cdot 10^{11}$	0.319	667.4	295.1	$2.094 \cdot 10^{7}$
Bird 640 Ceramic Packaging HS	8 to 14 F/1	$2.9 \cdot 10^{11}$	0.073	2775	1068	$2.99 \cdot 10^{7}$
	8 to 10 F/1	$2.9 \cdot 10^{11}$	0.168	1031	378	$2.99 \cdot 10^{7}$
	10 to 12 F/1	$2.9 \cdot 10^{11}$	0.220	953.5	421.6	$2.99 \cdot 10^{7}$
Pico1024 Gen2	8 to 14 F/1	$1.8 \cdot 10^{11}$	0.104	1942	747.4	$1.96 \cdot 10^{7}$
	8 to 10 F/1	$1.8 \cdot 10^{11}$	0.240	721.6	264.6	$1.96 \cdot 10^{7}$
	10 to 12 F/1	$1.8 \cdot 10^{11}$	0.314	667.4	295.1	$1.96 \cdot 10^{7}$
Pico 640 Gen 2	8 to 14 F/1	$2.3 \cdot 10^{11}$	0.083	2428	934.2	$2.45 \cdot 10^{7}$
	8 to 10 F/1	$2.3 \cdot 10^{11}$	0.192	902	330.8	$2.45 \cdot 10^{7}$
	10 to 12 F/1	$2.3 \cdot 10^{11}$	0.251	834.3	368.9	$2.45 \cdot 10^{7}$

Table A.8: Results obtained for the single-band LWIR detectors at 320 K.

Manufacturer	**Detector Name**	**Material FPA**	**λ range**	**Size FPA (pixel x pixel)**	**Pixel pitch**	**NEDT**	**F number**	**FPA T**
Leonardo (Italy/UK)	Condor II Dual - Waveband Infrared detector	HgCdTe	3 μm to 5 μm Single-band mode	640 x 512	24 μm	11 mK	F/1.84 (From drawing)	80 K
			8 μm to 10 μm Single-band mode			22 mK		
			3 μm to 5 μm Dual-band mode			28 mK		
			8 μm to 10 μm Dual-band mode			28 mK		
AIM (Germany)	AIM Dual-color	T2SL	3.4 μm to 4.4 μm	384 x 288	40 μm	35 mK	F/2.0	77 K
			4.4 μm to 5.0 μm			25 mK		
QimagiQ (USA)	Eagle 256	QWIP	4.3 μm to 5.3 μm	320x256	40 μm	40 mK	F/2.3	68K
			8.2 μm to 9 μm			30 mK		

Table A.9: Specifications of the different dual-band detectors. [37] [39] [38]

Detector	**λ range (μm) F/number**	**Detectivity (W^{-1})**	**NETD space (280 K x GE) (K)**	**SNR ground 280 K**	**SNR space (280 K x GE)**	**Specific detectivity, D^* ($m \cdot Hz^{1/2}/W$)**
Condor II Dual-Waveband Infrared detector	4.4 to 5 F/1.84	$1.98 \cdot 10^{13}$	0.036	840.6	21.01	$2.46 \cdot 10^{8}$
	8 to 10 F/1.84	$1.93 \cdot 10^{12}$	0.020	1924	2375	$2.40 \cdot 10^{7}$
	Dual band F/1.84 4.4 to 5	$7.8 \cdot 10^{12}$	0.092	330.3	8.254	$9.68 \cdot 10^{7}$
	Dual band F/1.84 8 to 10	$1.51 \cdot 10^{12}$	0.026	1512	1866	$1.88 \cdot 10^{7}$
AIM Dual-color	3.4 to 4.4 F/2.0	$6.88 \cdot 10^{12}$	-	342	-	$1.02 \cdot 10^{8}$
	4.4 to 5.0 F/2.0	$6.4 \cdot 10^{12}$	0.040	636.8	18.8	$9.48 \cdot 10^{7}$
Eagle 256	4.4 to 5.3 F/2.3	$2.9 \cdot 10^{12}$	0.051	396.8	8.543	$2.46 \cdot 10^{7}$
	8.2 to 9 F/2.3	$1.93 \cdot 10^{12}$	0.018	1331	2964	$1.64 \cdot 10^{7}$

Table A.10: Results obtained for the dual-band detectors at 280 K.

Detector	**λ range (μm) F/number**	**Detectivity (W^{-1})**	**NETD space (300 K x GE) (K)**	**SNR ground 300 K**	**SNR space (300 K x GE)**	**Specific detectivity, D^* ($m \cdot Hz^{1/2}/W$)**
Condor II Dual-Waveband Infrared detector	4.4 to 5 F/1.84	$1.98 \cdot 10^{13}$	0.020	1735	45.2	$2.46 \cdot 10^{8}$
	8 to 10 F/1.84	$1.93 \cdot 10^{12}$	0.016	2822	3494	$2.40 \cdot 10^{7}$
	Dual band F/1.84 4.4 to 5	$7.8 \cdot 10^{12}$	0.051	681.5	17.76	$9.68 \cdot 10^{7}$
	Dual band F/1.84 8 to 10	$1.51 \cdot 10^{12}$	0.020	2217	2745	$1.88 \cdot 10^{7}$
AIM Dual-color	3.4 to 4.4 F/2.0	$6.88 \cdot 10^{12}$	-	799.5	-	$1.02 \cdot 10^{8}$
	4.4 to 5.0 F/2.0	$6.4 \cdot 10^{12}$	0.022	1314	40.45	$9.48 \cdot 10^{7}$
Eagle 256	4.4 to 5.3 F/2.3	$2.9 \cdot 10^{12}$	0.029	797.4	18.38	$2.46 \cdot 10^{7}$
	8.2 to 9 F/2.3	$1.93 \cdot 10^{12}$	0.014	1984	4420	$1.64 \cdot 10^{7}$

Table A.11: Results obtained for the dual-band detectors at 300 K.

Detector	**λ range (μm) F/number**	**Detectivity (W^{-1})**	**NETD space (320 K x GE) (K)**	**SNR ground 320 K**	**SNR space (320 K x GE)**	**Specific detectivity, D^* ($m \cdot Hz^{1/2}/W$)**
Condor II Dual-Waveband Infrared detector	4.4 to 5 F/1.84	$1.98 \cdot 10^{13}$	0.012	3272	88.36	$2.46 \cdot 10^{8}$
	8 to 10 F/1.84	$1.93 \cdot 10^{12}$	0.013	3949	4903	$2.40 \cdot 10^{7}$
	Dual band F/1.84 4.4 to 5	$7.8 \cdot 10^{12}$	0.030	1285	34.71	$9.68 \cdot 10^{7}$
	Dual band F/1.84 8 to 10	$1.51 \cdot 10^{12}$	0.016	3103	3852	$1.88 \cdot 10^{7}$
AIM Dual-color	3.4 to 4.4 F/2.0	$6.88 \cdot 10^{12}$	-	1685	-	$1.02 \cdot 10^{8}$
	4.4 to 5.0 F/2.0	$6.4 \cdot 10^{12}$	0.014	2478	79.8	$9.48 \cdot 10^{7}$
Eagle 256	4.4 to 5.3 F/2.3	$2.9 \cdot 10^{12}$	0.018	1470	35.93	$2.46 \cdot 10^{7}$
	8.2 to 9 F/2.3	$1.93 \cdot 10^{12}$	0.011	2817	6273	$1.64 \cdot 10^{7}$

Table A.12: Results obtained for the dual-band detectors at 320 K.

Manufacturer	**Detector Name**	**Material FPA**	λ	**Size FPA (pixel x pixel)**	**Pixel pitch**	**NEDT**	**F/**	**FPA T**
SCD (Israel)	Bird 640 Ceramic Packaging BB Wide-Band	VOx Micro-bolometer TEC-less	3 μm to 14 μm	640 x 480	17 μm	35 mK	F/1	300 K

Table A.13: Specifications of the wide band Bird 640 Ceramic Packing BB from [5]

Detector	**λ range (μm) F/number**	**Detectivity (W^{-1})**	**NETD space (280 K x GE) (K)**	**SNR ground 280 K**	**SNR space (280 K x GE)**	**Specific detectivity, D^* ($m \cdot Hz^{1/2}/W$)**
Bird 640 Ceramic Packaging BB Wide-Band	8 to 14 F/1	$1.84 \cdot 10^{11}$	0.169	931.5	356.8	$1.85 \cdot 10^{7}$
	8 to 10 F/1	$1.84 \cdot 10^{11}$	0.429	311.1	113.4	$1.85 \cdot 10^{7}$
	10 to 12 F/1	$1.84 \cdot 10^{11}$	0.496	326.1	144.2	$1.85 \cdot 10^{7}$
	3 to 5 F/1	$1.84 \cdot 10^{11}$	-	20.2	-	$1.85 \cdot 10^{7}$
	4.4 to 5.4 F/1	$1.84 \cdot 10^{11}$	3.827	28.29	0.1	$1.85 \cdot 10^{7}$
	4.4 to 5.2 F/1	$1.84 \cdot 10^{11}$	5.266	20.05	0.1	$1.85 \cdot 10^{7}$

Table A.14: Results obtained for the wide band Bird 640 Ceramic Packing BB at 280 K.

Detector	**λ range (μm) F/number**	**Detectivity (W^{-1})**	**NETD space (300 K x GE) (K)**	**SNR ground 300 K**	**SNR space (300 K x GE)**	**Specific detectivity, D^* ($m \cdot Hz^{1/2}/W$)**
Bird 640 Ceramic Packaging BB Wide-Band	8 to 14 F/1	$1.84 \cdot 10^{11}$	0.139	1289	495.1	$1.85 \cdot 10^{7}$
	8 to 10 F/1	$1.84 \cdot 10^{11}$	0.335	456.3	166.8	$1.85 \cdot 10^{7}$
	10 to 12 F/1	$1.84 \cdot 10^{11}$	0.413	447.3	197.8	$1.85 \cdot 10^{7}$
	3 to 5 F/1	$1.84 \cdot 10^{11}$	-	43.79	-	$1.85 \cdot 10^{7}$
	4.4 to 5.4 F/1	$1.84 \cdot 10^{11}$	2.2	56.36	0.21	$1.85 \cdot 10^{7}$
	4.4 to 5.2 F/1	$1.84 \cdot 10^{11}$	2.977	40.65	0.20	$1.85 \cdot 10^{7}$

Table A.15: Results obtained for the wide band Bird 640 Ceramic Packing BB at 300 K.

Detector	**λ range (μm) F/number**	**Detectivity (W^{-1})**	**NETD space (320 K x GE) (K)**	**SNR ground 320 K**	**SNR space (320 K x GE)**	**Specific detectivity, D^* ($m \cdot Hz^{1/2}/W$)**
Bird 640 Ceramic Packaging BB Wide-Band	8 to 14 F/1	$1.84 \cdot 10^{11}$	0.118	1719	661.4	$1.85 \cdot 10^{7}$
	8 to 10 F/1	$1.84 \cdot 10^{11}$	0.271	638.5	234.1	$1.85 \cdot 10^{7}$
	10 to 12 F/1	$1.84 \cdot 10^{11}$	0.355	590.6	261.1	$1.85 \cdot 10^{7}$
	3 to 5 F/1	$1.84 \cdot 10^{11}$	-	86.72	-	$1.85 \cdot 10^{7}$
	4.4 to 5.4 F/1	$1.84 \cdot 10^{11}$	1.365	103.2	0.410	$1.85 \cdot 10^{7}$
	4.4 to 5.2 F/1	$1.84 \cdot 10^{11}$	1.821	75.51	0.410	$1.85 \cdot 10^{7}$

Table A.16: Results obtained for the wide band Bird 640 Ceramic Packing BB at 320 K.

References

[1] J. Loicq, "Space experiment development," Lectures from the University of Lige.

[2] A. Rogalski, M. Kopytko, and P. Martyniuk, *Antimonide-based Infrared Detectors: A New Perspective*, 1st ed. SPIE, Apr. 2018, iSBN: 978-1-5106-1140-5.

[3] A. Rogalski, *Infrared and Terahertz Detectors*, 3rd ed. CRC Press, Taylor & Francis Group, Dec. 2018, iSBN: 9781138198005.

[4] "Valence and conduction bands," Apr. 2019, wikipedia, accessed: 2019. [Online]. Available: https://en.wikipedia.org/wiki/Valence_and_conduction_bands

[5] "Infrared cooled and uncooled detectors." semi Conductor Devices | SCD, accessed: 2019. [Online]. Available: http://www.scd.co.il/

[6] A. Rogalski, *Infrared detectors*, 2nd ed. FL, USA: CRC Press, Taylor & Francis Group, 2011, iSBN: 978-1-4200-7671-4.

[7] A. Rogalski and D. A. Huckridge, "Next decade in infrared detectors," in *Electro-Optical and Infrared Systems: Technology and Applications XIV*. Warsaw, Poland: SPIE, Oct. 2017, p. 100, doi: 10.1117/12.2300779.

[8] A. Jain and A. Banerjee, "Design, development, characterization and qualification of infrared focal plane area array detectors for space-borne imaging applications," in *Earth Observing Missions and Sensors: Development, Implementation, and Characterization IV*, vol. 9881. International Society for Optics and Photonics, May 2016, doi: 10.1117/12.2222994.

[9] A. Traylor, "What is an Integrated Detector Assembly?" College of Optical Sciences, The University of Arizona, Aug. 2010, accessed: 2019. [Online]. Available: https://wp.optics.arizona.edu/optomech/wp-content/uploads/sites/53/2016/10/Traylor_What-is-an-IDA_Traylor.pdf

[10] "Handbook of thermal detectors." resources HAMAMATSU, accessed: 2019. [Online]. Available: https://www.hamamatsu.com/resources/pdf/ssd/e07_handbook_Thermal_detectors.pdf

[11] "ULIS IR | Experience Infrared, Thermal Image and Activity Sensors," accessed: 2019. [Online]. Available: https://www.ulis-ir.com/

[12] A. Rogalski, J. Antoszewski, and L. Faraone, "Third-generation infrared photodetector arrays," *Journal of Applied Physics*, vol. 105, no. 9, May 2009, doi: 10.1063/1.3099572.

[13] M. Clark, "Imaging Systems for CubeSats," 2018, accessed: 2019. [Online]. Available: https://cubesats.gsfc.nasa.gov/symposiums/2018/presentations/Day1/1415_Clark.pdf

[14] N. Hagen and M. W. Kudenov, "Review of snapshot spectral imaging technologies," *Optical Engineering*, vol. 52, no. 9, Sep. 2013, doi: 10.1117/1.OE.52.9.090901.

[15] "Multispectral imaging technology," spectral Devices Inc., accessed: 2019. [Online]. Available: https://www.spectraldevices.com/content/multispectral-imaging-technology

[16] P.-J. Lapray, X. Wang, J.-B. Thomas, and P. Gouton, "Multispectral Filter Arrays: Recent Advances and Practical Implementation," *Sensors*, vol. 14, no. 11, Nov. 2014, doi: 10.3390/s141121626.

[17] R. Le Goff, P. Etcheto, F. Tanguy, and P. Fuss, "Technological development of multispectral filter assemblies for micro bolometer," in *International Conference on Space Optics ICSO 2012*. Ajaccio, Corsica, France: SPIE, Nov. 2017, doi: 10.1117/12.2309068.

[18] T. D. Rahmlow, Jr., J. E. Lazo-Wasem, S. Wilkinson, and F. Tinker, "Filters for dual band infrared imagers," Orlando, Florida, USA, May 2009, doi: 10.1117/12.820059.

[19] M. Ebermann, N. Neumann, K. Hiller, E. Gittler, M. Meinig, and S. Kurth, "Widely tunable Fabry-Perot filter based MWIR and LWIR microspectrometers," M. A. Druy and R. A. Crocombe, Eds., Baltimore, Maryland, USA, May 2012, doi: 10.1117/12.919169.

[20] Y. Hang, "Time-Delay-Integration CMOS Image Sensor Design For Space Applications," Ph.D. dissertation, Nanyang Technological University, School of Electrical and Electronic Engineering. [Online]. Available: http://www.ntu.edu.sg/home/eechenss/Papers/Thesis-2016_Time-Delay-Integration%20CMOS%20Image%20Sensor%20Design%20For%20Space%20Applications.pdf

[21] M. Kohin and N. R. Butler, "Performance limits of uncooled VO x microbolometer focal plane arrays," B. F. Andresen and G. F. Fulop, Eds., Orlando, FL, Aug. 2004, p. 447, doi: 10.1117/12.542482.

[22] M. Loose, A. Hoffman, and V. Suntharalingam, "CMOS Detector Technology," raytheon, Rockwell scientific, MIT Lincoln Laboratory. [Online]. Available: https://slideplayer.com/slide/5041189/

[23] F. Tint Garcia-Moreno, G. Fargant, F. Guerin, C. Israbian, J. C. Mathieu, J. Michaud, A. Bardoux, O. Hagolle, and J. P. Lagouarde, "MISTIGRI instrumental concept for high-resolution thermal infrared imaging," M. Strojnik, Ed., San Diego, CA, Aug. 2009, doi: 10.1117/12.825637.

[24] A. Daniels, *Field guide to infrared systems, detectors, and FPAs*, 2nd ed., ser. SPIE field guides. Bellingham , Wash: SPIE Press, 2010, iSBN: 978-0-8194-8080-4.

[25] "Infrared cameras for thermal imaging in ground." hope Wish Photoelectronics Technology Co., Ltd. Accessed: 2019. [Online]. Available: http://www.chinahpws.com/en/

[26] "What is NETD in a Thermal Camera?" moviTHERM, accessed: 2019. [Online]. Available: http://movitherm.com/knowledgebase/netd-thermal-camera/

[27] G. Gaussorgues, *La Thermographie infrarouge : Principes, technologies, applications*, 2nd ed. Technique et documentation, 1984, iSBN: 2852062380.

[28] F. Corts, S. Briz, A. de Castro, I. Fernndez, S. Snchez, J. Melndez, and F. Lpez, "NETD estimation for microbolometer technology. JEM-EUSO IR CAM." accessed: 2019. [Online]. Available: http://spas.uah.es/index.php?option=com_content&view=article&id=100&Itemid=235&dir=JSROOT/jemeuso_national/2011-SRR&download_file=JSROOT/jemeuso_national/2011-SRR/Netd+Estimaton+for+Microbolomer+Technology.pdf

[29] "Geometrical definition of a thermal imager." center for Geospatial Analytics, accessed: 2019. [Online]. Available: https://cnr.ncsu.edu/geospatial/uas-workshop/

[30] P. Thomas S., H. Hartmut H., D. Rider, and M. Rud, "CIRAS, CubeSat Infrared Atmospheric Sounder," California Institute of Technology, Jet Propulsion Laboratory, Mar. 2016, accesed: 2019. [Online]. Available: https://airs.jpl.nasa.gov/system/presentations/files/285_Pagano_CIRAS_Overview_160321.pdf

[31] D. R. Ardila, E. Herman, D. W. Rowen, R. P. Welle, S. J. Wiktorowicz, and B. W. Hattersley, "Two Aerospace Corporation CubeSat Remote Sensing Imagers: CUMULOS and R3," accessed: 2019. [Online]. Available: https://digitalcommons.usu.edu/cgi/viewcontent.cgi?article=3613&context=smallsat

[32] "Infrared cameras and detectors for Aerospace, Defence and Security missions." leonardo company, accessed: 2019. [Online]. Available: https://www.leonardocompany.com/land/optronics/infrared-cameras-and-detectors

[33] S.-E. Quian, *Optical Payloads for Space Missions*, 1st ed. John Wiley & Sons, Ltd, Aug. 2015, iSBN: 9781118945148.

[34] N. Waltham, "CCD and CMOS sensors," in *Observing Photons in Space*, 1st ed., M. C. E. Huber, Ed. New York, NY: Springer New York, 2013, pp. 423–442, iSBN: 978-1-4614-7803-4 978-1-4614-7804-1.

[35] H. Geoffray and F. Guerin, "Measured performance of a low-cost thermal infrared pushbroom camera based on uncooled microbolometer FPA for space applications," Toulouse, France, Dec. 2001, p. 298, doi: 10.1117/12.450672.

[36] T. Greene, "Slitless spectroscopy with the James Webb Space Telescope Near-Infrared Camera (JWST NIRCam)," vol. 9904, 2016, p. pp. 99040E, doi: 10.1117/12.2231347.

[37] "AIM-IR Infrared detectors for industrial, security and space purposes," aIM-IR, accesed: 2019. [Online]. Available: https://www.aim-ir.com/de/home.html

[38] "Infrared Camera Cores | FLIR Camera Cores & Components," accesed: 2019. [Online]. Available: https://www.flir.com/browse/camera-cores--components/thermal-camera-cores/

[39] "Infrared dual band detectors, products and services. QmagiQ," qmagiQ, accessed: 2019. [Online]. Available: http://www.qmagiq.com/eagle256.html

[40] A. Rogalski and K. Chrzanowski, "Infrared devices and techniques," in *Series in Optics and Optoelectronics*. USA, FL: CRC Press, Oct. 2017, pp. 633–686, doi: 10.1201/9781315157009-19.

[41] A. Rogalski, "Infrared detectors: an overview," *Infrared Physics*, 2002, doi: 10.1016/S1350-4495(02)00140-8.

[42] "The Correct Material for Infrared (IR) Applications," edmund opics worldwide, accessed: 2019. [Online]. Available: https://www.edmundoptics.com/resources/application-notes/optics/the-correct-material-for-infrared-applications/

[43] S. Habraken, "Coherent and incoherent optics. Instrumental optics," Lectures from the University of Lige.

[44] A. Rogalski, "History of infrared detectors," *Opto-Electronics Review*, vol. 20, no. 3, Jan. 2012, doi: 10.2478/s11772-012-0037-7.

[45] C. L. Tan and H. Mohseni, "Emerging technologies for high performance infrared detectors," *Nanophotonics*, vol. 7, no. 1, pp. 169–197, Jan. 2018, doi: 10.1515/nanoph-2017-0061.

[46] Z. Jaki, *Micro and Nanophotonics for Semiconductor Infrared Detectors*, 1st ed. Cham: Springer International Publishing, 2014, iSBN: 978-3-319-09673-5 978-3-319-09674-2.

[47] "Quantum efficiency concept for infrared photodetectors." rP Photonics Encyclopedia, accessed: 2019. [Online]. Available: https://www.rp-photonics.com/quantum_efficiency.html

[48] D. T. Nguyen, "Design, modeling, and characterization of innovative terahertz detectors," Ph.D. dissertation, Universit de Grenoble, France, 2012. [Online]. Available: https://tel.archives-ouvertes.fr/tel-00773019

[49] H. Budzier, V. Krause, S. Bhmer, G. Gerlach, and U. Hoffmann, "Fast microbolometer-based infrared camera system," tU Dresden, Institute for Solid State Electronics, accessed: 2019. [Online]. Available: http://www.dias-infrared.de/pdf/p020.pdf

[50] "Cameras and detectors for the infrared," infrared Solutions, Xenics, accessed: 2019. [Online]. Available: https://www.xenics.com/products/

[51] P. Martyniuk and A. Rogalski, "Quantum-dot infrared photodetectors: Status and outlook," *Progress in Quantum Electronics*, vol. 32, no. 3-4, pp. 89–120, Jan. 2008, doi: 10.1016/j.pquantelec.2008.07.001.

[52] A. Rogalski, P. Martyniuk, and M. Kopytko, "InAs/GaSb type-II superlattice infrared detectors: Future prospect," *Applied Physics Reviews*, vol. 4, no. 3, Sep. 2017, doi: 10.1063/1.4999077.

[53] T. L. Haran, J. C. James, and T. E. Cincotta, "Relative performance analysis of IR FPA technologies from the perspective of system level performance," *Infrared Physics & Technology*, vol. 84, pp. 7–20, Aug. 2017, doi: 10.1016/j.infrared.2017.03.007.

[54] "Products and services in infrared detector technology," iRnova, leaders in Type II superlattice detectors, Accesed: 2019. [Online]. Available: https://irnova.se/products/

[55] A. Soibel, J. Nguyen, S. B. Rafol, A. Liao, L. Hoeglund, A. Khoshakhlagh, S. A. Keo, J. M. Mumolo, and J. Liu, "High-performance LWIR superlattice detectors and FPA based on CBIRD design," *Jet Propulsion Laboratory, California Institute of Technology*, no. Proc. SPIE 8268, Quantum Sensing and Nanophotonic Devices IX, p. 7, Jan. 2012, doi: 10.1117/12.909614.

[56] P. Martyniuk, M. Kopytko, and A. Rogalski, "Barrier infrared detectors," *Opto-Electronics Review*, vol. 22, no. 2, Jan. 2014, doi: 10.2478/s11772-014-0187-x.

[57] A. Rogalski, P. Martyniuk, and M. Kopytko, "Challenges of small-pixel infrared detectors: a review," *Reports on Progress in Physics*, vol. 79, no. 4, Apr. 2016, doi: 10.1088/0034-4885/79/4/046501.

[58] A. Jain and A. Biswas, "Parasitic Flux Analysis of Cooled Infrared Detectors for Space Applications," *Defence Science Journal*, vol. 67, no. 2, p. 193, Mar. 2017, doi: 10.14429/dsj.67.11180.

[59] "Dewars and Coolers for infrared detectors." teledyne Judson, accessed: 2019. [Online]. Available: http://www.teledynejudson.com/products/dewars-and-coolers

[60] "Comparison tables of small size cryocooler devices Ricor USA," ricor USA cryogenic and vacuum systems, accessed: 2019. [Online]. Available: http://ricor-usa.com/products/comparison-table/

[61] "Different materials for uncooled detectors of thermal imaging cameras." ,FLIR publications, accessed: 2019. [Online]. Available: http://www.flirmedia.com/MMC/CVS/Appl_Stories/AS_0015_EN.pdf

[62] R. E. Hodges, D. J. Hoppe, M. J. Radway, and N. E. Chahat, "Novel deployable reflectarray antennas for CubeSat communications," in *2015 IEEE MTT-S International Microwave Symposium*. Phoenix, AZ, USA: IEEE, May 2015, pp. 1–4, doi: 10.1109/MWSYM.2015.7167153.

[63] H. Baltes, O. Brand, G. K. Fedder, C. Hierold, J. G. Korvink, and O. Tabata, *CMOS-MEMS: Advanced Micro and Nanosystems*, 1st ed. John Wiley & Sons, Jul. 2008, iSBN: 978-3-527-61693-0.

[64] A. M. Hoang, A. Dehzangi, S. Adhikary, and M. Razeghi, "High performance bias-selectable three-color Short-wave/Mid-wave/Long-wave Infrared Photodetectors based on Type-II InAs/GaSb/AlSb superlattices," *Scientific Reports*, vol. 6, no. 1, Jul. 2016, doi: 10.1038/srep24144.

[65] "Dual-band QWIP MWIR and LWIR infrared detectors." ,QmagiQ, Accessed: 2019. [Online]. Available: http://www.qmagiq.com/products.html

[66] R. L. Johnson, "Bandpass Filters Past and Present," ,Omega Optical Inc., accessed: 2019. [Online]. Available: https://pdfs.semanticscholar.org/30d2/bad9e573f098693877c656886a5cdcafa407.pdf

[67] V. L. Kalyani and V. Sharma, "Different types of Optical Filters and their Realistic Application," *Journal of Management Engineering and Information Technology (JMEIT)*, vol. 3, no. 3, 2016, accessed: 2019. [Online]. Available: https://www.researchgate.net/publication/304696446_Different_types_of_Optical_Filters_and_their_Realistic_Application

[68] M. Malin and B. Cantor, "Mars Micro Orbiter (MMO). Mission objectives and optical payload." accessed: 2019. [Online]. Available: https://www.hou.usra.edu/meetings/smallsat2018/pdf/20_Malin.pdf

[69] R. Ramanath, W. E. Snyder, and H. Qi, "Mosaic multispectral focal plane array cameras," *Infrared Technology and Applications XXX*, vol. 5406, pp. 701–712, Aug. 2004, doi: 10.1117/12.543418.

[70] J. Lu, "High Performance Infrared Narrow Band Pass Filters for Infrared Sensors and Systems," in *IRS 2009 Proceedings*. Hangzhou, China: Multi IR Optoelectronics Co. Ltd., 2009, accessed: 2019. [Online]. Available: https://www.ama-science.org/proceedings/getFile/ZGp3

[71] M. Ebermann, N. Neumann, K. Hiller, M. Seifert, M. Meinig, and S. Kurth, "Tunable MEMS Fabry-Prot filters for infrared microspectrometers: a review," W. Piyawattanametha and Y.-H. Park, Eds., San Francisco, California, United States, Mar. 2016, p. 97600H, doi: 10.1117/12.2209288.

[72] T. D. Rahmlow, Jr., J. E. Lazo-Wasem, S. Wilkinson, and F. Tinker, "Dual band antireflection coatings for the infrared," B. F. Andresen, G. F. Fulop, and P. R. Norton, Eds., Orlando, FL, Apr. 2008, doi: 10.1117/12.780288.

[73] T. D. Rahmlow, Jr., J. E. Lazo-Wasem, J. N. Vizgaitis, and J. Flanagan-Hyde, "Dual-band antireflection coatings on 3rd Gen lenses," B. F. Andresen, G. F. Fulop, and P. R. Norton, Eds., Orlando, Florida, United States, May 2011, doi: 10.1117/12.888100.

[74] M. T. Eismann, *Hyperspectral remote sensing.* Bellingham, Wash: SPIE Press, 2012, iSBN: 978-0-8194-8787-2.

[75] "PRISMA Hyperspectral satellite from the Italian Space Agency (ASI)," eoPortal Directory, ESA, accessed: 2019. [Online]. Available: https://earth.esa.int/web/eoportal/satellite-missions/p/prisma-hyperspectral

[76] "An introduction to CCD operation," mullard space science laboratory, accessed: 2019. [Online]. Available: http://www.mssl.ucl.ac.uk/www_detector/ccdgroup/optheory/ccdoperation.html

[77] "CCD Sensor Architectures," instruments Oxford, accessed: 2019. [Online]. Available: https://andor.oxinst.com/learning/view/article/ccd-sensor-architectures

[78] D. Litwiller, "CCD vs. CMOS: Facts and Fiction," accessed: 2019. [Online]. Available: http://info.teledynedalsa.com/acton/attachment/14932/f-0414/1/-/-/-/-/Photonics_Spectra_CCDvsCMOS_Litwiller.pdf

[79] "Space & Ground-based CMOS Image Sensors," teledyne e2v, accessed: 2019. [Online]. Available: https://www.teledyne-e2v.com/products/imaging/cmos-image-sensors-for-space-and-ground-based-astronomy/

[80] M. Alhussein and S. I. Haider, "Simulation and Analysis of Uncooled Microbolometer for Serial Readout Architecture," *Journal of Sensors*, vol. 2016, pp. 1–13, 2016, doi: 10.1155/2016/9751056.

[81] "Cameras by Teledyne. Infrared imaging devices." accessed: 2019. [Online]. Available: http://www.camerasbyteledyne.com/

[82] "Operations manual for UltraDAS, integration time," ,Isaac Newton Group Of Telescopes, accessed: 2019. [Online]. Available: http://www.ing.iac.es/~docs/ins/das/ins-das-29/integration.html

[83] "What is Exposure Time?" May 2017, stellarNet, Inc.m accessed: 2019. [Online]. Available: https://www.stellarnet.us/what-is-exposure-time/

[84] "Different types of read-out for a detector. ITR vs. IWR." ,FLIR publications, accessed: 2019. [Online]. Available: http://flir.custhelp.com/ci/fattach/get/64611/1535096685/redirect/1/filename/FAQ%20ITR%20vs%20IWR.pdf

[85] "How fast can I image? Frame rate and read-out of detectors," ,HAMAMATSU Photonics, accessed:2019. [Online]. Available: http://camera.hamamatsu.com/jp/en/technical_guides/dissecting_camera/dissecting_camera03/index.html

[86] "Imaging Electronics: Understanding Camera Sensors for Machine Vision Applications," edmund opics worldwide, accessed: 2019. [Online]. Available: https://www.edmundoptics.com/resources/application-notes/imaging/understanding-camera-sensors-for-machine-vision-applications/

[87] "Shot noise and quantum noise," rP Photonics Encyclopedia, accessed: 2019. [Online]. Available: https://www.rp-photonics.com/shot_noise.html

[88] W.-C. Wang, "Optical detectors," Department of Power Mechanical Engineering. National Tsing Hua University., accessed: 2019. [Online]. Available: https://depts.washington.edu/mictech/optics/me557/detector.pdf

[89] R. Hornsey, "Noise in image sensors," accessed: 2019. [Online]. Available: https://ece.uwaterloo.ca/~ece434/Winter2008/Noise.pdf

[90] "Introduction to CMOS Image Sensor Design," National Taiwan University, accessed: 2019. [Online]. Available: http://ccf.ee.ntu.edu.tw/~ypchiou/Intro_EO/CMOS_Image_Sensor.pdf

[91] F. Niklaus, C. Jansson, A. Decharat, J.-E. Kllhammer, H. Pettersson, and G. Stemme, "Uncooled infrared bolometer arrays operating in a low to medium vacuum atmosphere: performance model and tradeoffs," Orlando, Florida, USA, Apr. 2007, p. 65421M, doi: 10.1117/12.719163.

[92] "Characteristics and use of infrared detectors," ,HAMAMATSU, solid state division, accessed: 2019. [Online]. Available: https://www.hamamatsu.com/resources/pdf/ssd/infrared_kird9001e.pdf

[93] D. D. Skatrud and P. W. Kruse, *Uncooled Infrared Imaging Arrays and Systems*, 1st ed., ser. Semiconductors and semimetals. Academic Press, 1997, vol. 47, iSBN: 9780080864440.

[94] V. Mackowiak, J. Peupelmann, Y. Ma, and A. Gorges, "NEP Noise Equivalent Power," ,Thorlabs, Inc., accessed: 2019. [Online]. Available: https://www.thorlabs.com/images/TabImages/Noise_Equivalent_Power_White_Paper.pdf

[95] J. Chouinard, "The Fundamentals of Camera and Image Sensor Technology," accessed: 2019. [Online]. Available: https://www.visiononline.org/userassets/aiauploads/file/cvp_the-fundamentals-of-camera-and-image-sensor-technology_jon-chouinard.pdf

[96] G. Boreman, *Modulation Transfer Function in Optical and Electro-Optical Systems*. Bellingham, WA: SPIE Press, 2001, iSBN: 9780819441430.

[97] "Introduction to Modulation Transfer Function," eo Edmund Optics, accessed: 2019. [Online]. Available: https://www.edmundoptics.com/resources/application-notes/optics/introduction-to-modulation-transfer-function/

[98] P. Coppo, E. Battistelli, M. Barilli, G. Basile, R. Bonsignori, A. Capanni, L. Chiarantini, C. Giunti, S. Pieraccini, A. Romoli, M. Taccola, and U. Del Bello, "Requirements and design of a thermal high-resolution Earth mapper (THEMA) based on uncooled detectors," Crete, Greece, Apr. 2003, doi: 10.1117/12.462609.

[99] "Infrared photodetectors and thermal detectors for ground and space applications," ,SOFRADIR, France. [Online]. Available: https://www.lynred.com/

[100] C. Underwood, "Low-Cost Satellite Infrared Imager Study," 2004, accessed: 2019. [Online]. Available: https://www.researchgate.net/publication/235013266_Low-Cost_Satellite_Infrared_Imager_Study

[101] A. Redjimi, D. Kneevi, K. Savi, N. Jovanovi, M. Simovi, and D. Vasiljevi, "Noise Equivalent Temperature Difference Model for Thermal Imagers, Calculation and Analysis," 2014, accessed: 2019. [Online]. Available: http://www.vti.mod.gov.rs/ntp/rad2014/2-2014/6/6.pdf

[102] A. Duenas Herrero, "Study of a CubeSat dual-band infrared imager for hydric stress observation from space." 2019, university of Lige.

[103] T. S. Pagano, D. Rider, and M. Rud, "Measurement approach and design of the CubeSat Infrared Atmospheric Sounder (CIRAS)," San Diego, California, United States, Sep. 2016, p. 997806, doi: 10.1117/12.2235986.

[104] D. Mamula, T. Pagano, J. Ostroy, and J. Inskeep, "NOAA EON-IR CubeSat Study for Operational Infrared Soundings," accessed: 2019. [Online]. Available: http://mstl.atl.calpoly.edu/~bklofas/Presentations/SummerWorkshop2017/Mamula.pdf

[105] "HyperScout hyperspectral imager." , Cosine technologies, accessed: 2019. [Online]. Available: https://www.cosine.nl/portfolio/hyperscout/

[106] M. Almasri, Bai Xu, and J. Castracane, "Amorphous silicon two-color microbolometer for uncooled IR detection," *IEEE Sensors Journal*, vol. 6, no. 2, pp. 293–300, Apr. 2006, doi: 10.1109/JSEN.2006.870139.